Photophysical Processes and Metal Ion Complexation of Fluorogenic Ligands with Single Molecule Sensitivity

By

ARJUN SHARMA

CHEM01201504017

Bhabha Atomic Research Centre, Mumbai

A thesis submitted to the

Board of Studies in Chemical Sciences

In partial fulfillment of requirements

for the Degree of

DOCTOR OF PHILOSOPHY

of

HOMI BHABHA NATIONAL INSTITUTE

May, 2019

Homi Bhabha National Institute

Recommendations of the Viva Voce Committee

As members of the Viva Voce Committee, we certify that we have read the dissertation prepared by "**Arjun Sharma**" entitled "**Photophysical Processes and Metal Ion Complexation of Fluorogenic Ligands with Single Molecule Sensitivity**" and recommend that it may be accepted as fulfilling the thesis requirement for the award of Degree of Doctor of Philosophy.

Chairman – Prof. S. Adhikari		**Date:** 07/08/2019
Guide – Prof. M. Kumbhakar	Manoj Kumbhakar	**Date:** 07/08/2019
Examiner – Prof. A. Datta	Datta	**Date:** 07/08/2019
Member 1- Prof. V. Sudarshan	Sudarshan. V	**Date:** 07/08/2019
Member 2- Prof. T. Jayasekharan	T. Jayasekharan	**Date:** 07/08/2019
Member 3- Prof. S. Maiti		**Date:** 7/8/19

Final approval and acceptance of this thesis is contingent upon the candidate's submission of the final copies of the thesis to HBNI.

I hereby certify that I have read this thesis prepared under my direction and recommend that it may be accepted as fulfilling the thesis requirement.

Date: 07/08/2019

Place: BARC

Manoj Kumbhakar

Prof. Manoj Kumbhakar

(Guide)

STATEMENT BY AUTHOR

This dissertation has been submitted in partial fulfillment of requirements for an advanced degree at Homi Bhabha National Institute (HBNI) and is deposited in the Library to be made available to borrowers under rules of the HBNI.

Brief quotations from this dissertation are allowable without special permission, provided that accurate acknowledgement of source is made. Requests for permission for extended quotation from or reproduction of this manuscript in whole or in part may be granted by the Competent Authority of HBNI when in his or her judgment the proposed use of the material is in the interests of scholarship. In all other instances, however, permission must be obtained from the author.

Arjun Sharma

DECLARATION

I, hereby declare that the investigation presented in the thesis has been carried out by me. The work is original and has not been submitted earlier as a whole or in part for a degree / diploma at this or any other Institution / University.

Arjun Sharma

List of Publications arising from the thesis

Journal

1. "Photon Antibunching in Complex Intermolecular Fluorescence Quenching Kinetics", **Arjun Sharma**, Jörg Enderlein and Manoj Kumbhakar, *Journal of Physical Chemistry Letters*, **2016**, *7*, 3137-3141.

2. "Origin of Excitation Dependent Fluorescence in Carbon Nanodots", **Arjun Sharma**, Trilochan Gadaly, Alka Gupta, Anand Ballal, Sunil Kumar Ghosh and Manoj Kumbhakar, *Journal of Physical Chemistry Letters*, **2016**, *7*, 3695-3702.

3. "Molecular Origin and Self-Assembly of Fluorescent Carbon Nanodots in Polar Solvents", **Arjun Sharma**, Trilochan Gadaly, Suman Neogy, Sunil Kumar Ghosh and Manoj Kumbhakar, *Journal of Physical Chemistry Letters*, **2017**, *8*, 1044-1052.

4. "Photon Antibunching Reveals Static and Dynamic Quenching Interaction of Tryptophan with Atto655", **Arjun Sharma**, Jörg Enderlein and Manoj Kumbhakar, *Journal of Physical Chemistry Letters*, **2017**, *8*, 5821-5826.

5. "Addition to "Molecular Origin and Self-Assembly of Fluorescent Carbon Nanodots in Polar Solvents"", **Arjun Sharma**, Trilochan Gadaly, Suman Neogy, Sunil Kumar Ghosh and Manoj Kumbhakar, *Journal of Physical Chemistry Letters*, **2017**, *8*, 5861-5864.

6. "Determining Metal Ion Complexation Kinetics with Fluorescent Ligand by Using Fluorescence Correlation Spectroscopy", **Arjun Sharma**, Aranyak Sarkar, Dibakar Goswami, Arunasis Bhattacharyya, Jörg Enderlein and Manoj Kumbhakar, *ChemPhysChem*, **2019**, DOI: 10.1002/cphc.201900517.

Conferences

1. "Origin of Excitation Dependent Fluorescence in Carbon Nanodots", **Arjun Sharma**, Trilochan Gadaly, Alka Gupta, Anand Ballal, Sunil Kumar Ghosh and Manoj Kumbhakar, **12th National Symposium on Radiation and Photochemistry** (**NSRP-2017**); March 2-4, 2017; Manipal University, Karnataka.

2. "Photon Antibunching in Complex Intermolecular Fluorescence Quenching Kinetics", **Arjun Sharma**, Jörg Enderlein and Manoj Kumbhakar, **14th**

DAE-BRNS Biennial Trombay Symposium on Radiation and Photochemistry (**TSRP-2018**); January 3-7, 2018, BARC, Mumbai.

3. "Fluorescence Correlation Spectroscopy in Exploring Metal Ion Complexation", **Arjun Sharma** and Manoj Kumbhakar, **13th National Symposium on Radiation and Photochemistry** (**NSRP-2019**); February 7-9, 2019; Visva-Bharati Santiniketan, West Bengal.

4. "Single Molecule Spectroscopic Investigation of Photophysical Processes"; Oral presentation by **Arjun Sharma**, **13th National Symposium on Radiation and Photochemistry (NSRP-2019)**; February 7-9, 2019; Visva-Bharati Santiniketan, West Bengal.

Arjun Sharma

Dedicated

to

My beloved Parents

ACKNOWLEDGEMENTS

First and foremost, I wish to record my deepest sense of gratitude and sincere thanks to my Ph.D. supervisor Prof. Manoj Kumbhakar for his invaluable guidance, unstinted inspiration, keen interest, continuous encouragement, good wishes, valuable suggestions and support throughout my entire research tenure. I would also like to record my sincere thanks to his wife Dr. (Mrs) Doyel Kumbhakar for her very strong moral support, advices and constant motivation which helped me a lot to finish my work on time.

I am deeply indebted to Prof. Jörg Enderlein (Gottingen, Germany) for his invaluable guidance, research support, critical comments, good wishes and valuable suggestions during the entire course of my Ph.D.

It gives me immense pleasure to thank all the members of the doctoral committee Prof. S. Adhikari, BARC (Chairman), Prof. V. Sudarsan, BARC (Member), Prof. T. Jayasekharan, BARC (Member) and Prof. S. Maiti, TIFR (Member) for critically evaluating my research activities time to time and providing valuable suggestions during the progress review and pre-synopsis seminar for completion of this work.

It is my great privilege to acknowledge Prof. P. D. Naik (Former Associate Director, Chemistry Group & Dean, HBNI), Prof. D. K. Palit (Former Head, RPCD), Prof. H. Pal (Associate Director, Chemistry Group A), Prof. S. Kapoor (Associate Director, Chemistry Group D & Head, RPCD) and Prof. A. C. Bhasikuttan (Head, MPS, RPCD) for their encouragement and support in carrying out the research work.

I express my sincere thanks to Prof. S. K. Ghosh (Head, FTD), Dr. Trilochan Gadaly (BOD), Dr. Dibakar Goswami (BOD), Dr. Arunasis Bhattacharyya (RCD), Dr. S. Neogy (MMD), Dr. Alka Gupta (MBD), Dr. A. D. Ballal (MBD) and Dr. Goutam Chakraborty (L&PTD) for providing their priceless contribution and support in the present work.

I am very much grateful to Dr. Prabhat Singh, Dr. Aruna Kumar, Dr. Rajib Ghosh, Mr. Aranyak Sarkar, Mr. Veeresh Nayak and Dr. Apurav Guleria for giving unconditional support and scientific advice during the entire course of my Ph.D. I also wish to express my sincere thanks to all other RPCD members for their support at different times.

I wish to express my sincere gratitude and indebtedness to my parents and other family members for their love and support to me.

I also wish to thank my friends especially Ms. Meenakshi Joshi, Mr. Raman Khurana, Mr. Gawali Santosh, Mr. Vikas Dhiman, Mr. Ajay Kumar, Mr. Sarjan Singh, Mr. Manjeet Singh and Mr. Ram Tripathi for their constant unconditional support.

Finally, I would like to thank God for giving me such a beautiful life and colleagues who filled my life with success and extreme happiness.

CONTENTS

Summary

Over the past few decades fluorescence-based spectroscopic techniques have evolved to cater to the needs of various biological and analytical investigations, often with quantitative information. The core aspect here is to explore and understand molecular interactions, the citadel to predict its structure and function of any chemical or biological system. Conventional fluorescence based methods provide insights of molecular interactions, i.e. stoichiometry, kinetics & thermodynamics. These findings have direct applications in bio-speciation and bio-sequestration research of various metal ions. However, use of conventional fluorescence methods is limited with actinides (and in general with any radioactive element) due to restrictions of high activity handling. In this regard, present thesis is aimed at easing of this activity handling constrain by developing single molecule sensitive methods of studying molecular interactions with unprecedented reduction of activity handling (< 1 Bq). Our endeavor is to design and develop single molecule sensitive methods to study the interaction kinetics with special emphasis to complex formation and also suitable single molecule probes for studying heavy metal ion interaction through binding kinetics.

In this regard, we first demonstrated the possibility of studying kinetics of intermolecular interactions between standard PET pairs; using single molecule sensitive photon antibunching (or ns fluorescence correlation spectroscopy). We observed that, unlike any other method, the single molecule sensitive photon antibunching experiments can provide complete information regarding the mechanism and kinetics of molecular interactions occurring in both excited and ground state of the fluorophore. We exemplified these observations by first studying the interactions between Rhodamine110 and aniline (Chapter 3) where predominant interactions are observed in the excited state of the fluorophore (Rh110) and then by studying the interactions

between Atto655 and Tryptophan (Chapter 4) where the predominant interactions occur in the ground state of the fluorophore (Atto655).

On the basis of positive results obtained from the above mentioned experiments, we further explored the potential of single molecule sensitive FCS in studying the interactions/complexation of metal ion with chelating fluorophores which is expected to be a pure ground state phenomenon. We studied the mechanism and kinetics of complexation between Calcein (well-known fluorescent chelator) and various metal ions (iron, uranium, europium and americium) using very low sample amounts. With these experiments, we have demonstrated that the single molecule sensitive FCS experiments can be employed over studying the kinetics of ground state interactions, especially of actinides using minute sample amount (~fM of actinides), which is close to their disposable limit. These results promote the hassle free work with poisonous or radioactive metals and complete the main objective of thesis.

However, development of suitable fluorescent probe is very important for the better utilization of single molecule sensitive techniques. Thus, in the present thesis, we have also worked over the development and photophysical characterization of fluorescent carbon nanodots with the aim to use it as a fluorescent marker as well as ligand for metal ion complexation. We explored the origin of their excitation dependent fluorescent behaviours as due to multiple electronic states originating from molecules, aggregates and weekly fluorescent CNDs in the system. Next, we tried to study the interaction of CNDs with Uranyl ions for binding assay in ensemble spectroscopy in which we observed very low value of binding constant (K), implicating the need for very high metal ion concentration for any significant interaction. However, FCS measurements for the same system were found unsatisfactory due to very low quantum yield of the CNDs in presence of metal ions. Hence, we opted for other bright ligands, like calcein for metal ions binding assay with single molecule sensitivity.

LIST OF ABBREVIATIONS

ADC	Analog to Digital Converter
APD	Avalanche Photodiode
AFM	Atomic Force Microscopy
A655	Atto655 dye
CzA	Citrazinic Acid
CD-f	Fractions of Carbon Nanodots
CND	Carbon Nanodot
CFD	Constant Fraction Discriminator
CW	Continues Wave
FCS	Fluorescence Correlation Spectroscopy
FT-IR	Fourier Transform Infra-Red
FIFO	First in First Out
FRET	Förster Resonance Energy Transfer
GRS	Gamma Ray Spectroscopy
HP-PMTs	High Performance Photomultiplier Tubes
IC	Internal Conversion
ISC	Inter System Crossing
IRF	Instrument Response Function
LIF	Laser Induced Fluorescence
MCP-PMT	Micro Channel Plate Photomultiplier Tubes
MCA	Multichannel Analyser

NMR	Nuclear Magnetic Resonance
NA	Numerical Aperture
PET	Photoinduced Electron Transfer
PMT	Photomultiplier Tubes
PL	Photoluminescence
Rh110	Rhodamine 110 Dye
SS	Steady State
SV	Stern Volmer
TR	Time Resolve
TCSPC	Time Correlated Single Photon Counting
TEM	Transmission Electron Microscopy
TRLIF	Time Resolved Laser Induced Fluorescence Spectroscopy
TAC	Time To Amplitude Convertor
TTS	Transit Time Spread
Trp	Tryptophan

LIST OF FIGURES

LIST OF TABLES

CHAPTER 1

Introduction

The ever increasing demand in nuclear power, space exploration, nuclear arsenal and accident escalates risk of human encounter with toxic metal ions, which underlines the need for renewed interest in exploring biochemical uptake, transport and storage of these toxic metal ions, along with development of suitable chelators to remove these radioactive metals from the body.[1-5] However major constrain in bio-speciation and bio-sequestration research with actinides (and in general with any radioactive element) is the elaborate handling of radioactive samples to minimize radiation exposure to experimenters, and thus severely limiting number of experiments performed with active metal ions,[2,3] and quite often researchers resort to investigating inactive metal ions showing similar physico-chemical behavior.

Generally, conventional ensemble spectroscopy for bio-speciation and bio-sequestration research employs metal ion complexation and or dissociation kinetics following changes in absorption or fluorescence signal of either metal (e.g. actinides & lanthanides) or (bio-) ligands. But the major constrain in conventional methods is their limited applicability over essential, toxic or radioactive materials due to the required sample size. Typical experiments with radioactive metal ions involve around 1 ml sample solution of concentrations

in the range of 10^{-6} M or more.[2,3,6-10] Such a sample, for example of ^{241}Am, will have activity of ~31 kBq (considering specific activity as 3.43 Ci/g).[8,9] Hence, extreme precaution towards safe handling of such sample and hazard minimization is synonymous to chemistry of radioactive elements.

Therefore, demonstration of a simple but robust spectroscopy method capable of investigating complexation or dissociation phenomena quantitatively with a significantly reduced amount of radioactive material is needed to not only benefit the bio-speciation and bio-sequestration research but also to the chemistry of radio-active metals in general. In this regard, use of single molecule sensitive techniques for studying the actinides can provide million times reduction in the overall activity handling as compared to the conventional experiments. And the activity of most important actinides like ^{241}Am, ^{239}Pu, etc. at femtomoles comes close to their acceptable disposable limit (< 1 Bq/mL for α-activity) (see Table 1.1).

Hence, single molecule sensitive fluorescence methods possess an edge over conventional methods in terms of safely handling of actinide samples for their interaction kinetics. But, these techniques have not been explored much in studying the molecular interactions therefore development of suitable methodology for such study of metal ions interaction especially complexation reaction with molecules/ligands is very essential. Thus, the present thesis will explore the applicability of single molecule sensitive technique over studying the complex molecular interactions and metal ion complexation of fluorogenic ligands in both of its excited and ground state. Further, efforts will also be made over designing suitable fluorescence probes for better utilization of single molecule spectroscopy in the field of actinide bio-speciation and sequestration research.

Actinides	Half life	Specific activity (dps/g)	Activity (dps)	
			Conventional flu. Spct.; 1 ml, 1 μM	Single molecule flu. Spct.; 1 μl, 1 nM
U-235	7.04×10^{8} y	8000	1.88×10^{-2}	1.88×10^{-8}
U-232	68.9 y	8.28×10^{11}	$1.92x\ 10^{5}$	0.192
U-233	159200 y	3.56×10^{8}	82.9	8.29×10^{-5}
Pu-239	24100 y	2.3×10^{9}	5.49×10^{2}	**5.49×10^{-4}**
Pu-241	14 y	3.9227×10^{12}	9.4472×10^{5}	**0.945**
Am 241	432.2 y	1.26×10^{11}	3.03×10^{4}	**0.0303**
Am 242	141 y	9.33×10^{13}	2.25×10^{7}	22.5
Am 243	7370 y	7.39×10^{9}	1.79×10^{3}	0.0017
Cm-241	32.8 d	6.108×10^{14}	1.47×10^{8}	1.47×10^{2}
Cm-242	160 d	1.25×10^{14}	3.02×10^{7}	30.2
Cm-243	29.1 y	1.87×10^{12}	$4.54x\ 10^{5}$	**0.454**
Cm-244	18.1 y	2.98×10^{12}	7.27×10^{5}	0.727
Cm-245	8500 y	6.34×10^{9}	1.55×10^{3}	0.00155

Table 1.1: Radioactivity of various important actinides observed in conventional and single molecule fluorescence spectroscopy.

A brief discussion about various aspects of the thesis is summarized here. First begin with description of fluorescence & photophysics, the elegant property of an analyte, used extensively in the present scientific endeavor.

1.1 Introduction to the fluorescence and Jablonski diagram

Over last three decades, analytical methods have recorded a remarkable growth due to inventions and advancements in various spectroscopy techniques. Among these, fluorescence spectroscopy has attracted immense attention of broad scientific community because of its high sensitivity, selectivity, easier handling and capabilities for both in vivo and in vitro experiments.

For qualitative and/or quantitative measurements of non-fluorescent analytes, where direct observations is not possible, indirect methods like fluorescence enhancement or quenching in presence of other reactant is preferred.

Fluorescence is an intrinsic property of the molecule or ion called as 'fluorophore' by virtue of which an excited fluorophore relaxes back to its ground state via radiative emission. It was first discovered by Sir John Frederick in 1845 while analyzing quinine solution[11] and later on illustrated by Prof. A. Jablonski using famous Jablonski diagram (Figure 1.1). Besides molecules or clusters, the fluorescence can also be observed from individual atoms like actinides as discussed ahead.

Fluorescence in Actinides: Most of the actinides like U(VI), Am(III), Cm(III), etc. shows weak but discrete fluorescence spectra.[12-14] This can be used in conventional spectroscopy methods to determine their various important parameters such as oxidation state, coordination number and concentrations, etc. However, due to the forbidden nature of underlying f-f transitions, their molar extinction coefficients and fluorescence quantum yield is generally observed to be very low. Therefore, the conventional fluorescence methods face huge difficulties over the sensitive or trace level determinations of these materials. Thus, more powerful and sensitive methods like laser induced fluorescence or gamma ray spectroscopy are generally employed over the trace level detection/studies of actinides.[2,10,15] But, despite of being highly suitable for both qualitative and quantitative estimation of actinide, these methods possess certain serious limitations in studying the complexation chemistry of metal ions with organic or bio-relevant chelating ligands (discussed later). Therefore, sensing of fluorogenic ligand is generally preferred over active metal ions in order to study their complexation behaviour. But,

prior knowledge of such ligand's photophysics and other fluorescence properties are prerequisite and thus discussed ahead.

Molecular Fluorescence: Jablonski diagram illustrates how photo or thermally induced excitations of molecule can results into various physical transitions in its excited state.[11,16] The diagram is given in Figure 1.1.

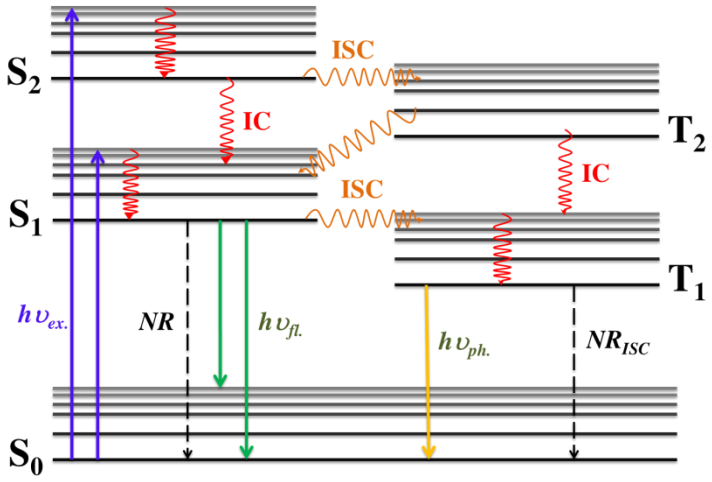

Figure 1.1: Jablonski diagram for the illustration of electronic transitions in the molecule. T_1 and T_2 represent triplet states of the fluorophore.

The absorption of a sufficiently energetic photon ($h\upsilon_{ex}$) results in the electronic excitation of molecule from its ground singlet state (S_0) to the excited singlet states (S_1, S_2, etc.). Molecules are unstable in their excited states thus perform various transitions among energy levels to obtain stability. These transitions could be either radiative or non-radiative, depending upon the separation of the energy level. Transitions between closely spaced energy level like S_1, S_2 and T_1 (triplet state of fluorophore) takes place via non-radiative pathways known as internal conversion (IC) and inter system crossing (ISC). IC occurs between the energy levels of similar multiplicity like S_1 and S_2, whereas the ISC occurs between energy levels of different multiplicity (S_1 and T_1).

In case of well separated energy levels like S_0 and S_1 the probability of radiative transition is more and therefore we observe two types of radiative emissions named as fluorescence or phosphorescence. Fluorescence is the spin allowed radiative transition of the fluorophore from its first excited singlet state to the ground singlet state. On the other hand, the phosphorescence is spin forbidden radiative transition of fluorophore from its high energy first triplet state (T_1) to the ground singlet state. Therefore, the yield and decay rate of fluorophore via phosphorescence is observed to be approximately thousand times smaller ($k_{ph} = 10^4$-10^8) than that of via fluorescence ($k_f = 10^8$-10^{10}).

Further, fluorescence is very sensitive property of the fluorophore. Therefore, the spectral shape, lifetime and intensity of fluorescence hugely depend on its surrounding physical and chemical environment.[11,16] As excitation of fluorophore results in the polarization of its electronic cloud therefore, molecules are generally more reactive in their excited state thus prone to various physical transitions or chemical reactions. The physical transitions like IC, ISC and collisional quenching come in the category of photophysics whereas the chemical reactions, dimerization, isomerization or permanent degradation of fluorophore comes under the photochemistry of molecule.

The fluorescence quenching is one of the photophysical process governed by an excited fluorophore by which its excess energy gets transferred to other molecule known as quencher by means of electron, proton, or energy transfer.[11,16] This excited quencher molecule may perform some chemical transformations (photosensitization) or de-excite via radiative (generally observed in FRET) or non-radiative emission of energy. In the former case, the fluorescence quenching is termed as sensitization which has been found very crucial in various biological processes such as photosynthesis. Thus, studies over the kinetics and mechanism of such

photoinduced processes are highly important to uncover various important biological and non-biological processes.

Besides, being a quantitative phenomenon, the fluorescence quenching is also used for determining the kinetics of various bimolecular interactions.[17-22] However, some interactions may also result in the enhancements of fluorescence instead of quenching. But in both of these cases, the change in fluorescence intensity can be used for determining the thermodynamics and kinetics of bimolecular reactions.[16,23] Fluorescence enhancements are mainly governed by either increasing in the extinction coefficient or increase in the fluorescence quantum yield of the fluorophore when it binds to the other molecule or ion. It is mostly encountered in case of ground state complexation of fluorogenic ligands with metal ions thus used for major applications in sensing various important metal ions in solution.[24]

As detection of fluorescence against dark background is relatively easier and more sensitive therefore, enhancement methods are practically more useful than quenching in studying the thermodynamics of molecular interactions. However, designing of suitable fluorescence probes for fluorescence enhancement based experiments is the biggest hurdle as compare to relatively simple fluorescence quenching experiments. Thus, fluorescence quenching methods are generally and most widely employed (though selectivity still remains the tricky issue) for analyzing the molecular interactions occurring in both excited and ground state of the fluorophore. In the present thesis, we have also used fluorescence quenching as an elegant method of studying mechanism, kinetics and thermodynamics of bimolecular interactions in solution. Therefore we will further extend our discussion over fluorescence quenching to comprehend the molecular interactions and their kinetics.

1.2 Kinetics of bimolecular interactions with fluorescence quenching

Stern Volmer (SV) plots are generally used in fluorescence spectroscopy[11,16] to study the kinetics of bimolecular interactions resulting in the quenching of fluorescence. It is a plot between the ratio of fluorescence intensity or fluorescence lifetime of fluorophore (F) in the absence (I_0, τ_0) and presence (I, τ) of quencher (Q) verses quencher concentration [Q], in the solution. Depending upon the type of interactions occurring in the solution, the SV plot can be obtained in four different ways, as shown in Figure 1.2. Let us first discuss the case when the fast dynamic interactions occur only in the excited state of the fluorophore

Case 1: Dynamic interactions occurring only in the excited state of the fluorophore

These types of interactions are mostly governed by electron or energy transfer mechanisms which are very fast as compared to the decay rate of the fluorophore.[11,16] Quencher molecule diffuses through solution and collides with an excited fluorophore (F*) to quench its fluorescence by either PET (photoinduced electron transfer) ($F^* + Q \rightarrow F^+..Q^-$) or FRET (Förster resonance energy transfer) mechanism ($F^* + Q \rightarrow F..Q^*$). This quenched fluorophore then gets solvated and relaxes back to its ground state (F). As these interactions are governed by the collisional interactions of fluorophore and quencher molecule, thus also called as dynamic interactions or quenching. In such type of interactions, the SV equation is given by[11,16]

$$\frac{I_0}{I} = \frac{\tau_0}{\tau} = 1 + K_{SV}[Q] \tag{1.1}$$

Thus, here the SV plot shows linear variation with quencher concentration [Q] as shown in Figure 1.2 (a). The SV eq. (1.1) is derived for a bimolecular pseudo first order reactions where [F]<<[Q].[16] It also assumes the complete quenching of fluorophore after successful interactions (and no exciplex formation). Eq. (1.1) is used to fit the recorded SV plot

and we get SV constant (K_{SV}). It is the product of dynamic quenching rate constant (k_{d+}) and the fluorescence lifetime (τ_f or τ_0) of the fluorophore in absence of quencher.

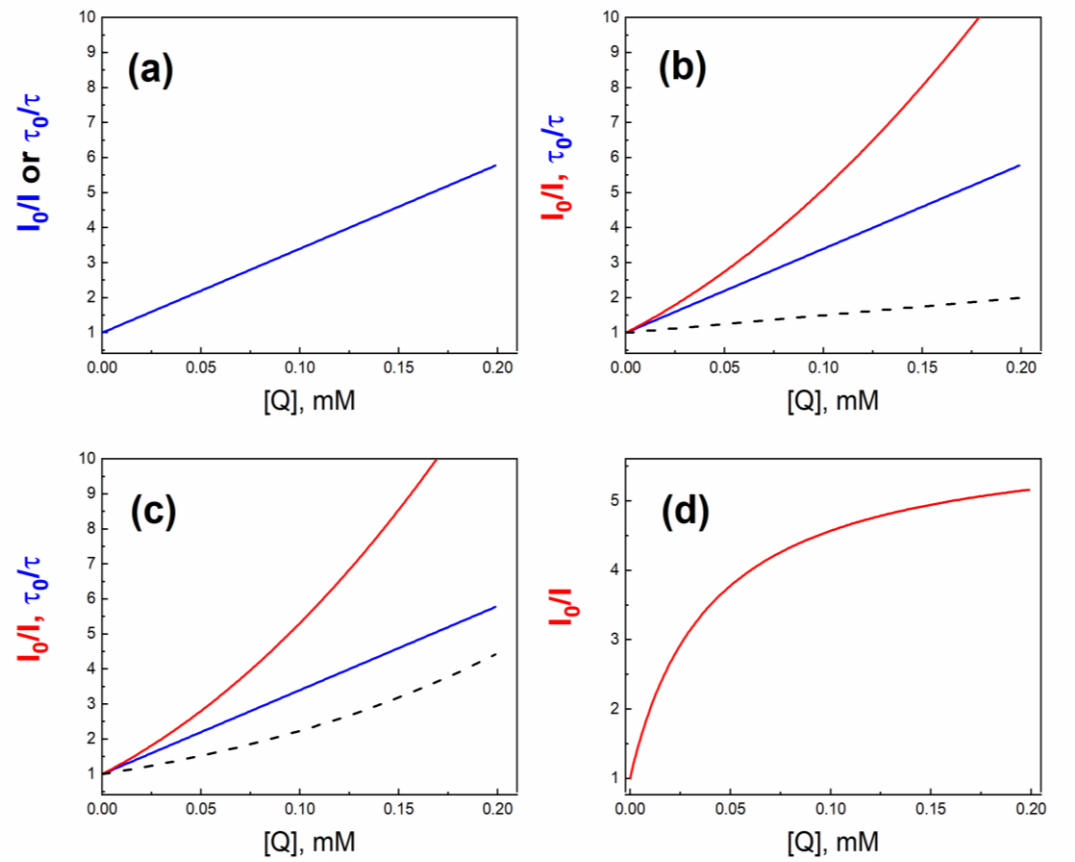

Figure 1.2: Schematic of SV plots for different types of fluorescence quenching. Figure (a) represents SV plot for only dynamic interactions (k_{d+} = 6 x 10^9 M^{-1} s^{-1}); (b) represents dynamic and static interactions (K = 5.0 M^{-1}); (c) represents combined dynamic, static and sphere of action interactions ($V.N_a$= 0.4M^{-1}) and (d) represents SV plot for multi-fluorophoric system either due to the presence of multiple fluorophore or formation of weakly fluorescent complex (K = 25.0 M^{-1}). The black colored dotted curves in (b) and (c) represent ratio of the steady state data and time resolve SV data which helps in defining the type of interactions in the system.

Case 2: Combined dynamic and static quenching

In addition to the excited state, the interactions or complexation of fluorophore with quencher molecule or ion in its ground state (F + Q ⇌ FQ) leads to additional variation in the SS SV plot (Figure 1.2b). This additional quenching due to ground state interaction is called as static

quenching as it is not diffusion controlled and occur at very fast rate (> 10^{11} s^{-1}). But, due to lower time resolution (~ 100ps) of conventional time resolved TCSPC setups, these interactions are not observed in the TCSPC data and we only see the dynamic interaction part in TR SV plot i.e. only linear variations.

However, experiments with ultrafast time resolve techniques like fluorescence up-conversion, one can follow these fast electron transfer reactions.[25] But due to very low S/N ratios, these measurements require very high concentration of dyes which is again non preferable due to complex chemistry of dyes (due to aggregation) at high concentrations.[26]

In such cases, modified SV equation[11,16] (eq. (1.2))is used to analyze SS SV data, where the TR SV data is used to determine Stern Volmer constant (K_{sv}) using eq. 1.1 and then SS SV data is fitted with eq. (1.2) to obtain the ground state complexation equilibrium constant (***K***).

$$\frac{I_0}{I} = \left(1 + K_{SV}\left[Q\right]\right)\left(1 + K\left[Q\right]^n\right) \tag{1.2}$$

here ***n*** represents stoichiometry of the ground state complexation. It is evident from eq. (1.1) and eq. (1.2) that in case of 1:1 ground state interactions, the ratio of SS and TR SV data must result in the linear curvature as shown in dotted black lines in Figure 1.2b. Thus identifying 1:1 ground state complexation is easier by carefully analyzing the SS and TR SV data. However, for higher order complexation, the ratio will still result in positively deviated curve thus require prior understanding of reaction mechanism to correctly analyze SS SV plots.

Case 3: Combined dynamic, static and sphere of action quenching

Besides dynamic and static quenching, one more form of quenching is observed specifically at very high concentrations of the quencher (> 50mM) known as quenching due to the sphere of action.[11,16] In this case, the quencher molecule located in very close vicinity of

fluorophore called as active sphere, immediately quenches the fluorescence as soon as the fluorophore gets excited. Just like static quenching, these types of interactions are also not diffusion controlled and occur at very fast rate to not observe in conventional TR setups. As these interactions are related to the spatial distribution of quencher molecules, thus the probability to encounter this type of fluorescence quenching decreases exponentially with lowering the quencher concentrations and vice versa.[16] Hence in this case, the ratio of steady state and time resolve SV plot further produces positively deviated curve in SV plot shown as black dotted curve in Figure (1.2(c)). Therefore, in order to determine the kinetics of bimolecular reaction in such type of complex system, the further modified SV equation[11,16] is used which includes all types of interaction like dynamic, static and sphere of action quenching and given by

$$\frac{I_0}{I} = \left(1 + K_{SV}[Q]\right)\left(1 + K[Q]^n\right)e^{VN_a[Q]} \tag{1.3}$$

here $\boldsymbol{V}$ represents the volume of active sphere of quenching and $\boldsymbol{N_a}$ is Avogadro constant. Inside this active volume, the probability of quenching is 1.[16] Thus, knowing the volume $\boldsymbol{V}$**,** one can calculate the radius of active sphere which can be very useful in analyzing various biological processes like protein folding or conformational dynamics, etc.[11]

Case 4: Negative deviation in SV plot

The above mentioned SV equations are derived only for those systems where a single fluorogenic analyte is present for analysis and it also assumes complete quenching of the fluorophore once it gets interacted or complexed with the quencher molecule. However, in some cases only certain fraction of analyte gets quenched (certain isomers) and in other the formed complex may also shows some fluorescence which also results in shifting the emission spectra. In all these type of cases the quenching experiments shows negative deviations in the SV plot

and cannot be analyzed with simple SV equations. Therefore in such cases other simplified pseudo first order equation[16,23] is used for the analyses given by

$$\frac{I_0 - I}{I_0 - I_f} = \frac{K[Q]^n}{1 + K[Q]^n} \tag{1.4}$$

here *n* and *K* stands for the stoichiometry and overall equilibrium constant for bimolecular ground state interactions between F and Q respectively. Here fluorescence intensity is used as a relative quantitative parameter thus eq. (1.4) can also be used by any other quantitative spectroscopy methods such as absorption spectroscopy, for determining the equilibrium constant of various weakly or non-fluorescent ligands with their respective ions/molecules.[23]

The thermodynamics of the actinide complexation with their newly developed ligands can also be studied with similar method. But most of the synthesized ligands usually exhibit very weak extinction coefficient and fluorescence quantum yield, pressing for the use of high ligand concentrations in the mM range. Thus, to observe a sufficient variation in the absorption spectra of these ligands the corresponding metal ion need to be added at comparable amount resulting in several orders of radioactivity above the safe acceptable limit. Due to the safety hazards involved in handling high radioactivity samples using conventional analytical methods only limited experiments are performed with limited knowledge about their chemical behaviors. Therefore, more sensitive quantitative methods have been designed in recent decades[2,10] for trace level measurements with these materials. However, even these methods limit the user in studying complexation of actinides with bio-relevant ligands and ligands in general, as discussed below.

1.3 Other spectroscopy methods used to study actinides

Among various techniques, the time resolved laser induced fluorescence spectroscopy[2,10] (TRLIF) and gamma ray spectroscopy[15] (GRS) are considered the most suitable

method for direct detection of trace metal ions and their speciation. However, both of these methods fall short in studying the kinetics of metal ion interactions with biologically relevant ligands as explained below.

1.3.1 Laser induced fluorescence (LIF) spectroscopy

LIF spectroscopy is one of the popular and very sensitive technique to study the actinides. Here, laser induced fluorescence means the fluorescence obtained after exciting the fluorophore with lasers. The obtained fluorescence signal can be divided into two categories called steady state and time resolved laser induced fluorescence (TRLIF). Steady-state techniques measure the overall intensity, peak wavelength, and spectral shape of the fluorophore. This helps in determining the strength, oxidation state and chemical environment around the fluorophore. On the other hand, time resolved measurements determine the average length of time for which a given fluorophore emits light. This time is termed as fluorescence lifetime of the fluorophore. Fluorescence lifetime is sensitive to various variables associated with biological microenvironment such as ion concentration, pH, enzymatic activity, molecular binding and temperature therefore, allowing these biological factors to be analyzed.

In case of heavy metals, the TRLIF techniques have been used to measure the strength, composition, and symmetry of the first coordination shell of multiple actinides and lanthanides with sensitivity up to the trace levels. These experiments can be performed at very low concentrations of metal ions (nM – pM), over a wide temperature range of 10 – 363 K with time-resolution from ~100 fs to few ms. Therefore, these techniques can be used for speciation of various fluorescent metal ions at environmentally relevant conditions. However, as different metal ions possess different excitation spectra and fluorescence lifetime therefore; specific lasers are used for specific analytes. TRLIF measurements are mostly made over few actinides like

Am(III), Cm(III), U(IV) and U(VI), as well as Eu(III), and to a lesser extent for other lanthanides. The observed fluorescence lifetime can provide information regarding the number and proximity of quenchers in the coordination sphere of the luminescent probe. This makes TRLIF as an elegant method to understand the chemistry of the actinides or any fluorescent metal ion in solid or in solution phase.

However, detection of actinides becomes very difficult in the presence of organic impurities or ligands due to the screening by organic moieties because of very low extinction coefficient of actinides (< 100 mol^{-1} cm^{-1}) as compared to organic materials. Thus high power lasers are generally used to sense metal ion in such cases, which certainly may results in degrading the organic or bio-relevant ligands. Thus molecular interactions are very difficult to study by LIF or TRLIF spectroscopy of actinides.

In order to overcome this problem, one way is to use flow cell which can minimized the photo degradation up to some extent but these measurements again require large volume of analyte which results in increasing the overall radioactivity of the actinide sample, hence inviting activity hazards to experimenters. Thus overall, the TRLIF measurements of actinides do not seem to be a suitable method for reduced activity handling of actinides and hence not appropriate to study the kinetics or thermodynamics of the metal ion interactions with organic ligands.

1.3.2 Gamma ray spectroscopy (GRS)

Most of the actinides and their isotopes produce specific energy gamma rays with varying intensities which provides discrete gamma ray spectrum. Therefore, the gamma ray spectroscopy (GRS) is used as another very sensitive method for trace level detection of radioactive nuclei's. Here the activity constrain in the experiments is relaxed due to the

requirement of small sample amount. Hence, this method has found various applications in nuclear industries, geochemical investigation and astrophysics.

But, the gamma ray spectrum does not get affected due to the chemical interactions of active metal ions, which is basically required to monitor the kinetics of any type of association or dissociation interactions. Hence, the ultra-sensitive GRS methods are also not useful in studying the chemistry of active metal ion complexation with any ligands.

Thus, from the above discussion we can conclude that sensing the metal ion to study its interactions with organic or bio-relevant ligand is very difficult and even not possible with recently developed ultra-sensitive methods. Thus sensing and analyzing the ligand molecule instead of metal ion seems to be the only possible alternative to study the complexation chemistry of metal ions. Therefore, considering the constrains associated with the activity handling in conventional spectroscopy (discussed earlier), we will now extend our discussion over more advanced, single molecule sensitive fluorescence methods and their applications in studying the complexation chemistry of actinides or in general any molecule or ion.

1.4 Applications of single molecule sensitive methods in studying actinides

During past few decades, the unprecedented advancements in optical spectroscopy methods and instrumentations have improved the sensitivity of fluorescence detections up to the level of single molecule. In order to observe a single molecule, a nanomolar solution of analyte is observed under confocal microscopes having the fluorescence detection volume of few femto-liters. Further, use of an intense excitation source and high performance photomultiplier tubes (HP-PMTs) for photon detection produces the detection sensitivity up to the level of single molecules. Therefore, a microliter solution of a few nanomolar concentration of analyte can be analyzed with such single molecule sensitive techniques. This effectively reduces the sample

amount from nano-moles (as used in conventional methods) to femto-moles. Thus, with at least million times reduction possibility in the sample amount we can expect safe handling of actinides for complexation & other interaction kinetics. With this pretext, we will now discuss about the single molecule sensitive correlation spectroscopy.

First of all, in order to study molecular interactions in solution under equilibrium conditions, a solution based single molecule sensitive method known as fluorescence correlation spectroscopy (FCS) is recommended. This method will be different from the conventional TRLIF methods first in terms of monitoring the fluorescent ligand instead of metal ions and second in terms of monitoring the fluorophore interactions in its both excited and ground state. Moreover, in single molecule measurements, all parameters from picosecond to few seconds can be aimed easily with FCS, which gives a wealth of information not only for reaction kinetics but for mechanism too.

1.5 Fluorescence correlation spectroscopy (FCS)

Fluctuation of fluorescence intensity within a tiny observation volume (~ 1fl) under equilibrium condition is evaluated by correlation spectroscopy, generally for the determination of diffusion coefficients and concentration of fluorescent species – the realm of fluorescence correlation spectroscopy. FCS was introduced for the first time in 1972 by Madeg, Elson and Webb[27] and since then FCS has extensively grown and used in determining diffusion coefficient, molecular interactions, triplet state lifetime and rotational dynamics of fluorophore with single molecule sensitivity.[28-30] Fluorescence, being very sensitive and easily recognizable against dark background was used as the basic physical property of a fluorophore in this technique. Any external (diffusion, aggregation, physical or chemical reaction, etc.) and internal (photo-physical) changes in fluorophore which leads to its fluorescence fluctuation are recorded for temporal

correlation. This means all dynamic parameters are reflected in FCS curve with characteristic timescales. And in conjunction with appropriate known model, FCS provides quantitative information for diffusion coefficients, hydrodynamic radii, average concentrations, kinetic chemical reaction rates and singlet-triplet dynamics. FCS and its variants are considered as one of the most sophisticated technique in the study of bio-chemical process with single molecule sensitivity. Here we describe the basic principle of FCS and application in relation to fundamental photophysics of fluorophore and their interactions with other solutes.

FCS records temporal changes in the fluorescence emission intensity as and when single emitters pass through the detection volume. Additionally, while travelling through the excitation-detection volume, the excited fluorophore may also undertake photo-physical paths other than emission by fluorescence for de-excitation, as shown in the simplified Jablonski diagram (see Figure 1.1).

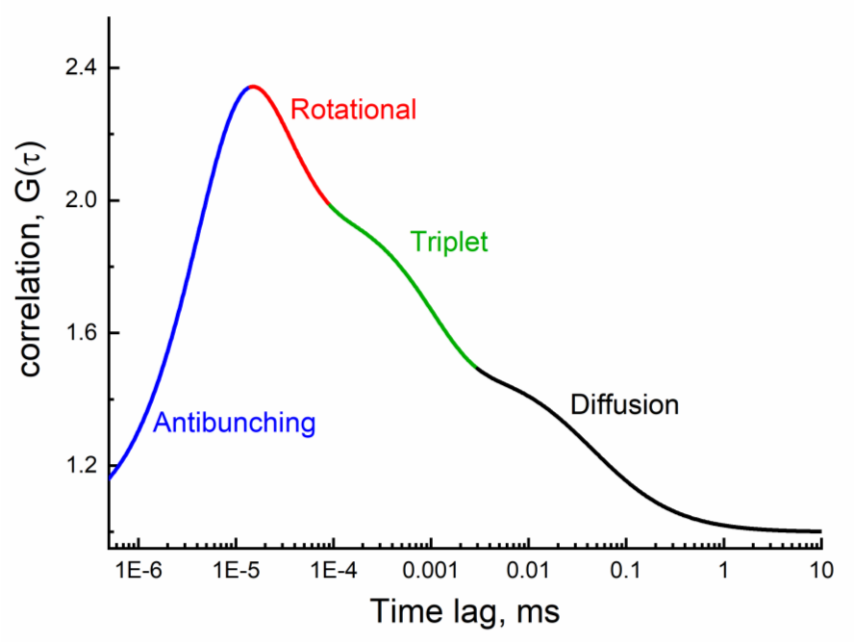

Figure 1.3: Schematic of full FCS curve.

The intensity changes are quantified in their strength and duration by temporally auto-correlating (or cross correlation) the recorded intensity signals, leading to the average number of fluorescent particles in the detection volume and their average diffusion time through the volume. The timescale of fluorescence fluctuation provides information about the kinetics of the underlying processes. For simplicity, a schematic diagram of full correlation curve is shown in Figure 1.3 consisting of expected four types of correlations in a single fluorophore.

Diffusional correlation: Diffusion of a fluorophore through the confocal volume leads to the generation of fluctuating fluorescence signal. The obtained photon statistics or fluorescence fluctuations of fluorophore are correlated at different lag times using equation 1.5 to obtain the correlation function $G(\tau)$ given by[29]

$$G(\tau) = \frac{\langle \delta F(t).\delta F(t+\tau) \rangle}{\langle F(t) \rangle^2} \tag{1.5}$$

The diffusional correlation is observed when fluctuations are correlated at lag times near to the average diffusional time of the fluorophore. However, the photon detection probability reduces from the center of confocal volume to the edges. Therefore 3D Gaussian correlation function is used for analyzing the 3D diffusional part of FCS curve given by

$$G_{Diff}(\tau) = \frac{1}{N.\left(1+\frac{\tau}{\tau_d}\right).\sqrt{1+S\frac{\tau}{\tau_d}}} \tag{1.6}$$

here S is the structural parameter of confocal volume and take cares of its non-spherical (oval) shape over 3D diffusion of fluorophore. The amplitude of diffusional correlation curve is inversely related to the number of dye molecules (N) in the confocal volume hence can be used for quantitative determination of analyte. The diffusion time (τ_D) is inversely proportional to the

diffusion coefficient (D) and is directly proportional to the hydrodynamic radius (r_H) of the diffusing species (will discuss in Chapter 2). Therefore, the interactions of fluorophore with macromolecules like proteins; cyclodextrins, etc. which significantly varies its hydrodynamic radius can be analyzed quantitatively by analyzing temporal variations in the diffusional part of FCS curve.

Triplet correlation: If we enlarge a smaller portion of fluorescence intensity vs. time trace of a very dilute sample, we see bunches of photons separated by an average time equivalent to the triplet state lifetime (see Figure 1.4). Thus, the fluorescence fluctuation arises due to the temporal separation of these bunches results in the additional triplet correlation curve in the FCS. This correlation curve contains information regarding the fraction of fluorophore in the triplet state and their relaxation time. This additional correlation function due to triplet state dynamics is given by[29]

$$G_{Trp}(\tau) = \frac{1 - T + Te^{-\tau/\tau_T}}{1 - T} \tag{1.7}$$

here $\boldsymbol{T}$ represents fraction of molecules which decays through the triplet state and τ_T is triplet state lifetime of fluorophore.

Rotational correlation: Excitation lasers being polarized in nature excites exclusively the molecules whose absorption dipole moment aligns parallel to it. The resulting fluorescence observed also come with specific polarization depending on the emitter's reorientation dynamics. Therefore if a polarizer is placed in front of detector then we further see fluctuation in fluorescence intensity due to rotation of molecular dipole, resulting even faster correlation than triplet state dynamics, as shown in Figure 1.3.[31] Typical rotation time for most of the fluorophore ($\boldsymbol{r_H}$ < 1 nm) in aqueous media lies in < 100 ps timescale which is beyond the resolution of our

current detection system (i.e. 167ps). But if molecule is much bigger in size (> few nm) such as green fluorescent protein, etc. or tagged macromolecules, then one should expect fluctuating signal due to its slower rotation time (~ 10 ns). Rotational correlation can also be seen due to retarded rotation of smaller molecules in highly viscous media, e.g. cellular matrix. The rotation correlation function of fluorophore is given by

$$G_{rot}(\tau) = 1 + K_r e^{-\tau/\tau_r} \tag{1.8}$$

here K_r is a normalizing constant and τ_r is the average rotational time of the fluorophore.

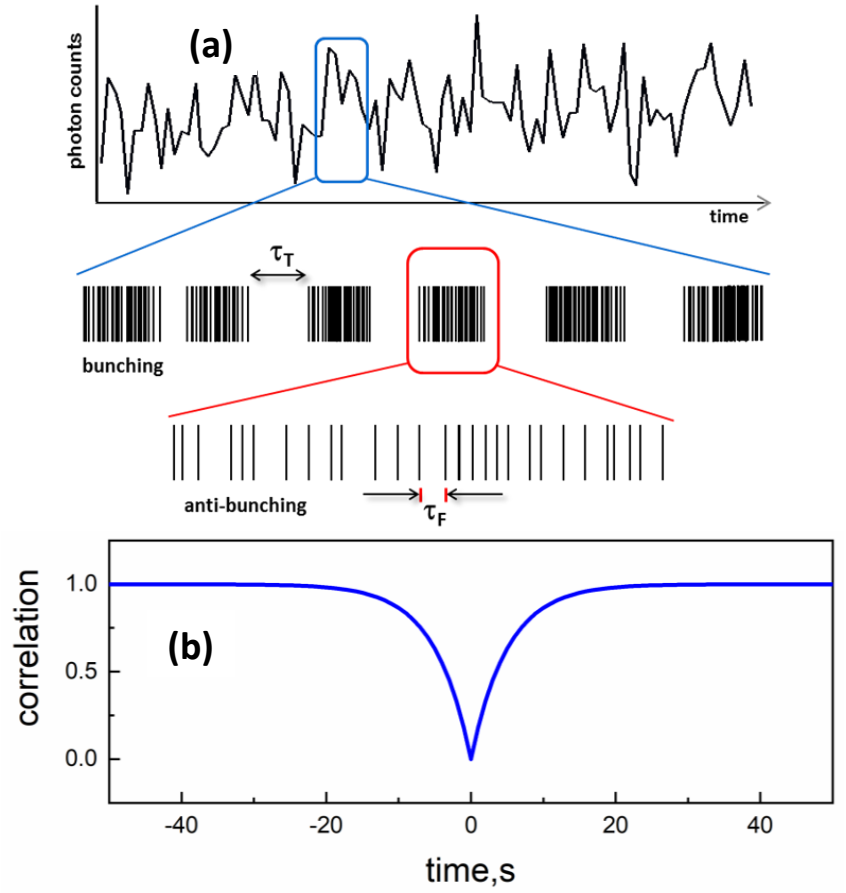

Figure 1.4: Schematic of fluorescence intensity trace vs. time for a very dilute sample under confocal excitation-detection condition (a) and antibunching curves for a single molecule (b).

Photon Antibunching: When we ensure that on average there are very few molecules in the detection volume, then at very shorter time scales below the fluorescent lifetime, correlation

show a downward curvature (see Figure 1.3). If we further expand the photons bunches, as shown in Figure 1.4, we see they are quite separated in time - no two photon events are temporally merged. It is a purely quantum-optical phenomenon and reflects the fact that a single fluorescent molecule cannot emit more than one photon per excitation cycle, which reduces the chance to observe two consecutive photons from one and the same molecule at very short correlation times leading to dip in the correlation amplitude at sub-nanosecond time scales.[31,32] Here two channel cross-correlations is used to overcome detector dead-time (~ 10 ns), the limiting factor in accessing sub-nanosecond correlations.

Short time linear correlation (i.e. nanosecond photon anti-bunching curve) is generally computed by artificially giving positive time shift ($t_s > 0$) to one channel and cross correlating with the other one. This way the whole time interval shown with positive and negative correlation times between t_- ns < t_s < t_+ ns could be calculated. This leads to a typical antibunching dip in the fluorescence correlation curve at very short lag times (τ) – known as photon anti-bunching (see Figure 1.4(b)). Thus FCS encompasses various dynamical events of over 9 orders from sub-nanoseconds to seconds. For a simple two-state system (S_0 and S_1), the correlation curve at very short lag times follows an inverse exponential law as given by

$$G_{ab}(\tau) = 1 - K_{ab} e^{-\tau/\tau_{ab}} \tag{1.9}$$

here $\boldsymbol{\tau_{ab}}$ represents the antibunching relaxation time inverse of which is antibunching relaxation rate. The antibunching relaxation rate ($\boldsymbol{k_{ab}} = \tau_{ab}^{-1}$) is given by the summation of excitation rate (k_{ex}) from ground to the excited state and decay rate (k_d) from the excited to the ground state. Thus, antibunching experiments provide direct access to the de-excitation rate (k_d) of the fluorophore inverse of which is the fluorescence lifetime for an unperturbed fluorescent molecule. However, these rates are expected to be varied in case of some perturbations like

molecular interactions. Thus, being temporal method of analysis antibunching can provide access to study the kinetics of molecular interactions. Therefore, we will now extend our discussion over the applications of FCS in studying the molecular interactions.

1.6 Bimolecular interactions or complexation with FCS

Attractive or repulsive forces between two non-bonded atoms or molecules are termed as molecular interactions whereas the complexation stands for the covalent bonding of the two analyte. These are crucial in diverse fields of protein folding, drug design, material science, sensors, nanotechnology, separations, and origins of life. Mechanism, kinetics and thermodynamics are the three major objectives in studying any type of molecular interactions. Molecular interactions lead to variations in the spectral properties of the analyte which allows their investigations with spectroscopy methods. Therefore, various conventional quantitative methods like fluorescence, absorption, NMR, IR, etc. are being used since decades to study the mechanism and thermodynamics of the molecular interactions. However, their fast and even slow kinetics require separate use of time resolved methods like time correlated single photon counting (TCSPC), fluorescence up-conversion, etc.[25,33-35] In this regard, FCS provides simultaneous time resolved and quantitative estimation of analyte to investigate interaction kinetics.[19,34,36] Besides, sensitivity of FCS allows experiment with very small amount of sample, as required for highly active samples. Hence, it is pertinent to discuss possible implementation of FCS methods in studying various types of molecular interactions.

First of all, FCS is a fluorescence based method which allows the direct measurements for only those interactions where the fluorescence properties of either analyte or fluorescent probe vary during interactions. However, in order to study the molecular interactions or complexation of non-fluorescent analyte, indirect approach via competitive binding among two

analyte and a fluorescent probe is considered. But to properly frame the obtained FCS results to get the kinetics, both of these direct or indirect methods require prior understanding of the reaction mechanism.

Variation in diffusional correlation: There are two variables in the diffusional part of FCS curve. First one is the count rate which is directly proportional to the number of fluorophore in the confocal cavity (***N***) and other one is the average diffusional time (τ_d). Both of these parameters provide quantitative estimation of molecular transformations/interactions. The two possible variations in the diffusional part of FCS curve are shown in Figure 1.5.

Change in the amplitude of FCS curve is observed when the molecular interactions lead to the disappearance of the fluorophore or decrease in its fluorescence yield/brightness, mostly due to stable or irreversible static quenching or the ground state complexation. Therefore, observing the extent of variation in the diffusional part of FCS curve can be useful to determine the thermodynamics of molecular interactions or transformations.

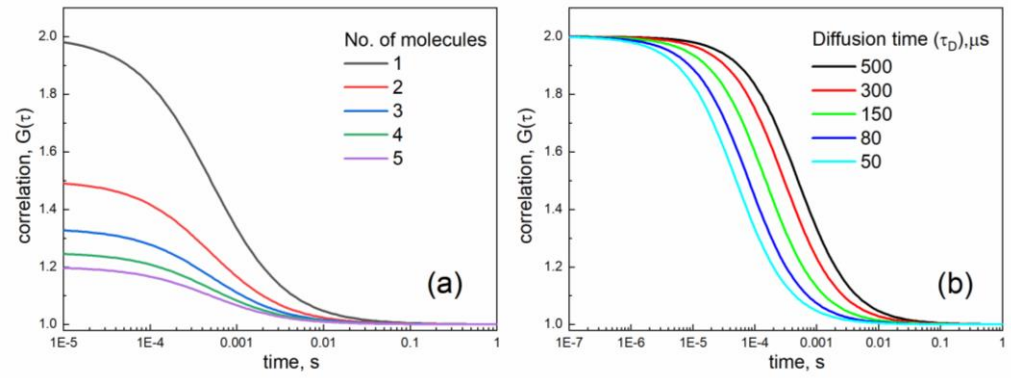

Figure 1.5: Schematic of change in FCS curves with change in number of fluorophore in confocal volume (a) and change in diffusion time (b).

Although, these variations can also be observed in case of photo-bleaching, drying or non-emissive aggregations of the sample with time. Hence, the experiment requires extreme care

and prior understanding of other interfering factors in order to obtain correct thermodynamic aspects of molecular interactions.

Temporal variation in the FCS curve (Figure 1.5b) is observed when the molecular interactions significantly vary the hydrodynamic radius (r_H) of the fluorophore, mainly by interaction with macromolecules. These variations have been mostly used for various biological applications like protein labeling, protein metal interactions, self or induced dimerization or aggregations of fluorophore, host-guest supramolecular interactions, etc.[37-40] However, as these variations requires significant change in the hydrodynamic radius of fluorophore therefore not appropriate to use for binding of relatively small molecules or metal ions. In literature, most of the studies investigate the binding of small fluorophore to large host or macromolecules where $\boldsymbol{r_H}$ variation is significant.

Variation in triplet correlation: Triplet part of FCS also contains two variables: one is triplet fraction (T) which is a quantitative parameter and the other one is triplet time (τ_T) which can be used for determining the kinetics of molecular interactions. The expected independent variations in FCS curve due to these variables are shown in Figure 1.6.

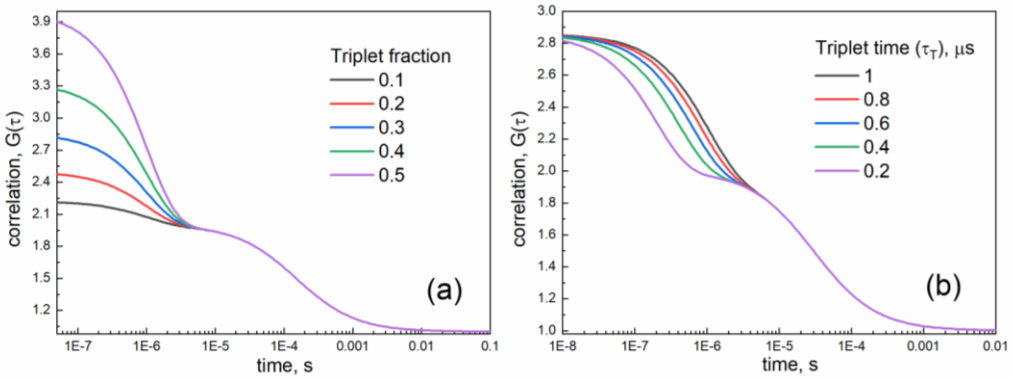

Figure 1.6: Schematic of change in FCS curves with change in triplet fraction $\boldsymbol{T}$ (a) and change in triplet time $\boldsymbol{\tau_T}$ (b).

Amplitude of triplet correlation curve is directly proportional to the fraction of fluorophore (*T*) which de-excite through the triplet state. It is directly dependent on the excitation power of the lasers hence requires stable laser output in order to study molecular interactions. The only change in triplet fraction (*T*) is expected to be observed (Figure 1.6a) when an excited fluorophore gets an alternative path of de-excitation from its S_1 state other than via triplet state such as in case of dynamic quenching interactions of the fluorophore with the other analyte. However, the change in triplet time (τ_T) is observed (Figure 1.6b) in case of dynamic interactions of the triplet state of the fluorophore. Therefore, with a suitable modeling of molecular interactions the classical FCS (bunching) can provide mechanism, kinetics and thermodynamics of molecular interactions involving the triplet state. Besides, variation in these parts (diffusion and triplet) of FCS curve can also be observed while varying various external parameters like the pH, viscosity, temperature, etc. Therefore, suitable solution of reaction medium and environment is essential to perform these interaction experiments.

Variation in triplet time window of FCS curve has also been monitored due to incorporation of additional relaxation rates in the FCS curve. For example, in the study of host guest interactions by Wajih Al-Soufi et. al.[37] using FCS, the incorporation of pyronines inside the cavity of macro cyclic β-dextrin resulted in the variation of both diffusional and triplet part of FCS curves. The change in diffusional curve was due to the change in the hydrodynamic radius of the fluorophore due to binding, hence used to determine the binding equilibrium constant (*K*) whereas, the change in triplet part of FCS curves were observed due to the overall reaction rates (k_+ and k_-). These types of observations can be analyzed by further incorporating new correlation term in FCS given by

$$G_R(\tau) = 1 + K_R e^{-\tau/\tau_R} \tag{1.10}$$

and $$\tau_R^{-1} = k_-(1 + K[H]) \quad (1.11)$$

here τ_R^{-1} represents overall reaction rate and depends upon the concentration of macromolecule or host molecule [H] and thereby used to determining the kinetics of binding (i.e. forward and backward rate constants).

Similar, methods were used by Markus and coworkers in determining the kinetic rate constants for tryptophan interaction with MR121 dye in its ground state.[41] This resulted in highly undesirable values for the sphere of action radius, mainly due to the negligence towards the complex behaviors of FCS curve owing to simplified photoinduced electron transfer (PET) reactions. FCS of PET between an organic fluorophore and a suitable amino acid or nucleobase is a powerful tool to study conformational dynamics in polypeptides, oligonucleotides, etc.[33,34,42,43] The core measurement principle is that PET between the dye and the amino acid or nucleobase quenches the fluorescence of the former, which can be observed as time-correlated intensity fluctuations in FCS. Contrary to Föster resonance energy transfer (FRET) which can measure intermolecular distances between ~2 and ~10 nm, PET is very sensitive on very short length scales, because it requires direct contact formation between the fluorophore and the quencher.[44,45] However, fluorescence quenching by PET is a rather complex result of several distinct interaction mechanisms, and their relative importance primarily depends on the particularities of the chosen fluorophore-quencher pair. Thus, determining kinetic parameters from PET-FCS measurements requires a clear understanding of the underlying interaction mechanisms. Further, as PET reactions are governed by the fluorophore in its excited singlet state. Thus, correlation between nanoseconds to microseconds may not be sufficient to extract reliable kinetic parameter.

Photon antibunching: The first prediction of photon antibunching in fluorescence was made by Ehrenberg and Rigler[31] in their treatment of rotational diffusion in FCS and was experimentally measured by Kask et al.[32] for fluorescent dye molecules in water way back in 1980s. Over the years, photon antibunching has been employed to explore stoichiometry of aggregates and complexes,[46-48] investigate photophysics of dyes,[49] investigation of ground-state proton transfer within the photocycle of a photoacid[50,51] and even sub-diffraction limited quantum imaging.[52] Recently, single molecule FRET (Forster Resonance Energy Transfer) experiments were done by B. Schuler and coworkers[45] using the photon antibunching part of FCS curve for studying the dynamic of protein molecules. Thus, photon antibunching may also be used to study intermolecular PET reactions in the solution. In general, the antibunching relaxation rate (k_{ab}) is given by the sum of excitation (k_{ex}) and fluorescence or de-excitation rate (k_d) of the fluorophore (eq. 1.12)

$$k_{ab} = k_{ex} + k_d \tag{1.12}$$

Thus, any process which varies the decay rate of fluorophore (such as dynamic quenching in the excited state by PET) is expected to be observed in antibunching part of FCS curve as change in antibunching relaxation time.

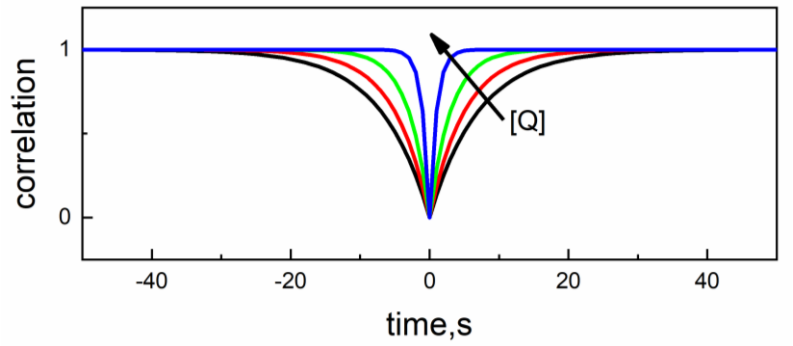

Figure 1.7: Schematic of expected change in antibunching curves due to dynamic interactions in the excited state of fluorophore.

Therefore, we can expect variations in the photon antibunching curves with increasing the quencher concentration [Q] in the solution as shown in Figure (1.7). Thus, kinetics of fast molecular interactions (dynamic quenching) can be studied by monitoring the change in the slop of antibunching curves. Yet, the impending competence of photon antibunching to investigate excited state chemical reactions; more specifically intermolecular fluorescence quenching, has not been endeavoured before due to the absence of suitable methodology. Thus, new methods incorporating photon antibunching part of FCS curve is superior to evaluate such system. Our endeavour is to develop better analysis method to study intermolecular interactions in general with emphasis to metal-ligand complexation. Besides, in order to study the molecular interactions of non-fluorescent or weakly fluorescent materials with heavy metal ion for bio-speciation and sequestration research and for various other applications of single molecule spectroscopy, we need to explore suitable fluorescent chelators along with their well-defined photophysics to avoid any unintentional complicacy for interaction studies.

1.7 Requirement of novel fluorescent chelators

As metal ions are generally non-fluorescent, therefore it is desirable to have fluorescent ligand/chelators which can report about interaction mechanism and dynamics. In this respect we thought of employing carbon nano dots (CNDs); a new class of fluorophore having rich surface functionality as a chelators for metal ions. These materials have attracted enormous attention because of their simple and inexpensive synthesis and also high photostability compared to traditional fluorophores. Their various properties like easy functionalization by chemical modification, high photostability, non-toxicity and so the bio-compatibility makes them serious contender for various applications like bioimaging, light harvesting, optical sensing and in our case for metal ion sensing via complexation with single molecule sensitivity.[53-56]

But, as these experiments (quantitative interactions or complexation) monitor the change in the fluorescence properties of fluorophore, thus a clear knowledge about the photophysics of fluorophore (here CNDs) is prerequisite. In this regard, numerous efforts have been undertaken in past few years to unravel the origin of photoluminescence of carbon dots (CNDs). Among various intriguing aspects, their excitation dependent fluorescence[57] has led to several hypotheses, starting from particle size distribution[58] to the presence of different emissive states[56,59-61] and even to sluggish solvent relaxation around nanodots.[62] Therefore, efforts should be made first to understand the fluorescence origin of these materials followed by their applications for heavy metal sensing and various other single molecule sensitive experiments.

1.8 Objective of the thesis

In this chapter, we discussed how the fluorescence spectroscopy methods provide insights and constrains of activity handling. We highlighted the use of FCS in order to remove the mentioned constrain in the study of actinides followed by a context for the development & analysis of intermolecular interactions. We also highlighted the need of suitable fluorescent marker required in single molecule sensitive applications. Thus, in the present thesis three major objectives are addressed as mentioned below

1) The first objective is to explore FCS over studying the complex fast molecular interactions like photo induced electron transfer or energy transfer occurring both in the excited and ground state of the fluorophore. Followed by the development of suitable methodology to obtain kinetics and mechanism of these interactions.
2) The second objective is to apply these single molecule sensitive methods over studying the mechanism and kinetics of metal ion complexation with fluorogenic ligands to overcome the activity constrains observed in conventional methods.

3) The third and final objective is to explore photophysics of novel fluorescent marker; carbon nanodots and inspect for their applicability for metal ions complexation with FCS.

1.9 Outlay of the thesis

Present thesis contains overall six chapters. Chapter 2 covers the methods, principle and instrumentations of all spectroscopy techniques used in the thesis. Chapter 3 and 4 works on exploring the use of ns-FCS in studying kinetics of fast molecular interactions which meets the first objective of thesis. On the basis of positive results obtained in Chapters 3 and 4; Chapter 5 works on studying the complexation of various metal ions with well-known fluorogenic ligand Calcein, using fluorescence correlation spectroscopy, which covers the second objective of the thesis. Finally, Chapter 6 works on the third objective of thesis where photophysics of fluorescent carbon nano dots have been extensively studied using all spectroscopy methods mentioned in Chapter 2.

CHAPTER 2

Experimental Methods

In this chapter we will discuss basic principles of a few spectroscopy techniques used in current thesis such as UV-visible absorption spectrophotometer, steady-state spectrofluorometry and time correlated single photon counting (TCSPC). There after the principle, instrumentation, and data analysis related to fluorescence correlation spectroscopy is discussed. Besides that, other supportive analytical methods like nuclear magnetic resonance (NMR) spectroscopy and Fourier Transform Infra-red (FT-IR) spectroscopy, imaging techniques like transmission electron microscopy (TEM) & Atomic force microscopy (AFM), have also been briefly discussed.

2.1 UV-visible absorption spectroscopy

All photophysical or chemical processes are initiated by absorbance of light. The absorption spectroscopy monitors the fraction of light absorbed by the substance as a function of light wavelength or frequency. The corresponding generated spectrum is called as absorption spectrum of analyte. Absorption spectrum reflects the ground state properties of analyte and extensively used to determine ground state interactions of the fluorophore.[11,16] Besides, it is also quantitative method thus widely used to determine concentration of unknown samples. In the present thesis, absorption spectroscopy has been used to monitor the ground state interactions of

fluorophore with quencher molecules (or metal ions) and also for the characterization of CNDs. In the present thesis, ground-state absorption spectra were recorded using a double beam UV–visible JASCO model V530 spectrophotometer (Tokyo, Japan). The operating wavelength of the instrument is 200 – 900 nm. The minimum resolution is 0.2 nm with sensitivity up to absorbance of ~0.005.

2.1.1 Instrumentation

The schematic diagram for conventional dual beam steady state absorption spectrophotometer is shown in Figure 2.1.

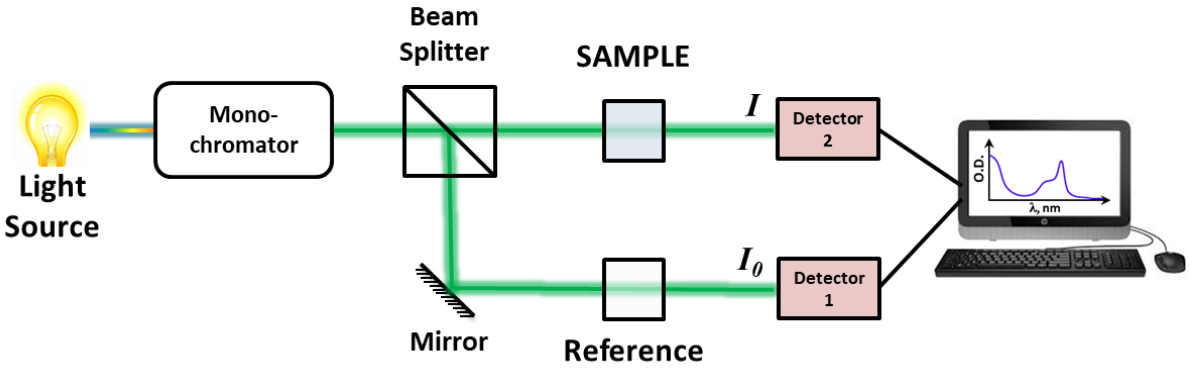

Figure 2.1: Schematic diagram of dual beam absorption spectrophotometer.

It mainly consists of four units; the excitation unit, monochromator, sample and reference chamber and photo detector. Tungsten filament lamp is used for the molecular excitation in the range of 350 – 900 nm (can excite up to 2500 nm) , whereas the deuterium lamp is used for the excitation below 350 nm (up to 170nm). Monochromator is placed in front of source to disperse the white light coming out of the source into individual wavelengths. Thus, light of a particular wavelength is allowed to pass through the monochromator slit to the sample

and reference chamber by 50-50 beam splitter. Solution containing analyte is placed in the sample chamber whereas only solvent is placed in the reference chamber.

The intensity of transmitted light from sample and reference is recorded in the photodetector (200 – 900 nm) as I and I_0 respectively. Logarithmic difference in the intensities of transmitted light between reference and sample is monitored as absorbance or optical density (OD). The process is repeated for all the wavelengths to construct the absorption spectrum as a function of excitation wavelength.

2.1.2 Theory

According to Beer-Lambert law, the relative change in intensity of light due to absorption is proportional to the concentration of the absorbing substance and the length of light path inside the sample. Therefore, if I is the intensity of light, c is concentration of absorbing analyte, dl is length of path travelled by light inside the sample and dI is the corresponding change in intensity then according to Beer-Lambert law

$$\frac{dI}{I} \propto c.dl \tag{2.1}$$

or

$$\frac{dI}{I} = a.c.dl \tag{2.2}$$

here 'a' is a constant of proportionality and known as absorptivity coefficient. Integrating equation (2.2) for intensity limits I_0 to I and length from 0 to l, we get

$$\ln \frac{I_0}{I} = a.c.l \tag{2.3}$$

$$\log \frac{I_0}{I} = \varepsilon.c.l \tag{2.4}$$

here $\log(I_0/I)$ is termed as absorbance or optical density (O.D.) of the substance, ε is known as extinction coefficient of dye and equals to $a/2.303$.

Extinction coefficient is intrinsic property of absorbing substance and varies with excitation wavelength. ε can be determined by monitoring the absorbance of analyte with known concentration and path length. In general, it is defined as absorbance of one molar absorbing substance at 1 cm path length. Absorbance or L.H.S. of eq. (2.4) is a unit less quantity therefore the units for the extinction coefficient are $mole^{-1}\ cm^{-1}$. Extinction coefficient basically defines the probability of analyte excitation at particular wavelength and it is the only quantity which varies with excitation wavelength in eq. (2.4). Thus, the absorption spectrum of sample can also be termed as its extinction spectrum.

2.2 Steady state fluorescence spectroscopy

Spectrofluorimeter is used to record fluorescence spectrum of analyte. It represents intensity of fluorescence as a function of the wavelength of emitted light. Fluorescence Intensity depends upon the concentration, extinction coefficient and fluorescence quantum yields of the fluorescent analyte whereas the spectral shape mainly reflects its excited state properties. In present thesis, the Steady-state (SS) fluorescence spectra were recorded using either HITACHI model F-4010 Spectrofluorimeter (Tokyo, Japan) or HORIBA FluoroMax-4.

2.2.1 Instrumentations

The schematic diagram of steady state fluorimeter is shown in Figure 2.2. It consist of five major units; light source, monochromators, filter holders, sample chamber and photodetector. Xenon arc lamp (more intense than tungsten lamp) is used (range 250 – 600 nm) for continues excitation of the sample. An excitation monochromator is placed in front of source

to selectively excite the sample at particular wavelength. The sample starts populating its excited state and within a fraction of microsecond the steady state is achieved.

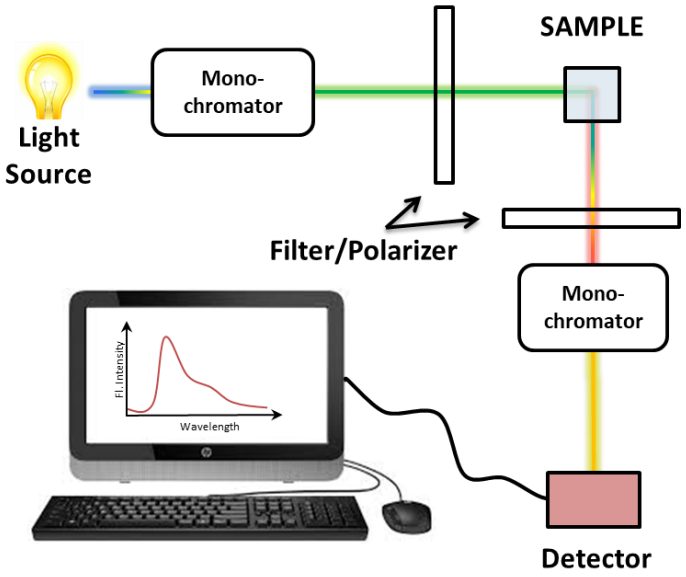

Figure 2.2: Schematic diagram of steady state fluorometer.

The fluorescence from the sample pass through emission monochromator and collected by photo multiplier tubes (PMT) detectors placed at the right angle to the excitation path (to minimize the detection of scattered signal). Thus the fluorescence intensity is recorded as a function of excitation or emission wavelength and generates corresponding fluorescence spectra.

2.2.2 Steady state emission and excitation spectra

In order to obtain the fluorescence emission spectrum, the sample is excited at fixed excitation wavelength (by fixing excitation monochromator) and the corresponding fluorescence intensity is recorded as a function of emission wavelength (using emission monochromator). Emission spectrum describes the excited state properties of the fluorophore. So, any perturbations in the excited state such as exciplex or excimer (excited state complex or dimer) formation is reflected in terms of change in the shape of emission spectrum of the fluorophore.

Further, as intensity of fluorescence is directly proportional to the concentration of fluorophore therefore change in fluorescence intensity can be used to study molecular interactions, excited state pK_a, and aggregation of the fluorophore.[11,16]

On the other hand, the excitation spectrum can be recorded by fixing emission monochromator at particular wavelength (fixed emission) and recording the intensity of fluorescence as a function of excitation wavelength (with rotating excitation monochromator). In ideal cases, the excitation spectrum matches well with the absorbance spectrum for standard dyes like Rhodamine110, coumarin, etc. However for heterogeneous samples the absorbance spectrum may varies from excitation spectrum. In such cases excitation spectrum is preferred over absorbance spectrum and recalled as true absorbance spectra of fluorophore which leads to its emission.

However, the spectrum obtained in conventional fluorometer is not corrected due to various reasons like irregular output of light source at different excitation wavelengths, unequal efficiency of monochromators and detector toward the wavelength and polarization of light. So, a correction factor need to be introduced in order to obtained the ideal fluorescence spectrum of analyte. Concentrated solution (3g/l) of Rhodamine B in ethylene glycol is mostly used as a quantum counter to correct the excitation spectra. This concentrated solution absorbs virtually all incident light from 220 – 600 nm and gives emission maxima at 630 nm. The quantum yield of sample is independent of excitation wavelength in this range (220 – 600 nm) and thus generates a calibration curve (intensity verses excitation wavelength) to correct excitation spectrum. On the other hand, emission spectrum is corrected by recording an emission spectrum of standard compound and compares it with its reported spectrum.

2.2.3 Steady state anisotropy

A polarized excitation of sample (by putting polarizers in front of monochromator) leads to its polarized emission. Extent of polarization in emission is described in terms of the anisotropy (r).[11] It is an intrinsic property of fluorophore and can differentiate two fluorophore in terms of the angle between their excitation and emission dipole moment (β) as represented in Figure 2.3. The steady state anisotropy in terms of β is given by[11] eq. (2.5)

$$r = \frac{2}{5}\left(\frac{3\cos^2\beta - 1}{2}\right) \tag{2.5}$$

β can have values from 0 to π therefore anisotropy can be in the rage of $-0.2 < r < 0.4$. r is zero for $\beta = 54.7^0$, known as magic angle where anisotropic effects are zero.

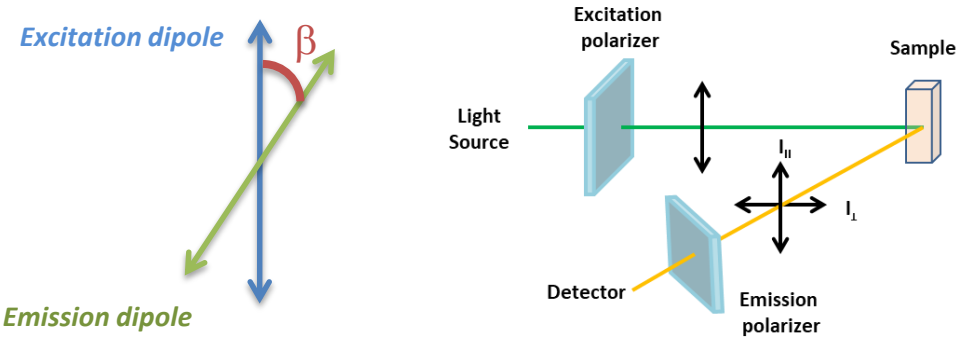

Figure 2.3: General representation of excitation and emission dipoles of fluorophore and Schematic diagram of polarized excitation and emission of the sample.

The steady state anisotropy can be measured with the same fluorometer setup just by additionally incorporating excitation and emission polarizers in the mentioned space (Figure 2.2 & 2.3). In order to restrict the rotational depolarization of fluorophore, the steady state anisotropy measurements are made in highly viscous (eg. glycerol) media. Thus for the vertical

polarized excitation, the fluorescence intensity at both horizontal and vertical polarization is recorded to obtain steady state anisotropy of the sample by the relation[11]

$$r = \frac{I_{VV} - GI_{VH}}{I_{VV} + 2GI_{VH}}; \qquad G = \frac{I_{HV}}{I_{HH}} \tag{2.6}$$

here G represents the correction factor, which is required to normalize different transmitting efficiency of emission monochromator toward parallel and perpendicular polarized emission. I_{VV} and I_{VH} represent vertical polarized excitation and corresponding vertical and horizontal polarized emission.

Steady state anisotropy can be measured in two ways; excitation anisotropy and emission anisotropy. For a particular emission spectrum, the emission anisotropy is not dependent on the emission wavelength as emission always occurs from the lowest singlet state. But, we can expect different emission anisotropy values if there are more than one emissive states of the sample. On the other hand, excitation anisotropy hugely depends on the wavelength of excitation and increases gradually with increasing excitation wavelength. Thus, the excitation anisotropy is maximum (r~0.4 or β=0) near the longest possible excitation wavelength (~ wavelength of emission maxima). However, a sudden change in excitation anisotropy is expected in case of multiple fluorogenic centers in the sample hence can be used to define multiple electronic states in the system. Thus, in the present thesis, steady state emission spectra, excitation spectra and excitation anisotropy has been used as an elegant method to study the photophysical behaviour of fluorophore. Besides, conventional time resolved fluorescence methods have also been widely used to study excited state phenomenon. Basic principle, instrumentation and applications of conventional time resolved fluorescence methods is discussed ahead.

2.3 Time resolved fluorescence spectroscopy with time correlated single photon counting (TCSPC)

2.3.1 Introduction

Fluorescence lifetime (FL) is an average time spent by an excited fluorophore in its excited singlet state or spent to fluoresce back to its ground state. FL is very sensitive property of fluorophore and used to study excited state perturbations in the system. Therefore, molecular interactions occurring in the excited state of the fluorophore can be easily studied using fluorescence lifetime measurements provided that the rate of interactions is more than the rate of fluorescence. One such type of interactions is the quenching by PET reactions between excited fluorophore and quencher molecules. As the rate of ET interactions (k_{et}) is very high so the overall quenching rate (k_q) depends on the mutual diffusion rate (k_d) of the reactant molecules ($k_q^{-1}=k_d^{-1}+ k_{et}^{-1}$) to form an encounter complex. So the interactions are diffusion controlled and also called as dynamic interactions. Stern Volmer plots are used to determine the collisional or dynamic quenching rate constant. In the present thesis, PET interactions have been studied extensively using TR TCSPC measurements. Therefore, in this section we will briefly discuss the instrumentation and working principle of TCSPC setup.

In present thesis, the nanosecond fluorescence decays were measured using diode laser based TCSPC setup (IBH, UK). A special PMT detector (IBH, UK) was used for the fluorescence decay measurements. The instrument response function for this setup is ~180 ps to 1.1 ns depending upon the excitation lasers. For lifetime measurements, fluorescence decays were recorded at the magic angle (54.7°) with respect to the vertically polarized excitation light to negate anisotropic effects. All the experiments were carried out at ambient temperature, 25 ± 1^0C unless otherwise mentioned.

2.3.2 Principle and Instrumentation of TCSPC

The TCSPC instrument works over the single photon counting principle.[11] The schematic diagram for TCSPC setup is shown in Figure (2.4). Pulsed lasers (peak energy ~1pJ) are used to excite the sample in TCSPC. An excitation pulse in the excitation laser split into two parts; one optical pulse excites the sample whereas the other part generates an electrical START pulse, which is then routed through a constant fraction discriminator (CFD) to the START input of the Time to Amplitude Convertor (TAC) to initialize its charging operation (see Figure 2.4). Function of CFD is to measure the arrival time of the photoelectron pulse with the highest possible time resolution.

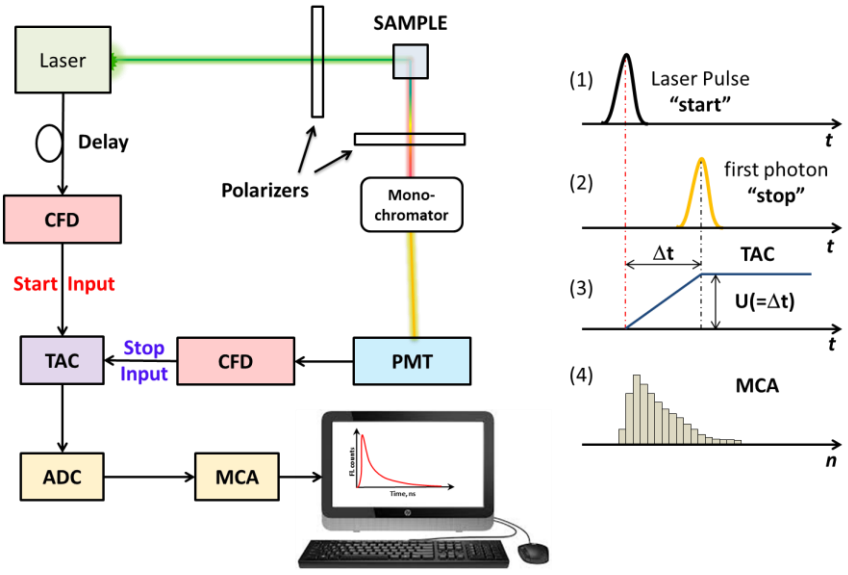

Figure 2.4: Schematic diagram of TCSPC setup. Here, CFD is constant fraction discriminator, TAC is time to amplitude convertor, ADC is analog to digital convertor and MCA is multichannel analyzer. Schematic on right has been adopted from 'Optical Spectroscopy - Methods and Instrumentation' by N. V. Tkachenko.

The optical pulse excites the sample which results in the emission of photons. These photons are then detected by a PMT (photo multiplier tube photodetector) to generate electrical STOP pulses. The STOP pulses then pass through another CFD and then to the time to amplitude

converter (TAC). TAC immediately stops its charging operation on receiving the stop signal and generates an electrical output having amplitude proportional to the time difference (Δt) between the START and STOP pulses reaching the TAC. The TAC output electric pulse is then fed to the input of a Multichannel Analyser (MCA) through an analog to digital converter (ADC). Function of ADC is to generate a numerical value corresponding to the pulse height of TAC output signal and select an appropriate address (channel) of MCA and add a count in this address. This cycle repeats for large number of times and as a result a histogram of counts against the channel number of MCA is generated (see Figure 2.4). The channel numbers are then mathematically converted into time with a proper time calibration and thus we get a fluorescence counts or intensity verses time plot i.e. time resolve fluorescence spectrum of the sample.

TCSPC don't require strong excitation light source as pulse energy of few pJ is sufficient to provide emission intensity close to the maximum acceptable value for samples of reasonable quantum yield. The characteristics of lasers which actually matter here the most are pulse width and repetition rate. The pulse width of laser determines the time resolution and ideally should be shorter than 10ps so that it won't be the limiting part of the instrument. High repetition rate (~ 10 – 50 MHz) is preferable for fast signal collection. However, very high repetition rate is not acceptable in case of probes having long lifetime (so should be optimized accordingly). In the detection part, MCP (micro channel plate) PMT (detection range 200 – 1000 nm) provide tenfold shorter pulsed width than any other PMT thus can provide time resolution ~ 25 ps. Avalanche photodiode (APD) possess little lower time resolution (> 100ps) and can be used for range 300-1100 nm. However, in general PMTs are used in most of the TCSPC setups. The factor that limits the time response of PMT is its transit time spread (TTS). It is the

distribution of transit times through the detector and for most phototubes it is nearly 2 ns. It can be reduced up to 1ns by carefully designing the PMTs. For MCP PMTs it is around <50ps.

2.3.3 Theory

For a sample having only one type of fluorogenic emitter the decay in the intensity of fluorescence follows first order kinetics. For instance, if I_0 represents the intensity at the moment of excitation and I is instantaneous intensity then

$$I = I_0 e^{-k_f t} \tag{2.7}$$

or

$$\ln(I) = \ln(I_0) - k_f t \tag{2.8}$$

here k_f represents the average decay rate or fluorescence rate of the sample inverse of which is the fluorescence lifetime (τ_f). Therefore, fluorescence intensity (I) of sample becomes *1/e* of the initial intensity at the fluorescence lifetime of the fluorophore. In ideal cases, when the sample is excited using a δ pulse and also the response of the detection system is instantaneous; the observed decay curve would represent the true fluorescence decay of the sample.

However, due to finite time width of the lasers and certain response time of the detection system, the observed decay curve *R(t)* is in fact a convolution of the true decay curves *I(t)* and the effective time profile of the excitation pulse *E(t)* given by

$$R(t) = \int_0^t E(\tau) I(t-\tau) d\tau \tag{2.9}$$

here *I(t)* represents the fluorescence decay function with δ pulse excitation and *E(t)* is the excitation pulse profile called as instrument response function (IRF). *E(t)* and *R(t)* can be experimentally measured. During analysis, decay function *I(t)* is assumed for the sample and this function is convoluted with the observed *R(t)* to obtain the calculated (fit) curve *Y(t).* The

variables in the function *I(t)* are changed iteratively until a best fit between the *Y(t)* and *R(t)* is obtained. The function *I(t)* is assumed to be a sum of exponentials given by

$$I(t) = \sum B_i \exp(-t/\tau_i) + A \tag{2.10}$$

here B_i represents the pre-exponential factor for the i^{th} component, τ_i is corresponding fluorescence lifetime and *A* is a correction term. The success of an analysis is determined from the following statistical parameter

$$\chi_r^2 = \frac{\sum_{i=1}^{n} \frac{1}{\sigma_i^2}\left[R(i) - Y(i)\right]^2}{n-p} \cong \frac{\chi^2}{n} \tag{2.11}$$

here σ_i^2 is the weighting factor of the counts in the i^{th} channel, *p* is the number of floating parameters and *n* is the number of data points. From Poisson statistics the standard deviation σ_i^2 is known to be the square root of the number of photon counts in TCSPC given by

$$\sigma_i^2 = \sqrt{R(i)} \tag{2.12}$$

In general, the function *I(t)* is assumed to be either a mono-exponential or a bi-exponential function and for each of these cases the parameters, B_i, τ_i and *A* are varied as long as a minimum value of Chi-square is obtained. For only random errors, the value of Reduced Chi-square is expected to be near unity however the first step to judge the fit is a visual comparison of the data and the fitted function along with virtual examination of the residuals which is difference between the measured data and fitted function.

2.4 Fluorescence correlation spectroscopy (FCS)

In the present thesis, fluorescence correlation spectroscopy has been used to study mechanism and kinetics of small molecular interactions with single molecule sensitivity. We

have already discussed about this method and its applications in Chapter 1. In this section, we will discuss the principle, instrumentation and analysis of FCS spectrum.

The experimental setup for FCS (and photon antibunching) experiments is based on epi-fluorescence detection microscopy (LSM 710, Carl Zeiss GmbH) with external two Hybrid PMT detectors (HPM-100-40, Becker & Hickl GmbH, Berlin, Germany) connected to DPC-230 correlator card (Becker & Hickl GmbH, Berlin, Germany) for recording photon streams with high temporal resolution (165ps) and generation of second order correlation functions ($G_{ab}(\tau)$). FCS measurements are performed on aqueous solutions of dye in Lab-Tek chambers, using a water immersion objective, 63x 1.2 NA. Sample temperature was controlled by a Zeiss (Jena, Germany) Temperature Modules and objective heater (PeCon, Germany).

2.4.1 Principle and Instrumentation of FCS

Figure 2.5 represents a schematic diagram of two detector based FCS setup used in our experiments. A few microliter samples of nearly nanomolar concentrations is placed on the cover slip (thickness ~ 0.13 – 0.17 mm) above the high numerical aperture (>1.1) microscope objective. An excitation beam of CW or pulsed laser passes through the objective to the sample for excitation. Fluorescence photons from the sample are thus collected by epifluorescence via same objective. An appropriate dichroic mirror is placed below the objective to separate the scattered laser light from the obtained fluorescence. Transmitted fluorescence photons then focused on confocal pinhole to reduce the observation volume. The pinhole permits passing fluorescence photons from the confocal volume only by nearly eradicating all other scattering photons as shown in Figure 2.5. Thus the size of pinhole defines the axial resolution of a confocal microscope. Typical dimension of a confocal volume lies in femtolitre, thus sample of sub nanomolar (nM) concentration result on an average nearly one molecule at any instantaneous

time in the confocal volume. This ensure signal from a single molecule and pinhole plays the role of heart in confocal microscope by rejecting background signal and thus improving S/N ratio.

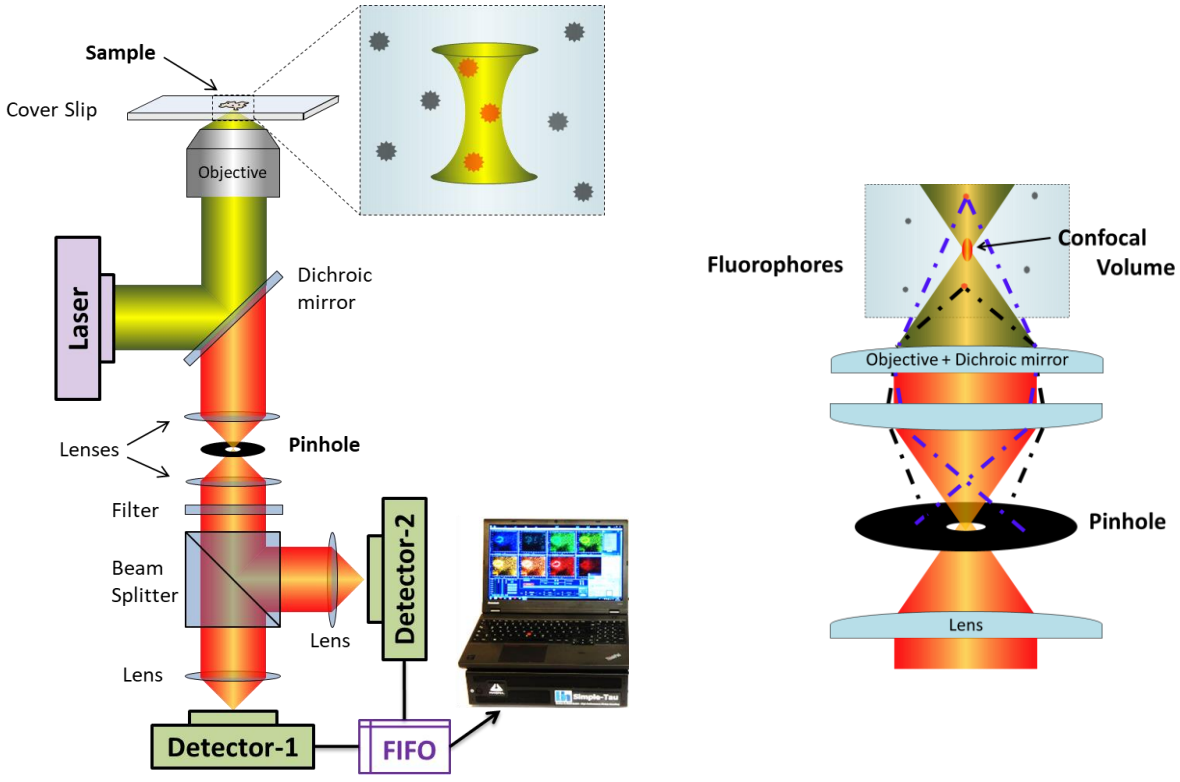

Figure 2.5: Schematic diagram of confocal microscope (left) used for FCS measurements. Confocal principle is depicted on the right side.

The transmitted fluorescence light from the pinhole then passed through an additional long pass filter to cut out scattered laser light further (if any). Ultimately that fluorescence photon beam is then equally divided into two beams and directed to two high performance PMT detectors. These detectors are connected to the FIFO (first in first out) electronics that records macro-time (i.e. time of photon arrival w.r.t. start of experiment), micro-time (i.e. time of photon arrival w.r.t. the previous excitation pulse) and detector where the photon is registered. Macro-

time is used to correlate intensity fluctuations in FCS whereas micro-time provides fluorescence lifetime information (when excited with pulsed laser).

A single photodetector in principle can also be used to generate correlation curve for lag time above its dead time (the average time taken by it after first photon detection to get ready for the second photon detection). The dead time for most of the detectors lies in range of few nanoseconds (~10 ns). Thus obtaining a nanosecond correlation is very difficult with single detector. In this regard two detectors are used to sense two consecutive photons and time resolution reduces to few picoseconds (~160 ps) from nanoseconds. In this case cross-correlation among two detectors is used to generate the correlation curve which additionally improves the S/N ratio by non-correlating intrinsic noise of detectors.

2.4.2 Theory

Fluctuation in fluorescence intensity arises when a fluorophore diffuses through the confocal volume as shown in Figure 2.6.

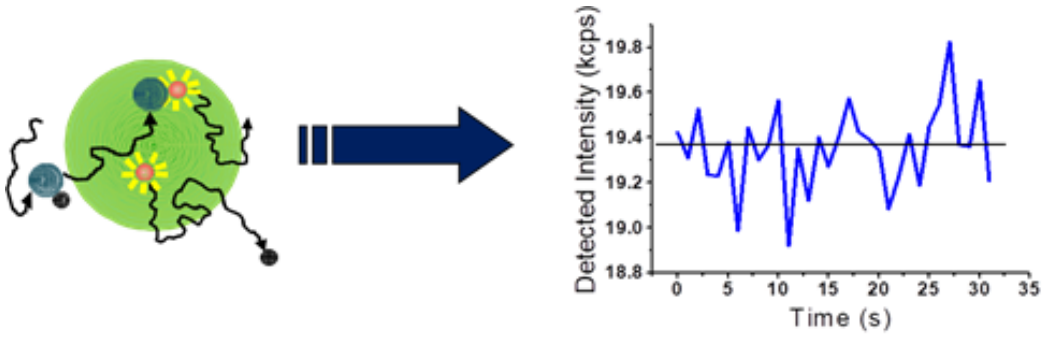

Figure 2.6: Schematic diagram of fluorescence fluctuations due to Brownian motion of fluorophore (top view of confocal volume) and corresponding data of ***F(t)***. Some part of this figure is adopted from the available presentations on the Internet (from www.its.caltech.edu).

If $\langle F \rangle$ is the average fluorescence intensity observed and F is fluorescence intensity at any instantaneous time t then the fluctuation in fluorescence intensity at that time is given by

$$\delta F(t) = F(t) - \langle F \rangle \tag{2.13}$$

The normalized correlation function G(τ) which correlates fluorescence fluctuation at time *t* and after a lag time τ is given by

$$G(\tau) = \frac{\langle \delta F(t) \cdot \delta F(t+\tau) \rangle}{\langle F(t) \rangle^2} \tag{2.14}$$

The diffusional motion of fluorophore through the confocal volume is the most common cause of fluorescence fluctuation (governed by a specific diffusion coefficient, which in turn depends on its size). Thus the correlation function corresponding to the diffusional motion of fluorophore can be derived, considering the oval shape of confocal volume (with r_0 as lateral and z_0 as axial diameter), concentration of analyte (C) and its averaged diffusion time τ_d and given by

$$G_{diff}(\tau) = \frac{1}{V_{eff} \langle C \rangle \left(1 + \frac{\tau}{\tau_D}\right) \sqrt{1 + \left(\frac{r_0}{z_0}\right)^2 . \frac{\tau}{\tau_D}}} \tag{2.15}$$

here V_{eff} represents the effective confocal volume and given by

$$V_{eff} = \pi^{\frac{3}{2}} . r_0^2 . z_0 \tag{2.16}$$

Diffusion time (τ_d) is related to the diffusion coefficient (*D*) of fluorophore by the relation

$$\tau_D = \frac{r_0^2}{4.D} \tag{2.17}$$

and the diffusion coefficient (D) is related to the hydrodynamic radius (r_H) of the fluorophore by relation

$$D = \frac{kT}{6\pi\eta r_H} \tag{2.18}$$

Thus, the hydrodynamic radius of fluorophore can be calculated using eq. (2.18) by recording the correlation curve of fluorophore and fitting with eq. (2.15) to get τ_d (and so the value of D). Further, as the product of V_{eff} and C represents the number of fluorescent entities (N) in confocal volume therefore eq. (2.15) reduces to

$$G_{diff}(\tau) = \frac{1}{N} \cdot \frac{1}{\left(1 + \frac{\tau}{\tau_D}\right)} \cdot \frac{1}{\sqrt{1 + \left(\frac{r_0}{z_0}\right)^2 \cdot \frac{\tau}{\tau_D}}} \tag{2.19}$$

Now for lag time $\tau = 0$, eq. (2.19) reduces to

$$G_{diff}(0) = \frac{1}{N_{eff}} = \frac{1}{V_{eff}\langle C \rangle} \tag{2.20}$$

or

$$\langle C \rangle = \frac{1}{V_{eff} G_{diff}(0)} \tag{2.21}$$

Therefore according to equation (2.21), the inverse of amplitude of $G(\tau)$ at lag time $\tau \rightarrow 0$, where no fluorescence fluctuations are observed due to diffusion of fluorophore directly gives information about the number of particles in confocal volume. Hence by knowing the size of effective confocal volume, one can determine the concentration of fluorophore with FCS without knowing their extinction coefficient (required in absorption spectroscopy). The effective volume for a confocal microscope can be estimated by recording FCS of a standard dye (eg. Rh110, Atto488, etc.) of known diffusion coefficient and using equations (2.15, 2.16 & 2.17).

Now, as discussed in Chapter 1, below the time scale of sub millisecond one can further observe positive correlation in FCS curve due to the additional fluorescence fluctuations arising because of the photo physics of fluorophore (eg. blinking due to triplet state relaxation). Let us consider a simple bright (B) and dark (D) state of the fluorophore where dark state can be assumed as its triplet state.

$$B \xrightarrow{k_D} D \quad \& \quad \mathrm{D} \xrightarrow{k_B} B$$

If T represents the fraction of triplet or dark state then T is given by

$$T = \frac{k_D}{k_D + k_B} \tag{2.22}$$

here k_D and k_B are corresponding rate constants of transformation from bright to dark and dark to bright state respectively. But in case, if triplet state is not completely dark then T is given by

$$T = \frac{k_D k_B \left(\eta_B - \eta_D\right)^2}{\left(k_D + k_B\right)\left(k_D \eta_D^2 + k_B \eta_B^2\right)} \tag{2.23}$$

here η_B and η_D represents the fluorescent quantum yield of bright and dark state respectively.

As T represents the fraction of dark state therefore (1-T) represents the fraction of bright state. Thus, for one fluorophore, the triplet state blinking can be represented as a simple exponential decay function given by

$$G_{trip}(\tau) = \frac{(1 - T + T.e^{-\tau/\tau_T})}{(1-T)} \tag{2.24}$$

here τ_T represents the average triplet relaxation time of fluorophore. Thus, including the triplet correlation function, the overall correlation function is given by

$$G(\tau) = G(\infty) + \frac{1}{N} . \frac{(1 - T + T.e^{-\tau/\tau_T})}{(1-T)} \cdot \frac{1}{\left(1 + \frac{\tau}{\tau_D}\right)} \cdot \frac{1}{\sqrt{1 + \left(\frac{r_0}{z_0}\right)^2 \cdot \frac{\tau}{\tau_D}}} \tag{2.25}$$

Further, as discussed earlier (in Chapter 1), an additional correlation may appear near sub nanoseconds time scale, due to the rotational fluctuation of the fluorophore. However, It generally occurs only in case of highly viscous media or large size fluorophore (>5 nm) like fluorescent proteins (or tagged proteins). This additional correlation can be expressed in simple exponential decay function as

$$G_{rot}(\tau) = (1 + K_{rot}.e^{-\tau/\tau_{rot}}) \tag{2.26}$$

here K_{rot} defines the amplitude of correlation function due to the rotational motion of molecule and τ_{rot} is the average rotational time of the fluorophore.

The timescale of rotational correlation highly depends upon size of fluorophore and solution viscosity. This may also get merged with triplet correlation part of FCS curve. However, the rotational correlation can be easily distinguished from triplet state by performing power dependent FCS measurements. The fraction of triplet state (*T*) directly depends upon the excitation power. Therefore, increasing the excitation power increases the amplitude of triplet state (relate to *T*) without affecting the rotational correlation curves thus can be easily differentiated.

Now at the nanosecond time scale the fluorescence fluctuations are recorded due to inherent photophysics of the fluorophore. Here molecule behaves like a quantum emitter and the time resolved occurrence of consecutive photons is correlated. At very short lag time ($\tau \rightarrow 0$ ps), the probability of getting consecutive photon for a single fluorophore is zero and this probability increases with increase in the lag time as next excitation and emission cycle sets in. Thus the obtained correlation curve contains information regarding the excitation and fluorescence rate of the fluorophore (discussed in Chapter 1). This part of FCS curve is known as photon antibunching and represented as the decay function of fluorophore by relation

$$G_{ab}(\tau) = (1 - K_{ab}.e^{-\tau/\tau_{ab}}) \tag{2.27}$$

here K_{ab} represents normalizing factor and associated with the average number of fluorescent molecules inside the confocal cavity. τ_{ab} is the antibunching relaxation time which is related to excitation and fluorescent rate of the fluorophore by the relation

$$\tau_{ab}^{-1} = k_{ab} = k_{ex} + k_f \tag{2.28}$$

So for a single type of fluorescence emitter in the confocal volume the overall correlation curve is defined as

$$G(\tau) = G(\infty) + G_{diff}(\tau)G_{trip}(\tau)G_{rot}(\tau)G_{ab}(\tau) \tag{2.29}$$

However, in case of more than one type of fluorescence emitter in the solution, the overall correlation function is given by addition of their individual correlation functions (G_1, G_2,..

etc.) as eq. (2.30)

$$G_{total}(\tau) = G_1(\tau) + G_2(\tau) + G_3(\tau) + ... \tag{2.30}$$

In present thesis, FCS experiments were performed in water with small size fluorophores (r_H < 0.5 nm). Therefore, contribution from the rotational correlation has not been expected and so has not taken in the analysis of FCS curve. Further, besides eq. (2.27), proposed kinetic models have also been used to fit the antibunching part of correlation curves in Chapters 2 and 3. Further, besides fluorescence techniques, various other spectroscopic/microscopic methods have also been used in current thesis for the characterization of newly synthesized carbon nanodots and briefly discussed ahead.

2.5 Brief introduction and characteristics of other used techniques

2.5.1 Infra-red absorption spectroscopy (IR)

Infrared spectroscopy is also known as vibrational spectroscopy in which matter is studied for its interactions with the infrared radiation. Vibrational spectroscopy is used to identify the types of bonds thus functional groups present in the system. Different functional groups require/absorb different energy IR-radiation to vibrate under specific vibrational modes.

Therefore, depending upon the types of functional groups present in the sample a typical IR spectrum is generated as absorbance verses IR- frequency in cm^{-1}. Therefore, it is an absorption based spectroscopy and the instrument used for this technique is called as infrared spectrometer. Fourier transform-IR spectrophotometers are used instead of normal IR-spectrophotometer to increase the scan rate of the instrument. In present thesis, IR-spectrophotometer is recorded to characterize the surface functional groups of carbon nanodots with Bruker Tensor III Fourier transform IR-spectrophotometer (FT-IR).

2.5.2 Nuclear magnetic resonance (NMR) spectroscopy

NMR spectroscopy is a technique to observe local magnetic fields around atomic nuclei. In this, the sample is analysed under strong magnetic field by excitation of active nuclei (having integral spin) with radio waves. The surrounded intermolecular magnetic fields around the active nuclei effectively changes the resonance frequency, thus provide details of local environment around it. Therefore, NMR is extensively used for mostly in identification of compounds like proteins, complex molecules, etc.

The most commonly used NMR is ^{1}H and ^{13}C-NMR spectroscopy but it can be applied to any kind of materials having spin active nuclei in it. In the present thesis, NMR spectroscopy has been used for comparing the characteristics of carbon nanodots with molecular fluorophore (Citrazinic acid). For this measurements ^{1}H-NMR spectra were recorded on 500 MHz (Varian), using DMSO-d6 as solvent for the characterization of synthesized carbon nanodots sample.

2.5.3 Transmission electron microscopy (TEM)

Transmission electron microscopy is technique in which a beam electron is focussed on a thin specimen to form an image. The thickness of specimen generally lies below 100 nm. Electron transmits through the sample and makes an image which is then magnified and focused

onto an imaging devise. Imaging devise could be a fluorescent screen or layer of photographic plates or a scintillator attached to a charge-coupled device (CCD). The resolution or TEM is relatively very high (few nm) as compare to light microscopes (> 200 nm for confocal microscope). It is due to the short de-Broglie wavelength of the electrons. Thus particles of very small size (~nm) can be imaged for determining their size and internal structure. In the present thesis TEM has been extensively used to study the internal structure and size of fluorescent carbon nanodots. For this, we have used Carl Zeiss Libra 120 kV and 200kV transmission electron microscope at an accelerating voltage of 120kV and 200kV for normal and high resolution TEM imaging of carbon nanoparticles.

2.5.4 Atomic Force microscopy (AFM)

Atomic force microscopy (AFM) is a kind of scanning probe microscopy (SPM) having resolution on the order of sub nanometer. It consists of a cantilever with a sharp tip at its end that is used to scan the specimen surface. The tip brought into the proximity of the specimen and the forces between the tip and specimen leads to the deflections in the cantilever. Extent of deflections is proportional to the height of sample which represents its size. Although, AFM is mostly used to study the surface related properties of samples for example mechanical properties like stiffness or adhesion strength and electrical properties such as conductivity or surface potential. But in the present thesis we have used AFM for determining the size distribution of synthesized carbon nanodots. For this, the carbon dot sample was loaded on mica plates and AFM images were recorded with Solver P47 from NT-MDT, Russia.

CHAPTER 3

Kinetics of Rh110 & Aniline Interaction

3.1 Introduction

Conventional studies of fluorescence quenching use time resolved (TR) and/or steady-state (SS) ensemble spectroscopy and Stern-Volmer (SV) analysis,[11,16] but these measurements cannot disentangle all the described mechanism and quantify all the involved reaction rates and rate constants. Additionally, experimental constrain associated with the handing of radioactive materials also limit its use in studying complexation kinetics of actinides with fluorogenic ligands (as discussed in Chapter 1).

In this regard, single molecule sensitive fluorescence correlation spectroscopy (FCS) and, in particular, its nanosecond part known as fluorescence antibunching can be used to fully elucidate the complex reaction scheme. The photon antibunching relaxation rate for a fluorophore is given by sum of the excitation rate (k_{ex}) and decay rate (k_d) of the fluorophore (eq. (3.1)).

$$\tau_{ab}^{-1} = k_{ex} + k_d \tag{3.1}$$

Therefore, as explained in Chapter 1, dynamic interactions in the excited state of the fluorophore which varies its decay rate can be studied using photon antibunching part of FCS curve. However, for more complex systems where fluorescent molecule undergoes static and dynamic quenching by a quencher moiety Q along with its triplet state photophysics, the antibunching part of an FCS curve becomes much more complex, but also contains much more information than conventional ensemble measurements.

Thus, in this chapter, we will explore potential of FCS in studying complex intermolecular interactions and present a novel fluorescence spectroscopic method, which combines fluorescence antibunching, TCSPC, and steady-state emission spectroscopy, to study chemical reactions at the single molecule level.

We exemplify our method on investigating intermolecular fluorescence quenching of Rhodamine110 by aniline. Here Rh110 is selected as a fluorophore due to its high quantum yield and water solubility whereas aniline is used as quencher molecule due to its high dynamic quenching rate with Rh110 and also good solubility in water. We will demonstrate that the combination of measurements of fluorescence antibunching, fluorescence lifetime and fluorescence steady state intensity, captures the full picture of the complex quenching kinetics which involves static and dynamics quenching, and which cannot be seen by steady-state or lifetime measurements alone.

3.2 Experimental details

3.2.1 Materials

Rhodamine 110 was a gift from M/s B&H GmbH. Aniline was procured from M/s. S.D Fine Chemicals and was freshly distilled before use. HPLC grade water from Sigma was used for solution preparations. Very dilute solution of freely diffusing Rh-110 in water (~ 1 nM) has been

used for the photon antibunching and regular FCS measurements. For ensemble spectroscopic investigations, Rh110 concentration was kept at around 1 μM.

3.2.2 Methods

Ground-state absorption spectra were recorded using a JASCO model V530 spectrophotometer (Tokyo, Japan). Steady-state (SS) fluorescence spectra were recorded using a HITACHI model F-4010 spectrofluorimeter (Tokyo, Japan).

The nanosecond fluorescence decays in the absence and presence of the quencher were measured using a diode laser (454 nm, <100 ps, 1 MHz) based TCSPC setup (IBH, UK). In the present work, a MCP-PMT detector (IBH, UK) was used for the fluorescence decay measurements. The instrument response function for this setup is ~130 ps at FWHM.

FCS and photon antibunching experiments were carried out on a LSM 710 confocal microscopy setup with 488 nm CW excitation equipped with a water immersion objective, 63x 1.2 NA. The collected fluorescence photons were focused through a 70 micron diameter pinhole and distributed on two dedicated detectors (Hybrid PMT's from B&H GmbH) by a polarizing beam splitter at the output port of the LSM scan head. The detectors are connected to a dedicated multichannel recorder, DPC-230 from B&H GmbH, which records photon arrival times with a time bin of 165 ps.

3.3 Results and discussion

3.3.1 Photophysics of Rh110 with photon antibunching

In the absence of any quencher, the antibunching part of the FCS curve, as shown in Figure 3.1, is described by a simple exponential law, $1 - \exp(-t/\tau_{ab})$, where the inverse antibunching relaxation time, $1/\tau_{ab}$, is given by the sum of the excited state lifetime τ ($=1/k_f$) and

the absorption cross section σ_{abs} times the excitation power P. Thus, we recorded a series of FCS curves for varying excitation power, from 5 kW/cm^2 to 275 kW/cm^2.

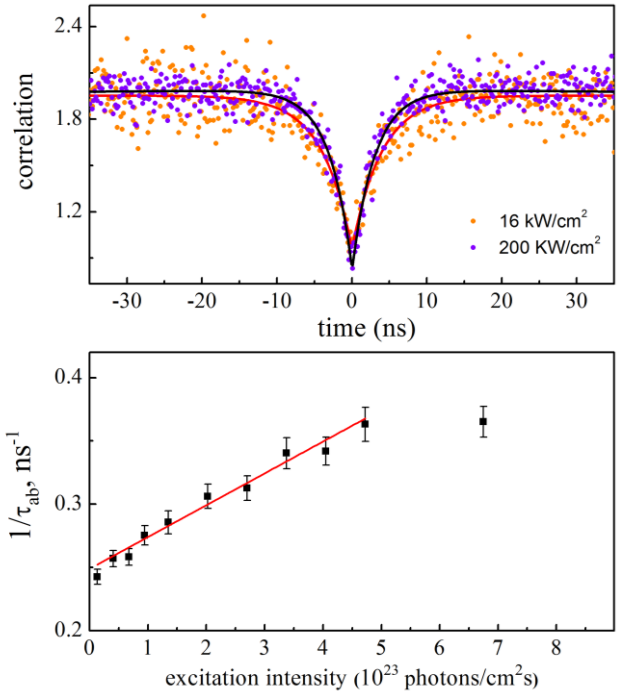

Figure 3.1: Nanosecond correlation at different excitation powers **(top)**. Plot of antibunching relaxation rate as a function of excitation intensity **(bottom)** corresponding data of F(t).

All measurements were performed on aqueous solutions of Rhodamine-110, Rh-110 (F), a common probe for single molecule spectroscopy and imaging. A linear fit of the antibunching relaxation rate $1/\tau_{ab}$ as a function of excitation intensity (excluding the triplet-state induced saturation region at moderately high excitation powers) yields a k_f value of 2.49±0.06 x 10^8 s^{-1}, which corresponds to a lifetime value of τ = 4.0 ns. This lifetime value matches perfectly to the fluorescence decay time of Rh-110 as measured with TCSPC (4.0 ± 0.1 ns), as well as other values reported in the literature. The slope of the linear fit corresponds to an absorption cross section of σ_{abs} = 2.5 ±0.2 x 10^{-16} cm^2, which is also very similar to the value of 2.6 x 10^{-16} cm^2 reported by Ringemann et al.[63] This result demonstrates

the capability of fluorescence antibunching measurements for measuring excitation and de-excitation times on a nanosecond time-scale with high accuracy.

3.3.2 Interactions of Rh110 with aniline

Next, we studied the quenching behavior of Rh-110 fluorescence in the presence of the quencher aniline (Q) in water. For this purpose, we measured the steady-state intensity, and recorded TCSPC fluorescence lifetime curves and antibunching curves, $g_{ab}(\tau|q)$, at various concentration values q of aniline.

First of all, we recorded steady-state absorption spectra and fluorescence intensities as a function of quencher concentration. The steady-state absorption spectra of Rh-110 show merely ~ 1 nm bathochromic shift in presence of a very high aniline concentration of 150 mM, indicating a very weak ground state complex formation (see Figure 3.2).

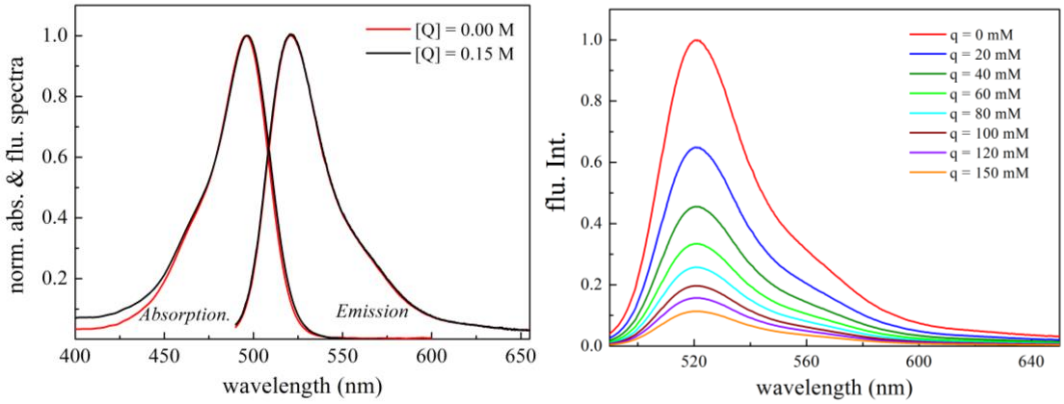

Figure 3.2: Normalized SS absorption and emission spectra of Rh-110 for zero and for 150 mM quencher concentration (left). Fluorescence emission spectra of Rh-110 at different quencher concentrations (right).

The SS fluorescence intensity gradually decreases with increasing quencher concentration, without any change in the spectral shape - indicating fluorescence quenching without exciplex formation.

Next we recorded time resolve TCSPC curves for different quencher concentration as shown in Figure 3.3.

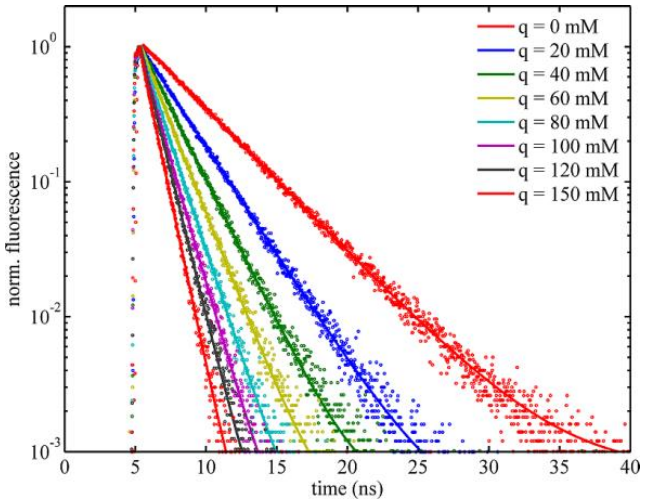

Figure 3.3: Measured TCSPC curves (open circles) at various quencher concentrations, together with mono-exponential fit curves (solid lines).

The recorded TCSPC curves could be perfectly fit with mono-exponential decay curves. This indicates that there is no reverse rate from the F'Q state to F* + Q, which would instantly lead to a multi-exponential decay behavior of the TCSPC curves.

3.3.3 Fluorescence quenching reaction scheme

The assumed fluorescence and quenching kinetics scheme is shown in Figure 3.4, which is based on the ensemble spectroscopy measurements. A fluorescent molecule is excited, with rate k_{ex}, from its singlet ground state (F) to its first excited singlet state (F*). From there, it can either relax to the ground state (with rate k_f), switch into its triplet state T (with intersystem crossing rate k_{isc}), or associated with a quencher molecule to form an encounter complex F'Q (dynamics quenching, rate constant k_{d+}). The encounter complex F'Q dissociates, with rate k_{d-}, into F and Q. Alternatively, the fluorophore can form with the quencher a non-fluorescent

complex FQ (static quenching) while it is in the ground state (rate constant k_{s+}), which then dissociates back into F and Q with rate k_{s-}.

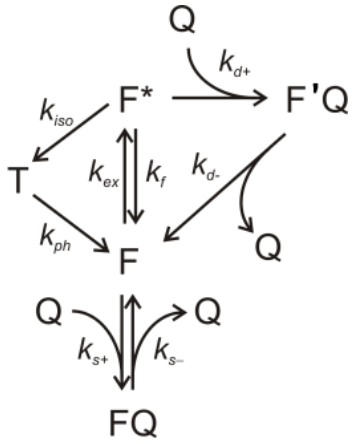

Figure 3.4: Schematic of fluorescence and reaction scheme.

Finally, the relaxation from the triplet state to the ground state is described by the phosphorescence rate k_{ph}. In the above scheme, F'Q and FQ are different as the former is formed via dynamic quenching by collision (i.e. encounter complex formation), while the latter is formed via static quenching by ground state non-fluorescent complex formation and the presence of two different quenching interactions is clearly indicated from Stern-Volmer analysis of ensemble results, as discussed later.

The reaction scheme shown in Figure 3.4 involves 5 states: F, F*, T, F'Q, and FQ. The corresponding reaction rate equations read, in matrix notation,

$$\frac{d}{dt}\begin{pmatrix} \mathrm{F} \\ \mathrm{F}^* \\ \mathrm{T} \\ \mathrm{F'Q} \\ \mathrm{FQ} \end{pmatrix} = \hat{\mathbf{M}}(q) \cdot \begin{pmatrix} \mathrm{F} \\ \mathrm{F}^* \\ \mathrm{T} \\ \mathrm{F'Q} \\ \mathrm{FQ} \end{pmatrix} \tag{3.2}$$

where $\hat{\mathbf{M}}$ is the reaction rate matrix:

$$\hat{\mathbf{M}}(q)=\begin{pmatrix} -k_{ex}-k_{s+}q & k_f & k_{ph} & k_{d-} & k_{s-} \\ k_{ex} & -k_f-k_{isc}-k_{d+}q & 0 & 0 & 0 \\ 0 & k_{isc} & -k_{ph} & 0 & 0 \\ 0 & k_{d+}q & 0 & -k_{d-} & 0 \\ k_{s+}q & 0 & 0 & 0 & -k_{s-} \end{pmatrix} \tag{3.3}$$

which is a function of quencher concentration q. With this reaction scheme, we can obtain all measurable quantities of interest. Firstly, the fluorescence decay follows a simple mono-exponential behavior with fluorescence decay time

$$\tau(q)=\left(k_f+k_{isc}+k_{d+}q\right)^{-1} \tag{3.4}$$

Secondly, from solving the steady sate equation by setting the left hand side in eq. (3.2) to zero, we find that the inverse of the steady state intensity $I(q)$ is a second order polynomial of q given by

$$\frac{I_0}{I(q)}=1+aq+bq^2 \tag{3.5}$$

with coefficients

$$a=\frac{k_{ph}\left[k_{d+}\left(k_{ex}+k_r\right)+k_{d-}\left(k_{s+}/k_{s-}\right)\left(k_f+k_{isc}\right)\right]}{k_{d-}\left[k_{ex}k_{isc}+\left(k_{ex}+k_f+k_{isc}\right)k_{ph}\right]} \tag{3.6}$$

and

$$b=\frac{k_{s+}}{k_{s-}}\cdot\frac{k_{ph}k_{d+}}{k_{ex}k_{isc}+k_{ph}\left(k_{ex}+k_f+k_{isc}\right)} \tag{3.7}$$

This allows us to express the unknown reaction rate constants k_{d-} and k_{s-} through the other constants and the coefficient values a and b as,

$$k_{d-}=\frac{k_{d+}^2k_{ex}k_{ph}}{\left[a\,k_{d+}-b\left(k_f+k_{isc}\right)\right]\left[k_{ex}k_{isc}+\left(k_{ex}+k_f+k_{isc}\right)k_{ph}\right]-k_{d+}^2k_{ph}} \tag{3.8}$$

and

$$k_{s-} = \frac{k_{d+} k_{ph} k_{s+}}{b\left[k_{ex} k_{isc} + k_{ph}\left(k_{ex} + k_f + k_{isc} \right) \right]} \tag{3.9}$$

Finally, the short lag-time part $g_{ab}(t|q)$ of the FCS curve (the antibunching-dominated part, where the impact of diffusion is still negligible) is given by the expression

$$g_{ab}\left(t|q\right) \propto \begin{pmatrix} 0 \\ 1 \\ 0 \\ 0 \\ 0 \end{pmatrix}^{\mathrm{T}} \cdot \exp\left[t\hat{\mathbf{M}}\left(q\right) \right] \cdot \begin{pmatrix} 1 \\ 0 \\ 0 \\ 0 \\ 0 \end{pmatrix} \tag{3.10}$$

which describes the probability to find the molecule back in the excited state at time t when it just relaxed back to the ground state at time zero. Here, the superscript T on the column vector indicates matrix transposition, and the exponent is understood as a matrix exponentiation. This expression for $g_{ab}(t|q)$ cannot be further simplified and has to be computed numerically.

3.3.4 Fitting of Stern Volmer plot

Next, As expected from eq (3.5), the inverse of the recorded steady state fluorescence, $I_0/I(q)$, as a function of quencher concentration can be perfectly fitted with a quadratic polynomial in q (see Figure 3.5), which fixes the values of the constants a and b. Knowing these values, the rate constants k_{d-} and k_{s-} can be calculated if one knows all the other rate constants, see eq. (3.8) and (3.9). Furthermore, the inverse of the fitted fluorescence decay times, τ_0/τ, shows a perfectly linear dependence on quencher concentration q, as expected from eq. (3.4). Fitting this curve with a linear fit (see Figure 3.5), yields a value for the rate constant of excited-dye/quencher complex formation as $k_{d+} = 5.98 \times 10^9\ \mathrm{M^{-1}s^{-1}}$.

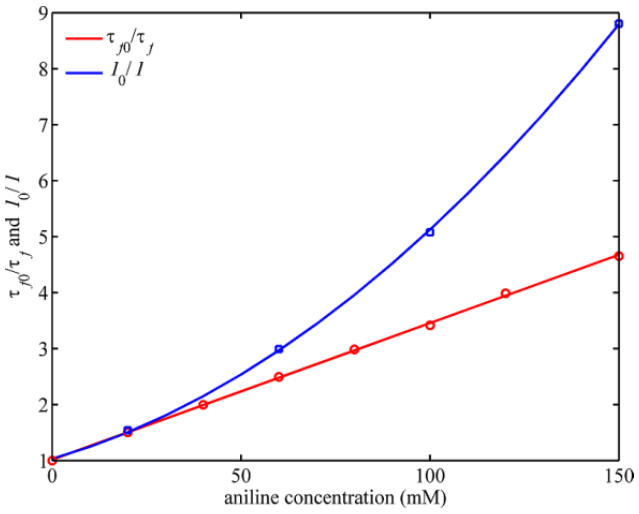

Figure 3.5: Dependence of the inverse fluorescence decay time, τ_{f0}/τ_f (red circle), and inverse of the steady-state fluorescence intensity, I_0/I (blue squares), as a function of quencher concentration q. The inverse lifetime curve is fitted by a linear fit (red line), and the inverse intensity curve is fitted with a quadratic polynomial (blue line).

However, the value of k_{ex}, k_{ph} , k_{isc} and k_{s+} is still unknown, and they cannot be found from TCSPC and steady state intensity measurements alone. Therefore, we used standard FCS for determining values for the intersystem crossing rate k_{isc} and the triplet state de-excitation rate k_{ph} of the fluorophore (Rh110)

3.3.5 Determination of k_{ex}, k_{ph} and k_{isc}

To avoid any nonlinearity effects connected with triplet-state (or higher excited state) pumping, all quenching experiments were performed with moderate excitation powers below 200 kW/cm^2, which is the intensity range where we observed a linear dependence between $1/\tau_{ab}$ and excitation intensity (see Figure 3.1). For this excitation intensity, we used standard FCS for determining values for the intersystem crossing rate k_{isc} and the triplet state de-excitation rate k_{ph}, which occurred to be $k_{isc} = 8.9 \times 10^5$ s^{-1} and $k_{ph} = 2.1 \times 10^5$ s^{-1}, respectively.[63] These values were then used for all subsequent data analysis.

At zero quencher concentration, the fluorescence antibunching relaxation follows a simple mono-exponential behavior (see Figure 3.6), and the relaxation rate is equal to $k_{ex} + k_f + k_{isc}$.

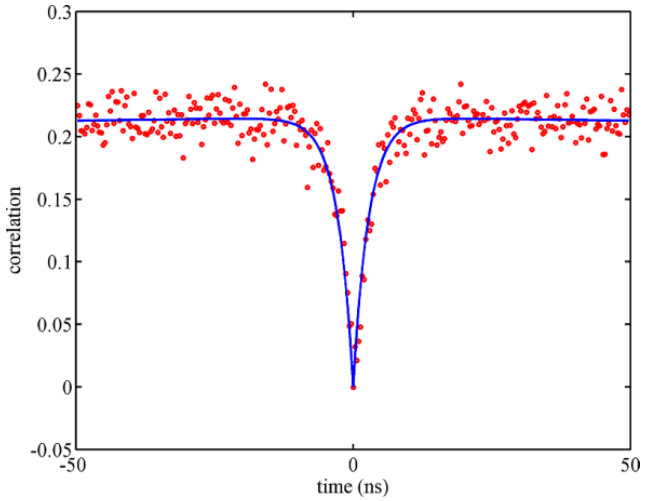

Figure 3.6: Fluorescence antibunching curve of Rh-110 at zero quencher concentration (red circles). The blue line represents a fit with a mono-exponential relaxation function.

Thus, already knowing k_f and k_{isc} we could determine excitation rate for our excitation conditions as $k_{ex} = 3.34 \times 10^8\ s^{-1}$. For all subsequent antibunching measurements, we used identical excitation conditions, so that this excitation rate was the same for all measurements.

3.3.6 Determination of k_{s+} : Variation in Antibunching curves

Next, we recorded antibunching curves of Rh-110 for increasing aniline concentrations (see Figure 3.7). Slop of antibunching curve show gradual variation with varying quencher concentration. The corresponding antibunching relaxation time is calculated and compared with the SV plot obtained from SS and TR TCSPC data. The SV plot from photon anti-bunching data nearly matches the SS SV plot, highlighting the formers ability to represent the full quenching interaction. However, anti-bunching has the edge over conventional SS measurements in extracting the individual rates of complexation kinetics leading to static quenching.

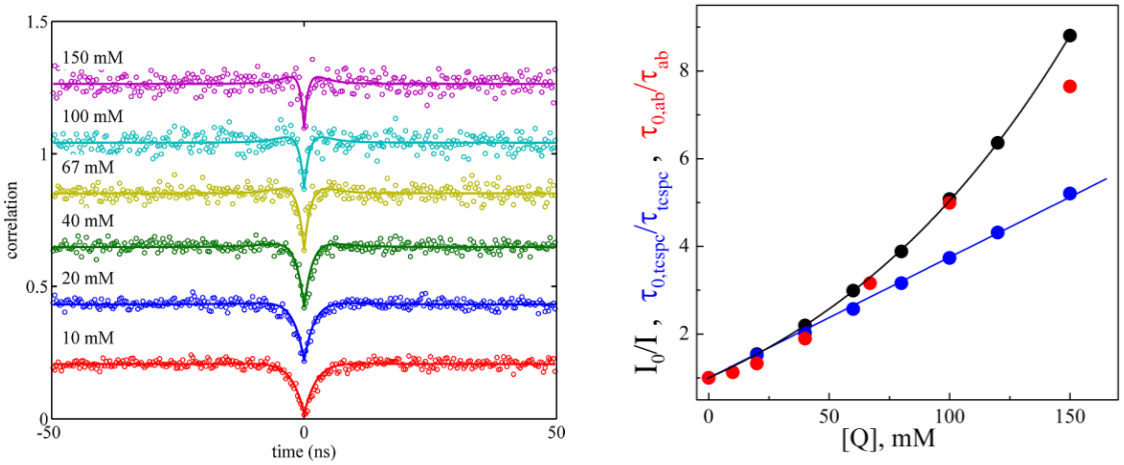

Figure 3.7: Measured antibunching curves (circles) at increasing quencher concentration (left). SV plot form conventional means (SS in black circles and TR in blue circles) and photon antibunching experiments (red circles). Solid lines show a global fit of all curves with the model given by eq. (3.10).

Antibunching curves were globally fitted with the model, eq. (3.10), having only the value of k_{s+}, which is the only left unknown rate constant, as free fit parameter. The model can globally fit all antibunching curves very well (see Figure 3.7). However, it occurs that the static quenching kinetics is by orders of magnitude smaller than the dynamic quenching kinetics, and repeating the fitting yields widely varying values for k_{s+} smaller than $\sim 5 \times 10^5\ M^{-1}s^{-1}$. For such small rate constants, the fit quality of the antibunching curves depends only on the ratio of k_{s+}/k_{s-} which is found to be equal to $29.4\ M^{-1}$, and the value of k_{d-}, which is found to be $k_{d-} = 2.62 \times 10^8\ s^{-1}$.

Thus, we find a very slow static quenching kinetics, which is by 5 orders of magnitudes slower than the dynamic quenching kinetics. However, the equilibrium constants are very similar, $k_{d+}/k_{d-} = 22.8$ and $k_{s+}/k_{s-} = 29.4$. This explains why we see a strongly nonlinear dependence of I_0/I in the steady-state intensity measurements. Antibunching, in principle, can precisely determine the k_{s+} and k_{s-} rates individually, but the slow complexation kinetics of the Rh110/aniline system does not show up on the nanosecond temporal window of antibunching.

3.3.7 Calculation of reaction free energy

In analogy with the fluorescence quenching reported for several Rhodamine derivatives with various amines, we assume that photoinduced electron transfer (PET) is the principal quenching mechanism. The fluorescence quenching by energy transfer from excited Rh-110 to aniline is energetically unfavorable as the emission spectrum of Rh110 does not matches or intersects with the absorption spectrum of aniline which lies even in the higher energy side.

Therefore, the reaction free energy for PET has been estimated using the following Rehm-Weller expression

$$\Delta G^0 = E(D/D^+) - E(A/A^-) - E_{00} - \frac{e^2}{4\pi\varepsilon(R_D + R_A)} \qquad (3.11)$$

where $\boldsymbol{E_{00}}$ is the excited state energy of the Rh110 in the S_1 state, $\boldsymbol{e}$ is the elementary charge, and $\boldsymbol{\varepsilon}$ is the static dielectric constant of the reaction medium, water. The $\boldsymbol{R_D}$ and $\boldsymbol{R_A}$ are hard sphere radii of Rh110 and aniline, respectively. The redox potential of Rh110, $E(A/A^-)$,was measured in water, and the value for aniline, $E(D/D^-)$,was taken from the literature.

$E(A/A^-)$	$E(D/D^+)$	E_{00}, eV	R_A, Å [a]	R_D, Å [a]	ΔG^0, eV
-0.69	0.63	2.5	4.3	2.8	-1.21

[a]: calculated based on Edward's Volume addition method.

Table 3.1: Energetics and ET parameters of Rh110-aniline systems in water.

3.4 Conclusions

Our results demonstrate that photon antibunching is a promising and powerful tool for studying the excited state dynamics of complex systems at the molecular level, and that it is

capable of determining the total ensemble of rates and rate constants, in contrast to TCSPC and/or steady-state measurements alone. It should be emphasized that only the combination of steady-state fluorescence, TCSPC measurements, and antibunching FCS measurements allowed us determine all the essential rates and rate constants which describe the dynamics and static quenching of Rhodamine-110 by aniline, a task which would have been impossible without this combination. Static quenching escapes detection by TCSPC, so that time-resolved Stern-Volmer plots reflect only dynamic quenching.[11,16] Further, our method can also be employed to study reaction rates in viscous media (e.g. organized assemblies, ionic liquids, cellular environment, etc.) where the conventional TCSPC-SV approach for extracting photo-induced reaction rates becomes questionable. Therefore, present results highlight the possibility of exploring complex quenching kinetics in chemical and biological sciences at the molecular level.

CHAPTER 4

Kinetics of Atto655 - Tryptophan Interaction

4.1 Introduction

Earlier we employed photon antibunching to explore dynamic quenching of Rhodamine-110 by aniline on the nanosecond timescale, where contribution of static quenching by ground-state complex formation is very small. Unlike the Rh110-aniline system, most of the pairs of fluorophores (i.e. MR121, Atto-655, TMR, Rh6G, etc.) & quenchers (i.e. tryptophan, tyrosine, guanine, etc.) that have been used for PET FCS exhibit a large amount of static quenching, both by ground-state complex formation as well as quenching-sphere-of-action, besides dynamic quenching.[17,18,21,22,64-67]

Grand efforts have been devoted to explore the intricacies of the interaction mechanism and the kinetics of PET in these systems,[19] even employing ultrafast transient absorption and fluorescence up-conversion measurements,[21,66,67] along with theoretical simulations.[18] But still, a complete picture of all aspects of PET and knowledge of all relevant parameters is still missing. This is partially due to the absence of PET-FCS measurements with sub-nanosecond temporal

resolution, and the lack of a unified model incorporating all relevant quenching mechanisms and coherently describing all available data from single molecule to ensemble measurements.

Moreover, there are inconsistencies between different reported values for the same parameter. For example, the reported quenching sphere radius of > 40 Å for MR121 or Atto-655 and tryptophan, as estimated from a modified SV equation,[19] is much larger than the value estimated from their respective van der Waals radii. As another example, molecular dynamics simulations predict a quenching distance of ~5.5 Å for the MR121-tryptophan system, above which there is no quenching. Moreover, binding stoichiometry, which should have a profound influence on the quenching dynamics, has never been seriously taken into account beyond the presence of a simple ground-state complex formation.[19,21,66,67] Similarly, quenching by weak exciplex formation,[16] which is in principle closely related to quenching-sphere-of-action in highly viscous media, has rarely been thought of as a possible PET mechanism. Thus, the main goal of our work here is to comprehensively disentangle the different mechanisms of PET, and to determine their kinetics.

In this chapter, we will study all the possible PET interactions, i.e. ground-state complex formation, quenching-sphere-of-action, and dynamic quenching of fluorophore (F) Atto-655 (A655) with quencher (Q) tryptophan (Trp) in aqueous medium. For this purpose, we make particular use of fluorescence antibunching, which is not accessible with conventional FCS or with ensemble measurements. Our study also presents a unified and comprehensive model of PET that describes well all the available experimental data.

4.2 Experimental details

4.2.1 Materials

A655 was purchased from Atto-Tech GmbH (Siegen Germany). L-Tryptophan was procured from Sigma (Germany) and was used without further purification. HPLC grade water from Sigma was used for solution preparations. Very dilute solution of freely diffusing A655 in water (~1 nM) has been used for the photon antibunching and conventional FCS measurements. For ensemble spectroscopic investigations, A655 concentration was kept at around 1 μM.

4.2.2 Methods

Ground-state absorption spectra, Steady-state (SS) fluorescence spectra and Nanosecond fluorescence decays were recorded using the similar setup mentioned in Chapter 3. However, here a diode laser (636 nm, <100 ps, 1 MHz) and a special PMT detector (IBH, UK) was used for the fluorescence decay measurements. All the experiments were carried out at ambient temperature, 26±1°C, unless otherwise mentioned.

The similar experimental setup for photon antibunching (and FCS) experiments is used as mentioned in Chapter 3 with 633 nm CW laser as excitation source.

SS and TR quenching measurements along with antibunching measurements were performed in the spectral region of 650-720 nm by suitable selection of emission with a monochromator, cut-off and band pass filters.

4.3 Results and Discussion

4.3.1 Variation in SS fluorescence and absorption spectrum

We recorded steady-state (SS) absorption and fluorescence spectra of A655 as a function of quencher (Trp) concentration (see Figure 4.1) to determine the possible quenching mechanisms.

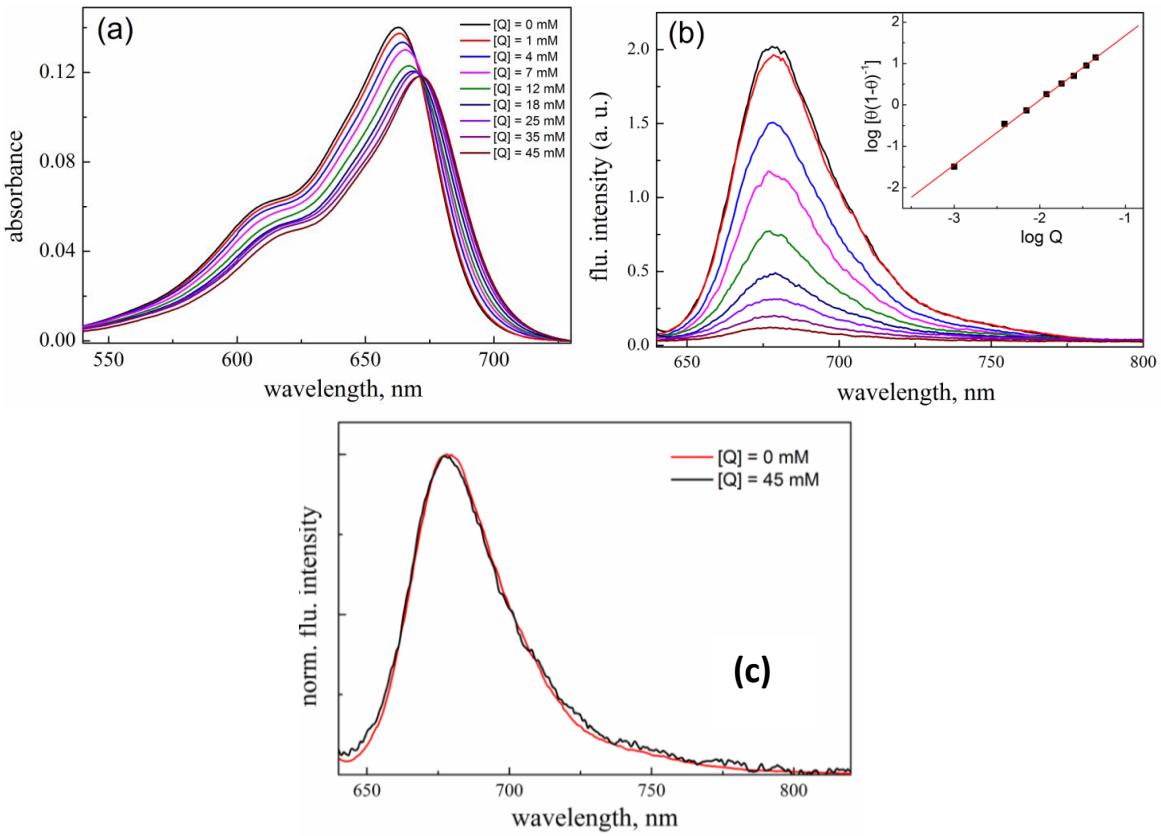

Figure 4.1: Absorption (a) and fluorescence (b) spectra of A655 at various concentrations of Trp. Fluorescence spectra were recorded with 630 nm excitation. Inset in (b) shows the corresponding Hill plot. Normalized emission spectra (c) of A655 in presence and absence of Trp.

With the addition of Trp, the peak absorbance of A655 decreases along with a gradual bathochromic spectral shift of ~ 10 nm (see Figure 4.1a), which is evidence for the formation of a ground-state complex between A655 and Trp. The appearance of an isosbestic point-like feature at 670 nm below a Trp concentration of 10 mM, and then gradual spectral red-shift indicate the possibility of higher-order complex formation (FQ_n; where n is the number of Q's associated per molecule of F), contrary to the usually assumed 1:1 complex (FQ).[21,66,67] Although similar spectral features have been observed in earlier works,[19] no possibility of higher-order complex formation was considered. SS fluorescence studies also show a gradual decrease in fluorescence intensity, I_q (see Figure 4.1b), with increasing Trp concentration, but without any visible change in spectral shape (see Figure 4.1c).

This suggests negligible contribution from exciplex emission. The observed changes in relative fluorescence intensity, $\theta = (I_{q=0} - I_q)/I_{q=0}$, with quencher concentration can be described with a Hill equation

$$\log\left(\frac{\theta}{1-\theta}\right) = n_H \log[Q] + \log K_n \tag{4.1}$$

which allows us to determine the overall binding constant, K_n, and the Hill coefficient, n_H. The corresponding Hill plot (see Figure 4.1b inset) can be best fitted with n_H = 1.6 and log K_n = 3.24. An n_H value of greater than one indicates positive binding cooperativity, meaning that the association of the first quencher molecule with the fluorophore facilitates the association of a subsequent one.[11,68] Taking into account the planar molecular structure of A655, it seems quite feasible that one A655 molecule can interact with two Trp molecules on both its sides in a coplanar stacking conformation. Thus, we consider formation of FQ_2 along with FQ for ground-state complexation, with an estimated overall value of K_n = 1.73 x 10^3 M^{-2}. A determination of the exact stoichiometry by using a Job plot could not be performed because it is impossible to reach, in aqueous solution, the required very high concentrations of A655 (generally much larger than K_n).[69] The nonlinear regression fitting of intensity following successive 1:2 complexation, as reported by Nigam et al.,[70] we obtain overall complexation constant of 8.1x10^3 M^{-2}, which is of similar order estimated from Hill plot.

Fluorescence quenching through excited state complex formation (besides dynamic collisional quenching) can also lead to additional quenching.[16,22,71] To check this possibility, we recorded excitation spectra as a function of Trp concentration, as shown in Figure 4.2.

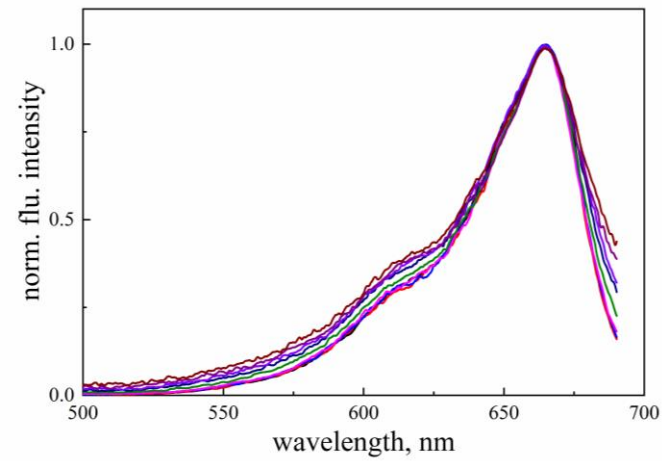

Figure 4.2: Excitation spectra of A655 at various concentrations of Trp for fixed emission at 700 nm.

Changes in excitation spectra upon the addition of Trp unambiguously indicate an excited state interaction, probably exciplex formation, at high quencher concentration. However, the excited fluorophore & quencher complex must be only weakly or not emissive, because emission spectra remain almost unaltered in the absence and presence of Trp (see Figure 4.1c). In the quenching-sphere-of-action model, quenching happens without the diffusion of nearby quencher molecules, and can be approximately considered to be similar to quenching via weak excited-state complex formation within the reaction sphere. For simplicity, in our kinetic scheme we define this additional fast quenching by a single overall rate constant, k_p. Formation of dye dimers or aggregates is neglected, because they are reported to form only much above the studied concentration range of ≤ 1 μM.[70,71] The absence of any appreciable change in fluorescence lifetime and spectra of A655 over the studied concentration range further substantiates this assumption (see Figure 4.3b).

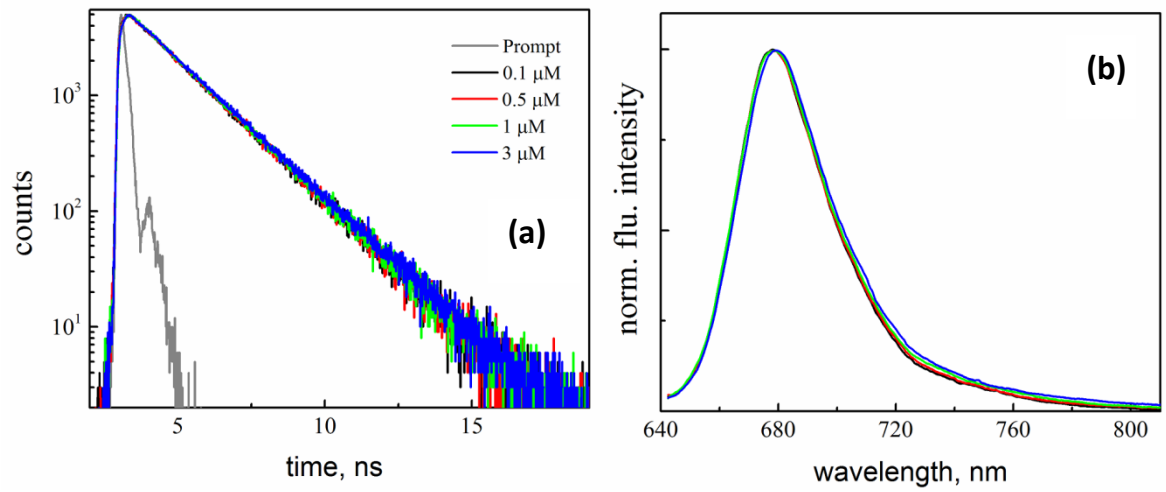

Figure 4.3: Fluorescence decay at 680 nm (a) and fluorescence spectra (b) for A655 at concentrations of ≤ 1 µM indicate negligible influence of dye aggregates.

4.3.2 Variation in TR fluorescence or TCSPC curves

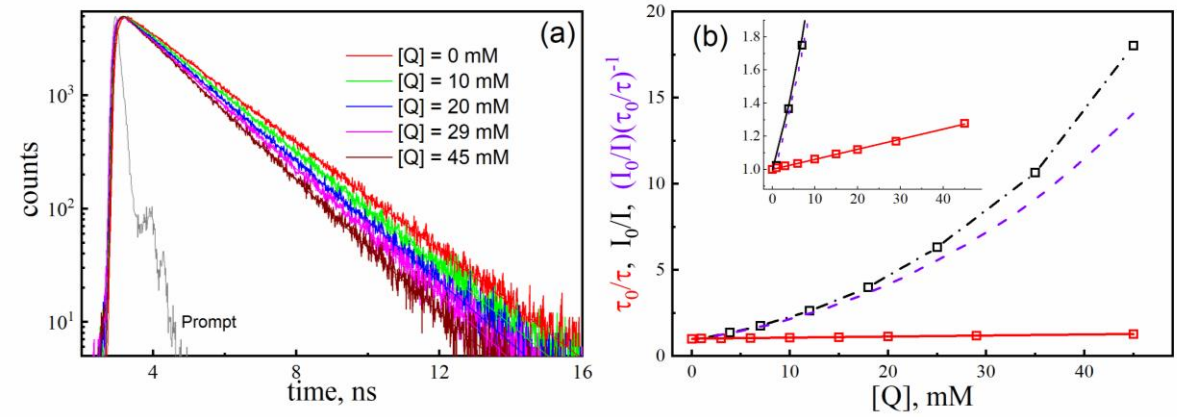

Figure 4.4: Fluorescence decays of A655 at different concentrations of Trp **(a)**. SV plot obtained from SS (black) and TR (red) measurements **(b)**. Here the solid red line represents the linear fit for TR SV data. The violet dashed line represents the ratio of SS and TR SV data indicating higher order complexation in ground state. The inset in (b) is the zoom in graph for the similar SV plot indicating huge variations in the SS intensity as compare to the variation in fluorescence lifetime i.e. the predominant interactions are in the ground state of fluorophore.

Next, we recorded fluorescence decays with time correlated single photon counting (TCSPC), which revealed a linear dependence of the decay time with Trp concentration (see Figure 4.4a). All recorded fluorescence decays could be well fitted with a mono-exponential decay

function, without any negative decay component that would signify exciplex equilibrium. However, the appearance of a small contribution with very short decay time is observed at very high Trp concentrations.[17] Examination of the excited state lifetime values (τ) show that they follow a SV relation, i.e. $\tau_{q=0}/\tau_q$ vs. [Q] displays a linear correlation, as expected for dynamic quenching (see Figure 4.4b).[11,16] It should be noted that strong exciplex-mediated quenching generally results in a non-linear negative deviation from the linear SV plot[72,73] and that this deviation should increase with increasing temperature.[73] However, we observe a strict linearity of the SV plots over the studied temperature range from 298 K to 328 K, with increasing linear slope for increasing temperatures (see Figure 4.5). Hence, we conclude that exciplex-mediated quenching is negligible or even absent in the studied system.

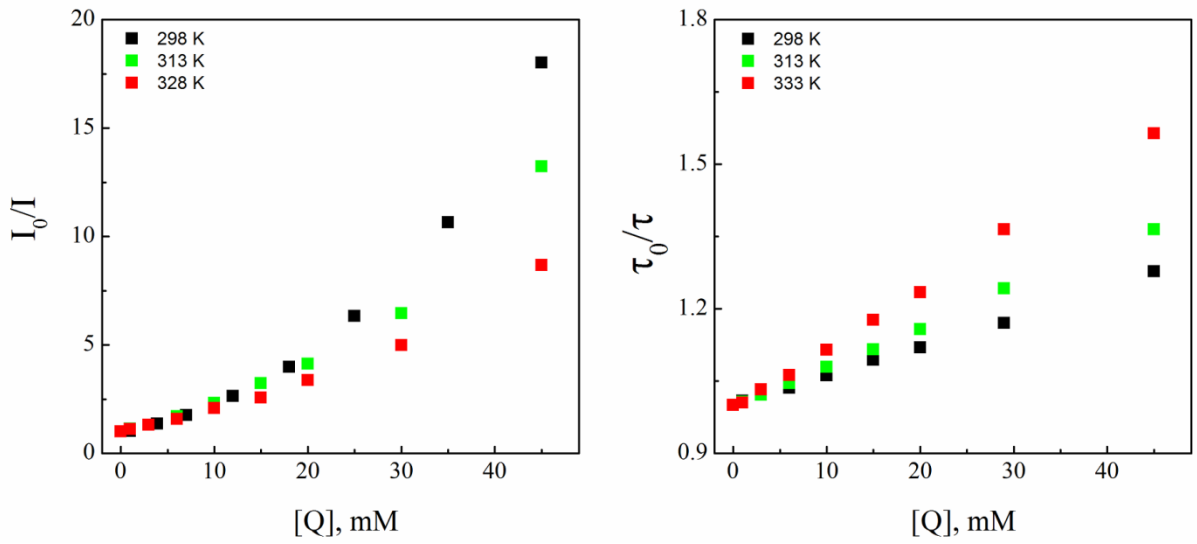

Figure 4.5: SS (left) and TR (right) SV plots measured at different temperatures. Increase in temperature shows a reduction in positive deviation (lowering of static quenching, SS SV plot) but an increase in dynamic quenching (TR SV plot).

Next, contrary to TR results, the corresponding SS fluorescence intensity data ($I_{q=0}/I_q$ vs. [Q]) shows a positive deviation from linearity (see Figure 4.4b), indicating the presence of static quenching along with dynamic quenching.[11,16] However, static quenching is the dominant process for the interaction between A655 and Trp, as clearly evident from the comparison of SS and TR SV plots.[18] The non-linear positive deviation of the static-only quenching seen in the

relation of $(I_{q=0}/I_q)(\tau_{q=0}/\tau_q)^{-1}$ vs. [Q][19,74] highlights the complexity of the interaction (see Figure 4.4b). This could be due to either higher-order complex formation, or to instantaneous excited-state quenching at high [Q] values, or both of them. Absence of a clear single isosbestic point in the absorbance data and analysis of the Hill plot undeniably suggests higher order complex formation, while changes in the excitation spectra reflect excited-state interactions other than dynamic quenching.

4.3.3 Proposed reaction scheme

With this background of possible quenching interactions, the proposed kinetic fluorescence and quenching scheme for the pair A655-Trp is shown in Figure 4.6.

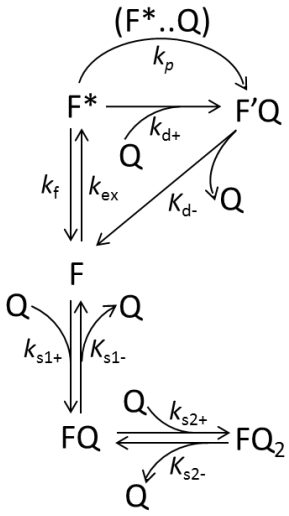

Figure 4.6: Schematic of fluorescence and reaction scheme.

Here, F denotes the fluorophore in its ground state which is excited, with rate k_{ex}, into its first excited singlet state (F*). This excited state can either relax directly to the ground state (with rate k_f) or collide with a quencher molecule Q (i.e. dynamic quenching) to form a charge transfer product F'Q with rate constant k_{d+}. This complex eventually cycles back to ground state

F, with rate k_{d-}. The additional fast quenching of the excited state via exciplex formation or quenching-sphere-of-action is incorporated in the scheme via the (F*..Q), which accounts for non-zero probability of the interaction of an excited fluorophore with a quencher in close vicinity during excitation, which leads to a tunneling-like quenching dynamics on a picosecond time range and will thus not be visible in the measured fluorescence decay curves or antibunching data. The primary charge transfer products of the quenching-sphere-of-action or exciplex formation processes are assumed to be similar to those of dynamic quenching, except that in the first case their formation is instantaneous with respect to excitation, and that quenchers hardly diffuse during quenching interaction. Stepwise formation of non-fluorescent ground-state complexes FQ and FQ_2 for static quenching is described by the association and dissociation rate constants, k_{s1+} & k_{s1-}, and k_{s2+} & k_{s2-}, respectively.

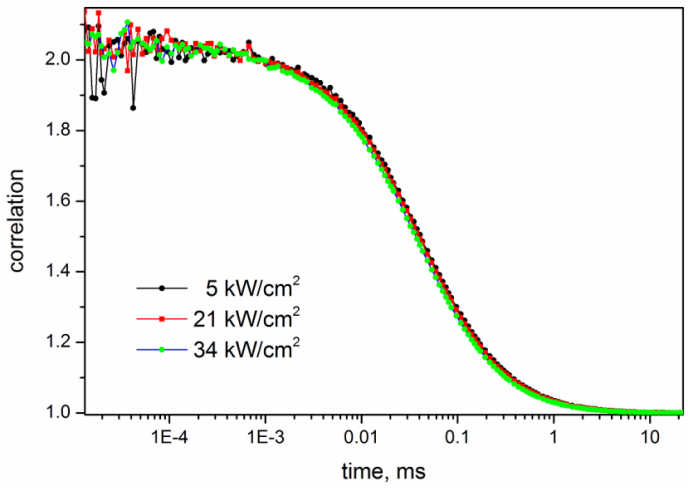

Figure 4.7: FCS curves of A655 in water at different excitation intensities indicate negligible contribution of triplet state photophysics.

Any intersystem crossing to the triplet state for A655 is assumed to be absent for the used excitation power of 34 kW/cm^2 in the present study, taking into account that it is negligible

even at higher excitation intensity of 100 kW/cm^2.[64,75] Excitation-intensity dependent FCS curves for A655 are shown in Figure 4.7.

The reaction scheme shown in Figure 4.6 involves five states: F, F*, F'Q, FQ and FQ_2. The corresponding reaction rate equations can be written in matrix notation as

$$\frac{d}{dt}\begin{pmatrix} \mathrm{F} \\ \mathrm{F}^* \\ \mathrm{F'Q} \\ \mathrm{FQ} \\ \mathrm{FQ_2} \end{pmatrix} = \hat{\mathbf{M}}(q)\cdot\begin{pmatrix} \mathrm{F} \\ \mathrm{F}^* \\ \mathrm{F'Q} \\ \mathrm{FQ} \\ \mathrm{FQ_2} \end{pmatrix} \tag{4.2}$$

$\hat{\mathbf{M}}$ is the reaction rate matrix:

$$\hat{\mathbf{M}}(q) = \begin{pmatrix} -k_{ex} - k_{s1+}q & k_f & k_{d-} & k_{s1-} & 0 \\ k_{ex} & -k_f - k_{d+}q & 0 & 0 & 0 \\ 0 & k_{d+}q & -k_{d-} & 0 & 0 \\ k_{s1+}q & 0 & 0 & -k_{s1-} - k_{s2+}q & k_{s2-} \\ 0 & 0 & 0 & k_{s2+}q & -k_{s2-} \end{pmatrix} \tag{4.3}$$

which is a function of quencher concentration $\boldsymbol{q}$, and where we have left out $\boldsymbol{k_p}$ because (i) sphere-of action quenching is much faster than the time range accessible by time-resolved fluorescence or antibunching measurements, and (ii) it leads to a non-polynomial dependence of the static quenching curve on quencher concentration, which cannot be described as simple linear reaction kinetics. With this reaction scheme, we can determine all quantities of interest. Firstly, the fluorescence decay follows a simple mono-exponential behavior with fluorescence decay time

$$\tau(q) = \left(k_f + k_{d+}q\right)^{-1} \tag{4.4}$$

Secondly, from solving the steady sate equation by setting the left hand side in Eq.(3) to zero, we find that the inverse of the steady state intensity $I(q)$ is a third order polynomial of q.

However, this polynomial has to be multiplied by an additional exponential term exp(qV) which takes into account the sphere-of-action quenching, where V is the quenching sphere volume (per mole). So that one finds

$$\frac{I_0}{I(q)} = \left(1 + aq + bq^2 + cq^3\right)\mathrm{e}^{qV} \tag{4.5}$$

with coefficients

$$a = \frac{k_{s1-}\left(k_{ex} + k_{d-}\right)k_{d+} + k_{d-}k_f k_{s1+}}{k_{d-}k_{s1-}\left(k_{ex} + k_f\right)} \tag{4.6}$$

$$b = \frac{k_{d+}k_{s2-}k_{s1+} + k_f k_{s1+}k_{s2+}}{\left(k_{ex} + k_f\right)k_{s1-}k_{s2-}} \tag{4.7}$$

and

$$c = \frac{k_{s1+}k_{s2+}k_{d+}}{\left(k_{ex} + k_f\right)k_{s1-}k_{s2-}} \tag{4.8}$$

Finally, the short lag-time part $\boldsymbol{g_{ab}(t|q)}$ of the FCS curve (the antibunching-dominated part, where the impact of diffusion is negligible) is given by the expression

$$g_{ab}(t|q) \propto \begin{pmatrix} 0 \\ 1 \\ 0 \\ 0 \\ 0 \end{pmatrix}^{\mathrm{T}} \cdot \exp\left[t\hat{\mathbf{M}}(q)\right] \cdot \begin{pmatrix} 1 \\ 0 \\ 0 \\ 0 \\ 0 \end{pmatrix} \tag{4.9}$$

which describes the probability to find the molecule back in the excited state at time t when it just relaxed back to the ground state at time zero. Here, the superscript T on the column vector indicates matrix transposition, and the exponent is understood as a matrix exponentiation. This expression for $\boldsymbol{g_{ab}(t|q)}$ cannot be further simplified and has to be computed numerically.

4.3.4 Global fitting of SS, TR and antibunching curves

Having this model in place, we first fitted the TR SV plot using eq. (4.4), thus finding k_{d+} = 3.34×10^9 M^{-1}s^{-1} and k_f = 5.46×10^8 M^{-1}s^{-1} (the latter corresponding to a fluorescence decay time of τ_f = 1.83 ns). Lettings these values fixed, in a second step, we fitted both the SS SV *and* all the antibunching data globally with one set of kinetic rate constants $k_{ex}, k_{s1+}, k_{s1-}, k_{s2+}, k_{s2-}$ and the sphere-of-action volume *V*. During the fit, we put the back-reaction rate constant k_{d-} equal to k_{s1-}, because the electron transfer in the complex F'Q is quasi instantaneous leading to FQ so that the dissociation rate constants k_{d-} and k_{s1-} describe the same process FQ → F + Q. The global fit result for the SS Stern Volmer and the antibunching curves is shown in Figure 4.8.

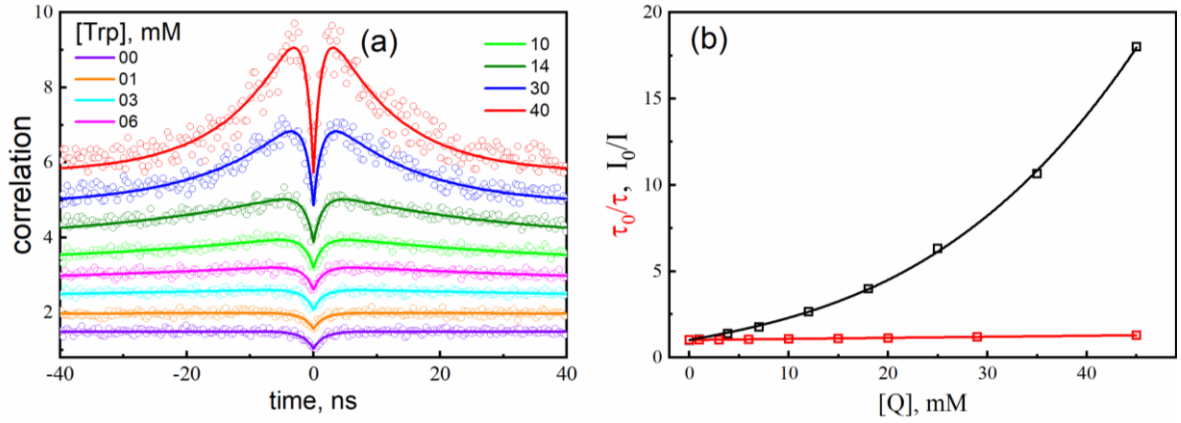

Figure 4.8: Measured antibunching curves (a) for increasing quencher concentration (indicated on top). SS and TR Stern Volmer plot (b). Solid lines in (a) and (b) represents global fitting according to unified reaction scheme.

The found values for the rate constants are k_{ex} = 1.3×10^8 s^{-1}, k_{s1+} = 3.1×10^9 M^{-1}s^{-1}, k_{s1-} = 4.4×10^7 s^{-1}, k_{s2+} = 9.1×10^9 M^{-1}s^{-1}, k_{s2-} = 3.1×10^8 s^{-1}, and for the sphere-of-action volume per molecule = 2.5×10^{-23} l which corresponds to a sphere-of-action radius of 1.8 nm. The calculated overall association constant of 2.7×10^8 M^{-1} from these global fit constants matches nicely with the earlier estimated values from steady state ensemble data (Hill plot). Besides, the present

global estimation of quenching sphere radius is much closer to the van der Waals contact distance between fluorophore and quencher, than any of the earlier estimates. Our estimate is also in agreement with the established quenching sphere radius which is slightly larger than the van der Waals contact distance between F and Q.[16]

To further substantiate the validity of the proposed kinetic scheme, we analyzed the antibunching data with a model assuming only a 1:1 or 1:2 ground-state complexation. However, both fail to globally fit the experimental data set with acceptable rate constants (Appendix A1). This further corroborates the complex kinetic scheme for A655-Trp system, as shown in Figure 4.6.

It should be emphasized here that, until now, we attributed the observed excited state interactions (as seen by the changes in the excitation spectra in the presence of a quencher) either to exciplex formation or to sphere-of-quenching interaction. However, due to the absence of any appreciable exciplex emission and no tangible evidence for a negative deviation in the TR SV plot along with its reverse temperature effect, quenching due to exciplex formation cannot be proven with certainty. Nonetheless, instantaneous quenching of excited A655 molecules by weakly interacting Trp molecules, as described by the quenching sphere model, seems quite plausible.

4.4 Conclusion

In this fundamental photo-physical study of commonly used dye-quencher system (i.e. MR121/A655-Trp) we have highlighted cooperative binding and its quantitative analysis for quenching kinetics – hitherto unaccounted in conventional FCS analysis. Besides, quenching interaction by sphere-of-action has also been for the first time incorporated in the analysis of PET-FCS, which lead to the better description of quenching sphere. This is in complete contrast

to earlier reports with conventional FCS results and analysis. And the most intriguing and novel aspect of the present work is that we coherently describe a unified and comprehensive mechanistic and kinetic model for fluorescence quenching of MR121/Atto-655 by tryptophan, which excellently describes all available data from single molecule to ensemble measurements with a single set of global parameters – which is also a first in the field of quenching kinetics in general. Moreover, the advantage of presented nanosecond FCS or photon antibunching over conventional FCS is its ability to directly measure kinetic rates, and the possibility of exploring both static and dynamic interactions. Most importantly present study demonstrates that FCS measurements have a lot to offer provided we frame an appropriate scheme with precise inputs from other spectroscopic tools.

CHAPTER 5

Kinetics of Calcein - Metal Ion Interaction

5.1 Introduction

Fluorescence Correlation Spectroscopy (FCS) has been extensively used to measure equilibrium binding constants (*K*) or association and dissociation rates in many reversible chemical reactions across chemistry and biology. For the majority of investigated reactions, the binding constant was on the order of ~100 M^{-1}, with dissociation constants faster or equal to 10^3 s^{-1}, which ensured that enough association/dissociation events occur during the typical diffusion-determined transition time of molecules through the FCS detection volume. This is also evident from our previous studies with Rh110-aniline and A655-tryptophan systems as well.

In general, the autocorrelation curve for freely diffusing molecules undergoing fast reversible blinking transitions between a fluorescent & non-fluorescent state (e.g. singlet-triplet transition) is given by[76,77]

$$G(\tau) = G(\infty) + \frac{1}{N(1-T)} \cdot \frac{1}{1+\tau/\tau_D} \cdot \frac{\left(1-T+T\cdot e^{-\tau/\tau_T}\right)}{\sqrt{1+\left(r_0/z_0\right)^2 \cdot (\tau/\tau_D)}} \qquad (5.1)$$

The relation between the diffusion time τ_D and diffusion constant D of the fluorophore is given by $\tau_D = 2r_0^2/D$, which allows for determining D if r_0 is known. The above model can be easily generalized for the case of more than one species. For example, in the case of two species with different diffusion coefficients $D1$ and $D2$, the resulting correlation curve is a simple additive superposition of eq. (5.1) with the two diffusion times τ_{D1} and τ_{D2}. This can be, for example, exploited for studying the binding equilibrium between a small ligand (fast diffusion time) and its bound state to a larger target (slow diffusion time). Then the ratio of the amplitudes of the two contributions of the kind eq. (5.1) to the total correlation curve reflects the ratio between free and bound ligand concentration.[37,39,40,78-80]

A detail account of using FCS for the measurement of association constants (K_a) & binding kinetics has been given by Al-Soufi et al.[37] In all these investigations, one uses the fact that binding leads to a significant change in diffusion time. However, this is no longer the case for the binding of small metal ions (M) to a chelating ligand/fluorophore (L), where the resulting change in hydrodynamic radius is negligible. However, such a binding can lead to a tremendous change in the fluorescence brightness of the ligand due to metal-induced fluorescence quenching or enhancement.[81-83] This again leads to fluorescence intensity fluctuations exploitable by FCS. Thus, performing and evaluating FCS measurements at different concentrations of metal ions and ligands allows for measuring binding curves and determining association constants (K_a). In particular, for a reaction of the form[81]

$$M + L \underset{k_b}{\overset{k_f}{\rightleftharpoons}} ML$$

where, on the left-hand side, the ligand is fully fluorescent, and, on the right-hand side, its fluorescence is quenched, one will observe a correlation curve very similar to eq. (5.1), but

where τ_T is now replaced by a corresponding relaxation time τ_R, and the dark-state related amplitude T by a reaction-related amplitude A_R.[37-39] Under pseudo uni-molecular conditions ([M] >> [L]), the relaxation time is given by $\tau_R^{-1} = k_f$ [M] + k_b, and the amplitude by $A_R = k_f$ [M]/k_b, thus providing valuable information about the reaction kinetics.[37] This approach was used by Magzoub et al.[84] for measuring the millisecond association kinetics of potassium ions with triazacryptand-based indicator ligands. They found association rate constant k_f of 2×10^3 $M^{-1}s^{-1}$ and a dissociation rate constant k_b of 1.2×10^2 s^{-1}, for a fixed association constant $K_a = k_f/k_b$ of 16.7 M^{-1}. For the smallest K^+-concentration studied (20 mM), the relaxation time τ_R was around 6.2 ms, comparable to the diffusion time of the free ligand (~0.5 ms).

Extrapolating these results to sub-micromolar metal concentrations (as would be desirable for actinides) indicates that τ_R becomes close to k_b^{-1}, as k_f·[M] tends to zero. metal ion complexes with chelating ligands form thermodynamically stable complexes with dissociation rates equal or smaller than 10^{-2} s^{-1},[85-87] which makes the relaxation time τ_R significantly larger than the diffusion time τ_D. As a result, the correlation decay related to the chemical reaction will be barely detectible in a FCS autocorrelation curve, because this will be decayed to zero (due to diffusion) before the correlation decay associated with the chemical reaction can set in. Thus, FCS seems to be incapable of measuring association rates (at low ion concentrations) for values of $K > 10^4$ M^{-1}. This is, however, the case for the majority of interactions involving metal ions with charged chelating ligands. For such systems with large values of K_a ($\tau_R >> \tau_D$), the typical approach is to measure the relaxation rate for varying reactant concentrations close to the pseudo uni-molecular regime, and then to estimate the values of k_f and k_b from the slope and intercept of a linear plot of the relaxation rate against analyte concentration. Using this approach, Göhler et al.[88] determined the association and dissociation rate constants for human adhesion/growth-

regulatory galectins and found their values to be on the order of $10^3\ M^{-1}s^{-1}$ and $10^{-4}\ s^{-1}$, respectively (i.e. $K_a \cong 10^7\ M^{-1}$). This indirect approach to assess the kinetic parameters[88,89] is promising for tackling the present problem of measuring metal-ligand complexation at ultra-small amounts of metal ions.

In the present chapter, we explore the applicability of FCS for measuring reaction rates of such complexation reactions, and apply it to binding of iron, europium and Uranyl ions to a fluorescent chelating ligand, calcein. For this purpose we exploit the fact that the ligand fluorescence becomes strongly quenched after binding a metal ion, which results in strong intensity fluctuations that lead to a partial correlation decay in FCS. We further demonstrate the power of FCS in studying the complexation of the highly radioactive ions $^{241}Am^{3+}$, where its use leads to an unprecedented minimization of required sample amount, reducing sample radioactivity by around 6 orders of magnitude (as compared to conventional bulk spectroscopy). In particular, the tiny observation volume of FCS of ~ 1 fL together with its inherent requirement of very low sample concentration allows us to perform experiments with only 1 μl sample solution at an Am^{3+} concentration of ~ 10^{-9} M, which amounts to a radioactivity level of less than 1 Bq.

5.2 Experimental Details

5.2.1 Materials

Calcein dye, Mohr salt ($(NH_4)_2Fe(SO_4)_2 \cdot 6H_2O$), europium nitrate, and DFO (Deferoxamine) were purchased from Sigma-Aldrich and was used without further purification. Highly purified laboratory stock of uranyl nitrate was used for complexation study. DOTA was a gift from Dr. Tapas Das, RPhD, BARC. Imidazole (extra pure-AR grade) from SRL and concentrated HCl (AR grade) from Thomas Baker was used for preparation of 200 mM buffer

stock. The stock was suitably diluted to prepare 10 mM Imidazole-HCl buffer of pH 6.5 (± 0.05) for all spectroscopic measurements in the present study. HPLC grade water from Sigma was used for solution preparations without any treatment with Chelex. Very dilute solution of freely diffusing calcein in buffer solution has been used for the photon antibunching and FCS measurements. All solutions were prepared at least 6 hours before measurements to reach equilibrium, unless specifically mentioned.

In solution iron(II) is highly unstable and quickly oxidizes to iron(III). Calcein shows binding to both iron(II) and iron(III) states. The strong affinity of DFO for iron(III) facilitates auto oxidation of iron(II) and competes rapidly with calcein for iron.[90]

Am-241 stock solution was prepared by dissolving Americium oxide powder (purity >99%) in minimum volume of nitric acid. This stock solution was diluted appropriately as per our requirement in FCS experiments. Laboratory stock solution of freshly purified ^{241}Am was used for the experiments and the purity of the ^{241}Am was checked using alpha spectrometry (silicon surface barrier detector) and gamma spectrometry (HPGe detector). The concentration of ^{241}Am (~ micromolar) in the stock solution was estimated based on its activity (in Bq) measured in liquid scintillation counting system and this stock solution was appropriately diluted to nanomolar concentration range using buffer as per our requirements.

5.2.2 Methods

Ground-state absorption spectra, Steady-state (SS) fluorescence spectra and nanosecond fluorescence decay were recorded using similar setups mentioned (used) in Chapter 3 and 4. pH meter from Eutech Instruments (model PC2700) was used for pH measurements.

The experimental setup for FCS measurements are same, as mentioned in chapter 3 & 4. 488nm CW laser is used for the excitation of Calcein in FCS experiments. FCS measurements for complexation with iron and uranium were performed on aqueous solutions of calcein (L) in Lab-Tek chambers. For measurements with americium we used 1 µL solution in between two no. 1 thickness coverslips separated by suitable spacer of 150 micron height, as shown in Figure 5.1. Positioning the pan-cake shaped solution in the center of the observation volume was achieved by precisely monitoring reflection signal (in Zeiss-ZEN software) from the top surface of the bottom coverslip and the bottom surface of the top coverslip by the motorized Z-drive of Axio-observer-Z1. We then place the objective at nearly half distance from these two surfaces. A short FCS trace recorded with 1 µl solution in this arrangement is similar to that with a regular drop of solution (50 µl), also shown in Figure 5.1.

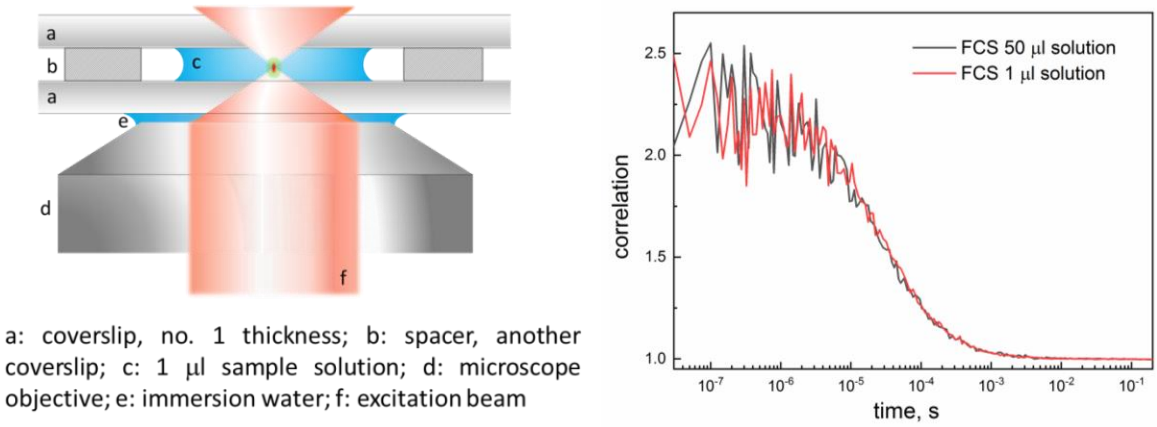

Figure 5.1: (**Left**) Representative cover slip arrangement for FCS measurement with 1 µl solution (not to scale). Red spot in sample indicates confocal volume. (**Right**) FCS curves of Rh110 recorded for 60 seconds in a droplet of 50 µl solutions over coverslip (red) and 1 µl solution sandwiched between two coverslips.

There was no appreciable change in correlation amplitude even up to half an hour of sample loading in between two cover slips, expected in case of solvent evaporation. However to rule out any significant effect on FCS traces, complexation study with 1 μL solutions were performed with higher laser power of ~10% (~60 mW) and acquisition time of less than 15 minutes.

FCS data analysis: Fluorescence fluctuations arising from single molecules diffusing through the detection volume in fluorescence correlation spectroscopy (FCS) experiments were analyzed via second order cross correlation function, *G(t)* (eq. 5.1). Data were fitted to an analytical model using containing a single 3-dimensional diffusion term with a single-exponential triplet relaxation.[91]

Calibration of our FCS setup was performed with standard solution of Rh110 in 8-well Lab-Tek chambers, shown in Figure 5.2. The diffusion coefficient (D) of Rh110 corresponding to diffusion time of 36.3 μs in the present setup is 4.7 x 10^{-6} cm^2s^{-1}.

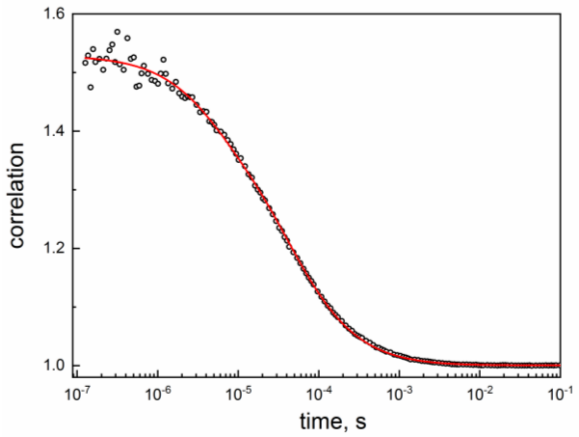

Figure 5.2: FCS curve of ~ 3 nM Rhodamine-110 dye in water. Solid line is the fitting curve following equation 5.1. The estimated confocal volume is 0.98 fL with r_0/z_0 = 0.1 and r_0 = 0.26 μm.

In photon antibunching curves (in nanosecond region) influence of triplet state dynamics (~2 μs) is expected to be negligible. Hence a simple fit with below form for the nanosecond range is used to extract antibunching relaxation time constant (t_{ab}) and its amplitudes (A).[49]

$$G_{ab}(\tau) = G(\infty) + A\left(1 - e^{-\tau/\tau_{ab}}\right) \tag{5.2}$$

The observed antibunching relaxation time of 2.83 ns for calcein remain nearly constant in presence of metal ions, but its amplitude increases due to decrease in calcein ground state population. Normalized FCS curves in absence and presence of metal ions indicate unaltered triplet state dynamics and its contribution (e.g. Figure 5.7(b) inset). Therefore the variation in A is exclusively due to the change in calcein singlet state population only and related to change in *N* value.

Determination of binding constant was carried out by calculating normalized change in amplitude (FCS & photon antibunching) and SSF intensity following equation 5.3[23] and its correlation with added metal ion concentration.

$$Y = \frac{\Delta x_i}{\Delta X} = \frac{x_0 - x_i}{x_0 - x_\infty} = \frac{K[M]^n}{1 + K[M]^n} \tag{5.3}$$

where x_0 is the initial fluorescence intensity or average number of molecule in confocal volume in absence of metal ions, x_i is the fluorescence intensity or average number of molecule in presence of metal ions, x_μ is the saturating fluorescence intensity or average number of molecule in confocal volume at very high metal ion concentrations, K is the binding constant, [M] is the quencher concentration (which is metal ion concentration) and n is the stoichiometry.

In order to estimate forward (i.e association) rate, k_f and backward (i.e. dissociation) rate, k_b we recorded change in fluorescence intensity as function of time after the addition of metal ion into calcein solution. The plots for the time dependent intensity decay were fitted with equation 5.4, as

$$\left(I - I_f\right)/\left(I_0 - I_f\right) = e^{-(Kk_b[M]^n + k_b)t} \tag{5.4}$$

where, I_0 is the initial fluorescence intensity, I_f is the fluorescence intensity at a very long time (i.e. saturating fluorescence intensity) and , I is the intensity at any given time.

5.3 Results and discussion

In the present study, we used calcein (L) as chelating ligand. Calcein is a well-known turn-on sensor for calcium ions in solution at pH > 10.[92]

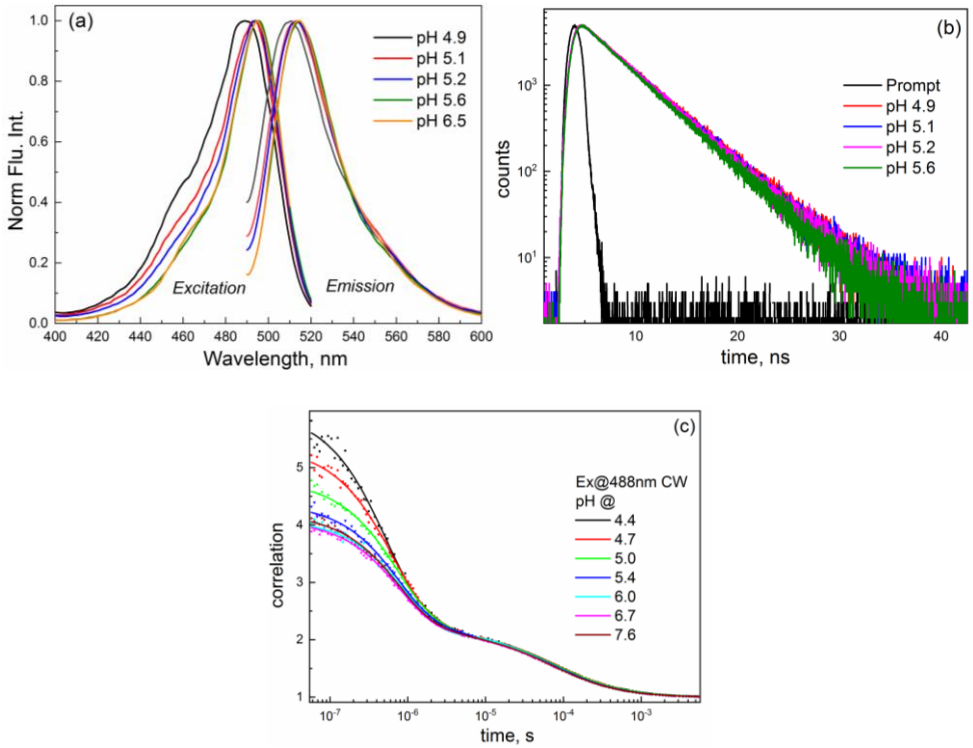

Figure 5.3: Normalized excitation and emission spectra **(a)**, time resolve spectra **(b)** and FCS curves **(c)** of calcein in water at different pH.

Below pH 10, calcein shows bright fluorescence, and binds also to various other metals (henceforth termed as M) such as Fe, Ni, Cu, etc. Because the photophysics of calcein (excitation & emission spectra, quantum yield, intersystem crossing yield) is very sensitive to the pH of the solvent (see Figure 5.3), we used a 10 mM imidazole-HCl buffer of pH 6.5 ± 0.05 for all our measurements.

This choice of pH was motivated by the fact that the fluorescence quantum yield of calcein decreases significantly at very small values or very large values of pH. We checked also that any background signal from blank buffer was negligible compared to calcein fluorescence (see Figure 5.4a). Any presence of trace metal impurities in the buffer was not expected to impair our results, as we correlate only the change in fluorescence of L upon addition of M (keeping the concentrations of L and buffer constituents fixed).

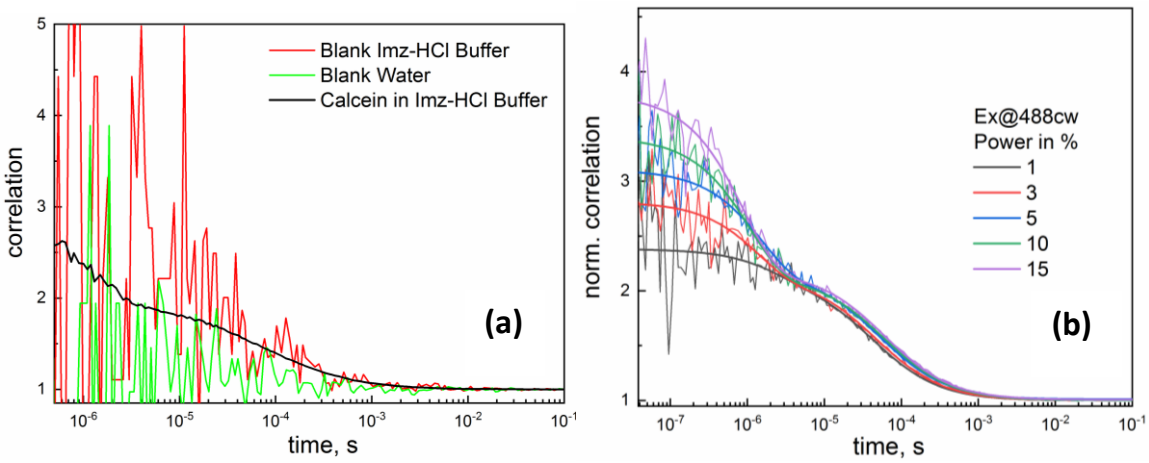

Figure 5.4: **(a)** Three minute control FCS measurements for comparison of actual signal over the background. Background signal from blank buffer and water are relatively much weaker than calcein in imidazole buffer. **(b)** Excitation intensity dependent FCS curves of calcein in buffer, data recorded for 180 seconds each. Solid lines are the fits following equation 5.1. Increase in laser power leads to broadening of observation volume and thus increase in diffusion time.

FCS measurements were performed by exciting the sample with less than 30 μW of a cw 488 nm argon ion laser. Typical measurement time was a few minutes, and the chosen low excitation power prevented any significant population of the triplet state (see Figure 5.4b).

5.3.1 Interaction kinetics of Calcein with Iron (III)

To demonstrate the reliability of FCS for the measurement of binding constants, we studied the complexation of iron with calcein and checked the results against ensemble spectroscopy measurements.

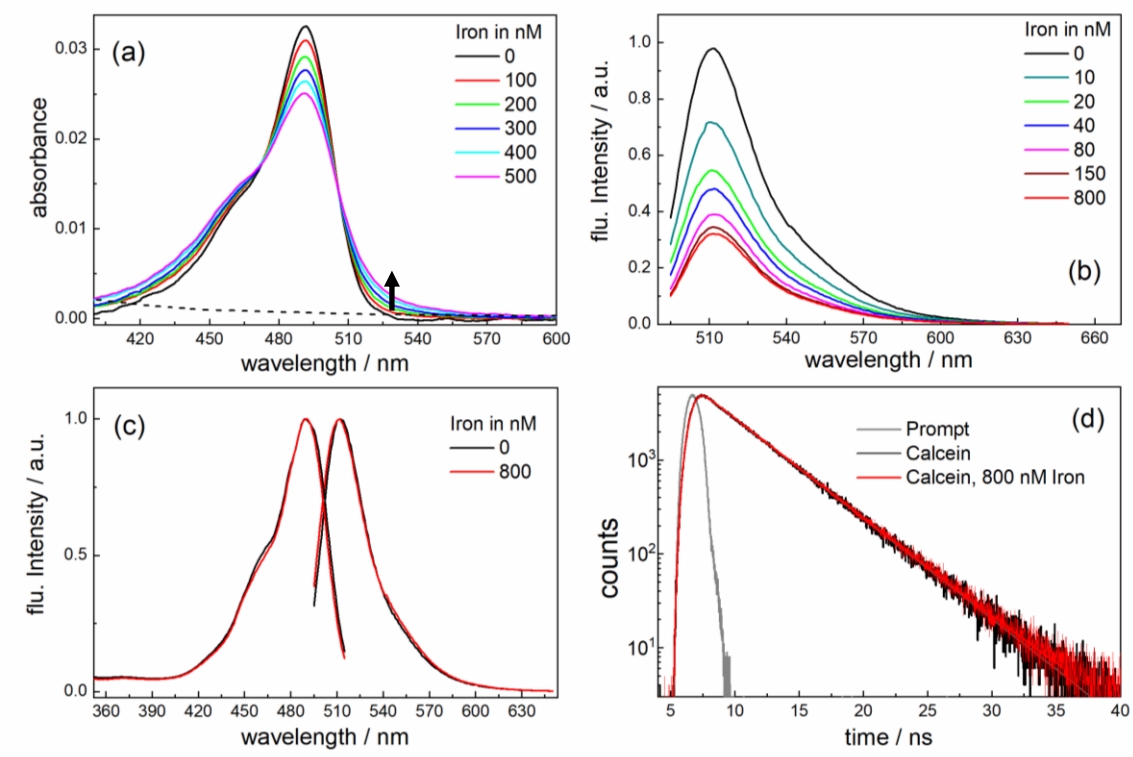

Figure 5.5: (a) Absorption spectra of ~0.5 μM calcein in buffer with gradual addition of iron. Dashed line represents absorption spectra of instantly prepared 1 μM Mohr salt in buffer. **(b)** Fluorescence intensity of calcien (with excitation at 488 nm) gradually decreases with increase in iron concentration. **(c)** Normalized excitation and emission spectra of calcein in absence and presence of 800 nM iron. **(d)** Fluorescence decay traces of calcein remain unaltered in absence and presence iron ions.

We recorded steady-state (SS) absorption and fluorescence emission spectra of calcein together with time-resolved (TR) fluorescence intensity decays as a function of iron concentration (see Figure 5.5).[93]

Binding of metal ions to calcein (L + M ↔ ML) results in a strong quenching of fluorescence by ~ 70% (see Figure 5.5b), but there is no change in the emission spectrum. This observation excludes the possibility of complex formation between excited the state of calcein (L*) and iron. We did also not observe any noticeable fluorescence signal at an excitation wavelength of 540 nm, corresponding to the absorption maximum of the ground-state ML complex, indicating its non-emissive nature. The excited state decay rate (2.5×10^{8} s^{-1}) remained unaltered even in the presence of 800 nM iron (see Figure 5.5d), which suggests the absence of dynamic quenching (i.e. collisional interaction) in the studied concentration range. This is also expected from the Stern-Volmer equation assuming a bimolecular diffusion rate constant (~10^{10} $M^{-1}s^{-1}$) as the maximum possible quenching rate constant.[11] Therefore, in the present system, ground-state complexation gradually depletes the concentration of free fluorescent calcein and thus leads to a gradual decrease in observed fluorescence upon addition of iron. The observed gradual increase in correlation amplitude of the FCS curves (see Figure 5.6b) is due to the decrease of the average number of fluorescent molecules *N* within the detection volume, in agreement with results from SS measurements.

Normalized FCS curves of calcein in absence and presence of iron are almost identical (see Figure 5.6b inset), which demonstrates that addition of iron thus not change the intersystem crossing rate (triplet state population) of calcein. A Job plot confirms a stoichiometry of 1:1 for the ML complex (see Figure 5.6c).

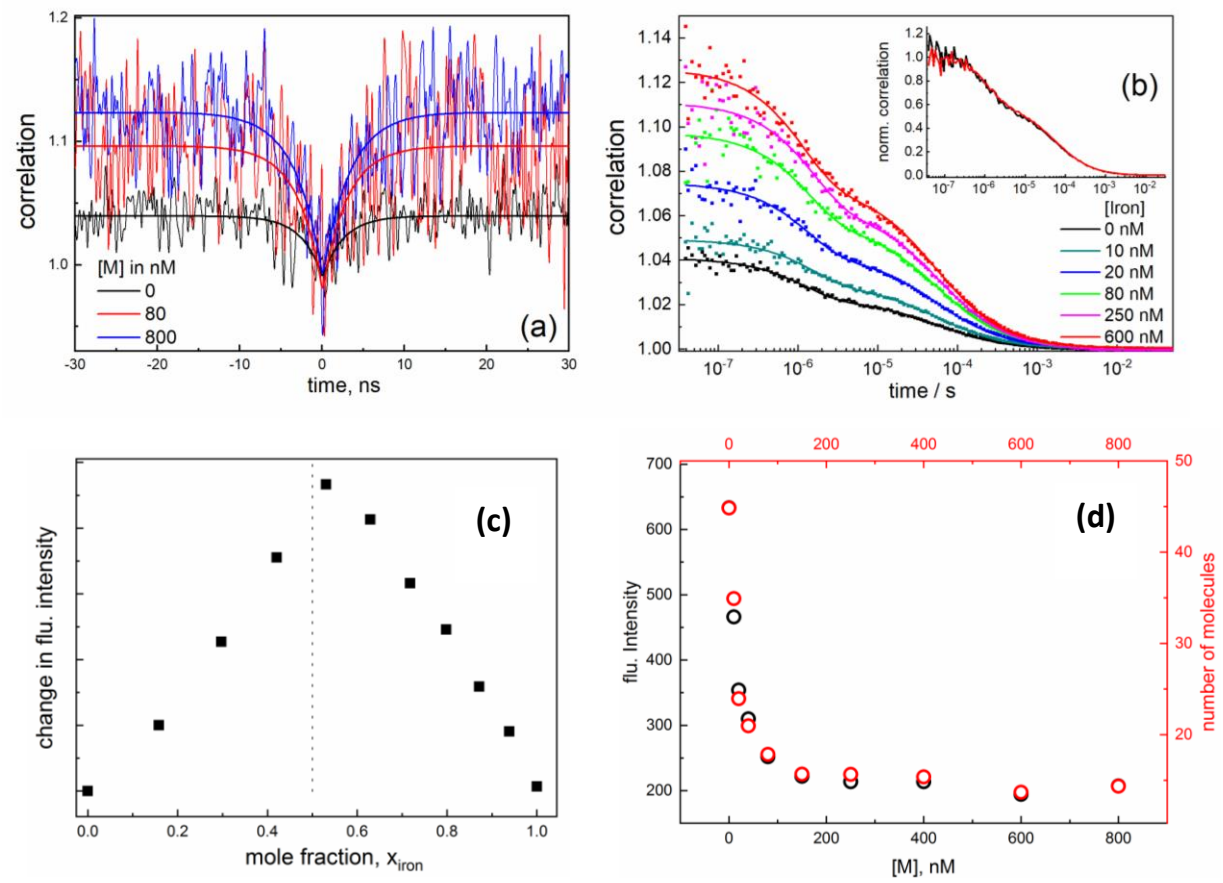

Figure 5.6: (a) Photon antibunching curves generated from the same FCS data set shown in (B) for calcein-iron system. Photophysics of calcein remains unaffected by the addition of iron, as is evident from a comparison of normalized correlation curves as shown in the inset (b). Solid lines in (b) are fits of equation 5.1. Job plot for calcein-iron system in buffer is shown in **(c)** which indicates 1:1 complexation. Plot of SS fluorescence intensity of calcein (from ensemble fluorescence quenching measurement) and number of free calcein molecules (from FCS measurements) as a function of added iron concentration is shown in **(d)**.

SS intensity values from ensemble measurements and number-of-molecule values from FCS measurements display a similar decreasing trend (see Figure 5.6d) upon metal ion addition. It should be noted that photon anti-bunching curves (i.e. nanosecond FCS) calculated from the same FCS raw data do also show a gradual decrease in the average number of molecules within the detection volume (see Figure 5.6a). However, antibunching relaxation rates remain unaltered by iron, again indicating the absence of collisional quenching.

Next, we plotted the average number of molecules (i.e. inverse of correlation amplitude in FCS or photon antibunching) and the SS fluorescence intensity as functions of metal ion concentration. These curves where then fitted with a binding model, see eq. (5.3).[23] The fit yielded a value for the binding constant K_a and coefficient n, being equal to the binding stoichiometry (expected to be 1 for calcein-iron). The corresponding plot is shown in Figure 5.7a, yielding a global value of logK_a = 7.9, with excellent agreement between FCS (7.21 (±0.8) x 10^7 M^{-1}) and SS (7.33 (±0.44) x 10^7 M^{-1}) measurements.

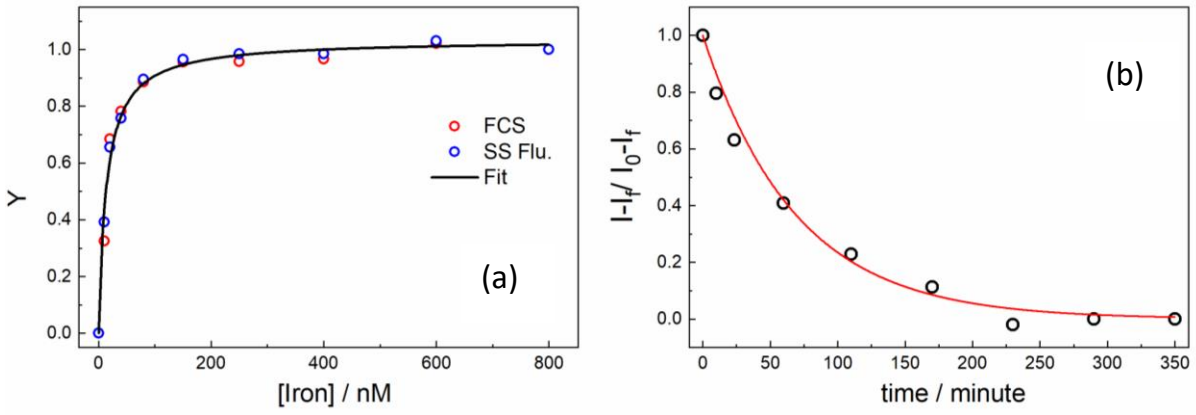

Figure 5.7: (a) Normalized binding curve for calcein-iron interactions, obtained from SS and FCS measurements. The solid line is a global fit of the binding curves with K_a = 7.13 (±0.5) × 10^7 M^{-1} for 1:1 complexation. **(b)** Time dependent complexation kinetics for calcein-iron system with [iron] = 500 nM. Solid line is the fit following equation 5.4.

As already discussed before, the slowness of the association/dissociation rates for metal ion/ligand complexes prevents us to use FCS for determining the rate constants directly (though it is possible for faster reactions like binding of small organic molecules to a supramolecular host).[37,39-41] For obtaining these rate constants k_f and k_b, we recorded the SS fluorescence intensity as a function of time after the addition of metal ions to a calcein solution. The results are shown in Figure 5.7b. For calcein-iron with K_a = 7.13 x 10^7 M^{-1}, the determined values of k_b and k_f are 2.96 (±0.09) x 10^{-5} s^{-1} and 2.11 (±0.08) x 10^2 $M^{-1}s^{-1}$, respectively.

5.3.2 Interaction kinetics of Calcein with Uranyl (II)

Next, we turned to the binding kinetics of uranyl ions UO_2^{2+} with calcein. Ensemble spectroscopy (see Figure 5.8) reveals strong (~ 80%) fluorescence quenching due to ground-state 1:1 complexation, similar to that of calcein-Fe^{2+}.

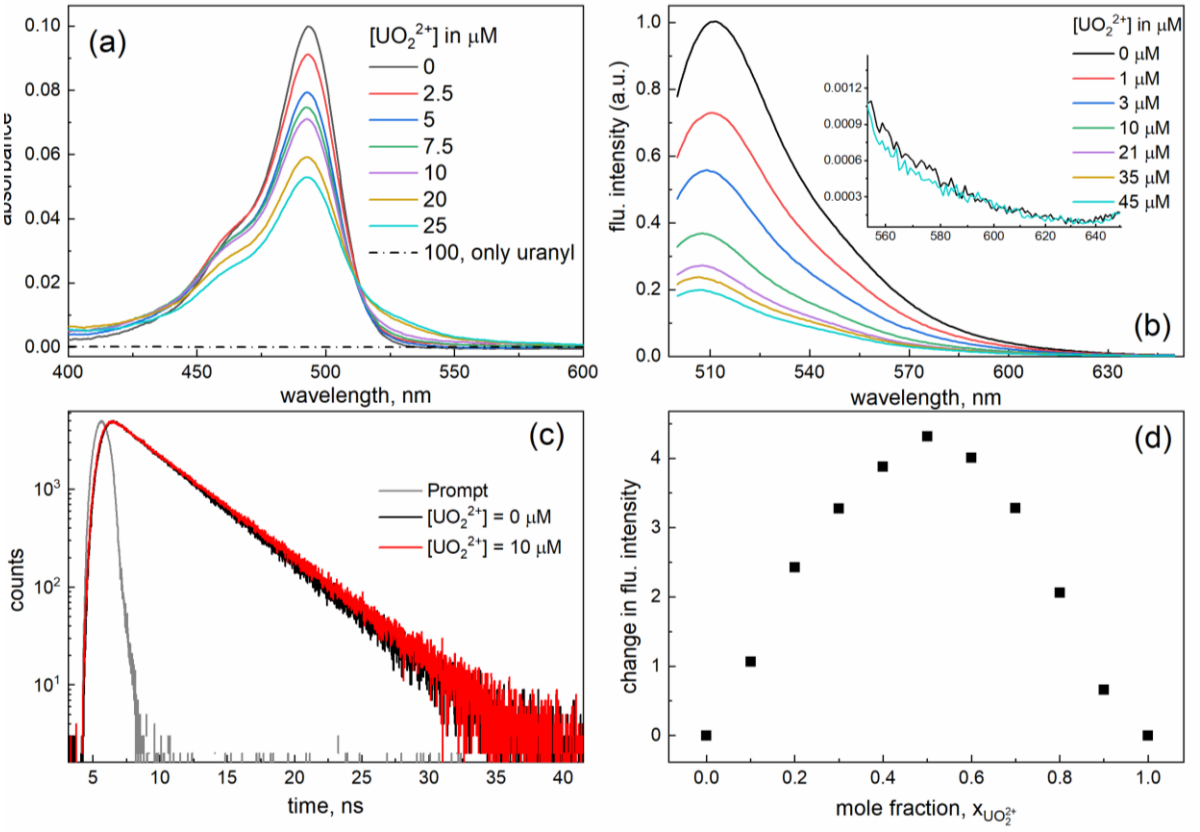

Figure 5.8: (a) Absorption spectra of calcein in buffer with gradual addition of uranyl ion. Dash-dotted line represents absorption spectra of 100 μM UO_2^{2+} in buffer. Observation of new band at 540 nm is probably due to absorption by the ground state complex. **(b)** Fluorescence intensity of calcien (with excitation at 485 nm) gradually decreases with the addition of UO_2^{2+}. **Inset** shows emission spectra of Calcein with excitation at 540 nm in absence and presence of 45 μM UO_2^{2+}. This indicates very weakly emissive complex if not non-emissive in nature. **(c)** Fluorescence decay traces of calcein remain unaltered in absence and presence UO_2^{2+}. **(d)** Job plot for calcein-UO_2^{2+} system in buffer. Change in fluorescence intensity of calcein in presence and absence of metal ion at different mole fractions of UO_2^{2+} indicates 1:1 complexation.

Variation in photon antibunching, FCS and binding curves are shown in Figure 5.9. Excellent agreement between binding curves obtained from ensemble and from FCS measurements again underlines the reliability of FCS in studying complexation (or dissociation) reactions. Global fitting of the binding curves yields a K_a value of 4.69 (±0.4) x 10^5 M^{-1}. Individual fits return a value of 4.67 (±0.35) x 10^5 M^{-1} and 3.99 (±0.5) x 10^5 M^{-1} for FCS and SS measurements, respectively.

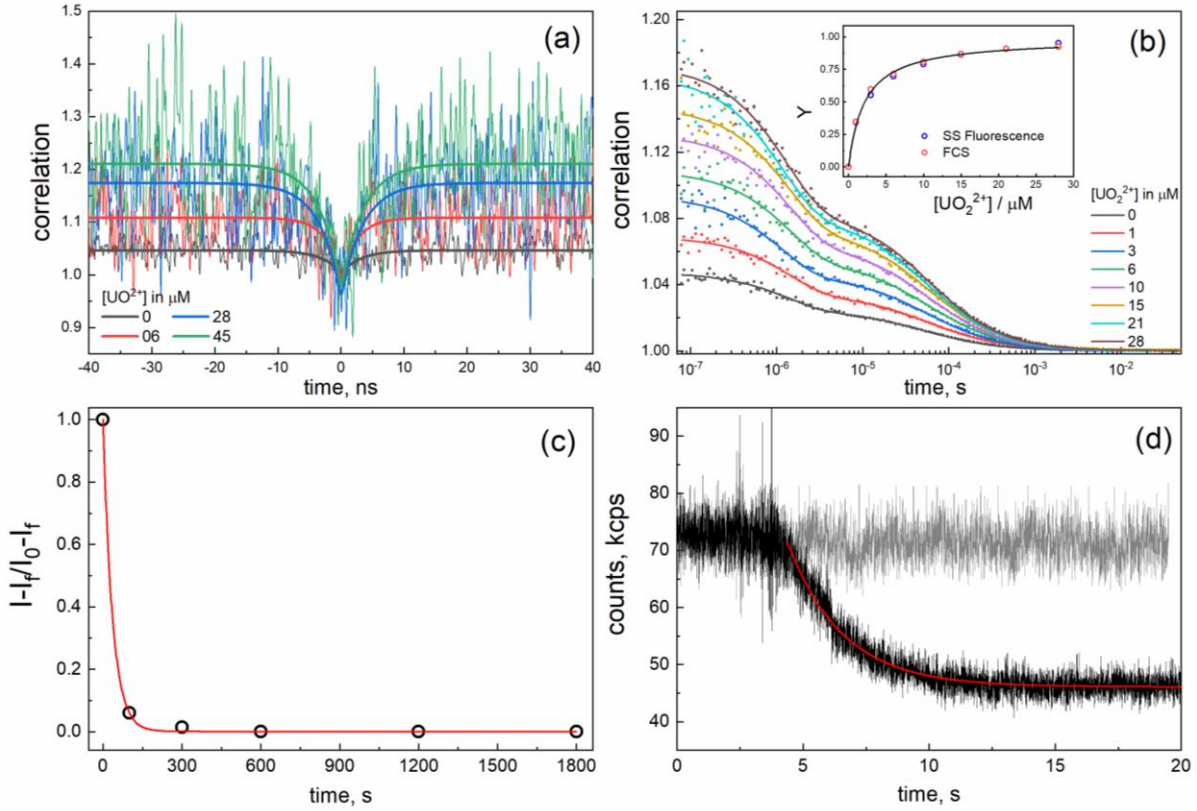

Figure 5.9: Photon antibunching **(a)** and FCS correlation curves **(b)** of 38 nM calcein with varying concentrations of UO_2^{2+}. **Inset (b)** Normalized binding curves for calcein- UO_2^{2+} system estimated from ensemble and FCS measurements corroborate nicely. The solid line is the global fit of the binding curves for 1:1 complexation. **(c)** Time dependent complexation kinetics for calcein-UO_2^{2+} systems with SSF intensity measurement [UO_2^{2+}] = 5 µM. Solid line is the fit following equation 5.4. **(d)** Fluorescence time trace of calcein recorded on the FCS setup in absence (grey) and presence (black) of around 8 µM urnayl ions. Large spikes in the 2 – 4 second region are due to addition and mixing of very small volume of blank buffer and uranyl solution for the control and actual kinetics measurement, respectively. Solid line is the fit curve following equation 5.4

This is similar to an earlier reported value of 4.7 x 10^5 M^{-1} from ensemble spectroscopy measurements in acidic pH = 4 for selective binding of calcein with uranyl in the presence of other metal ions.[94]

Next, for obtaining these rate constants k_f and k_b, we recorded the SS fluorescence intensity as a function of time after the addition of metal ions to a calcein solution. The results are shown in Figure 5.9c. For calcein-uranyl with K_a = 4.69 x 10^5 M^{-1}, we find k_b = 8.38 (±0.06) x 10^{-2} s^{-1} and k_f = 3.93 (±0.07) x 10^4 $M^{-1}s^{-1}$, respectively. For these values, the equilibrium relaxation time (under pseudo unimolecular condition), $\tau_R = 1/(k_f[M]_0+k_b)$,[37,39,40] is several orders of magnitude larger than the diffusion time of few tens of microseconds. (τ_R = 7.4 x 10^3 s for calcein-iron and τ_R = 9.7 s for calcein-UO_2^{2+}). Comparison of the dissociation rates shows that uranyl-calcein complexes are thermodynamically ~100 times less stable than iron-calcein. The much faster complex formation rate for uranyl ions is related to its substantially lower hydration energy (primarily due to reduced charge-to-radius ratio). Besides bulk measurements, we measured the time dependent intensity also on our FCS setup after adding (and rapidly mixing) uranyl ions into calcein solution in lab-tek chambers (see Figure 5.9d). Analysis of these intensity time trace gives a value of k_f = 3.43 (±0.12) x 10^4 $M^{-1}s^{-1}$, and k_b = 7.3 (±0.2) x 10^{-2} s^{-1} (using the earlier determined K_a value).

It is important to mention here the works of Wunderlich et al.[95] where rapid mixing and hydrodynamic focusing in a calibrated microfluidic channels has been used to precisely monitor slow kinetics of few milliseconds to hundreds of seconds for protein folding & conformational changes in presence of around 3 M guanidinium chloride with single molecule sensitivity. Such a sophisticated microfluidic channel based sensitive detection is ideal for slow kinetics with small amount of sample volumes (~ 10 μl) where reaction is essentially irreversible during the

observation time accessible at equilibrium. In the present work, we adopted a simple method to follow the kinetics and the results obtained are comparable with ensemble kinetics parameters. As preliminary kinetic data suggests reaction times are of the order of few tens of seconds for the studied sample concentrations, so we used quick mixing in Labtek-chambers to follow the complexation reactions and cross-checked with appropriate control measurements.

5.3.3 Interaction kinetics of Calcein with Europium (III)

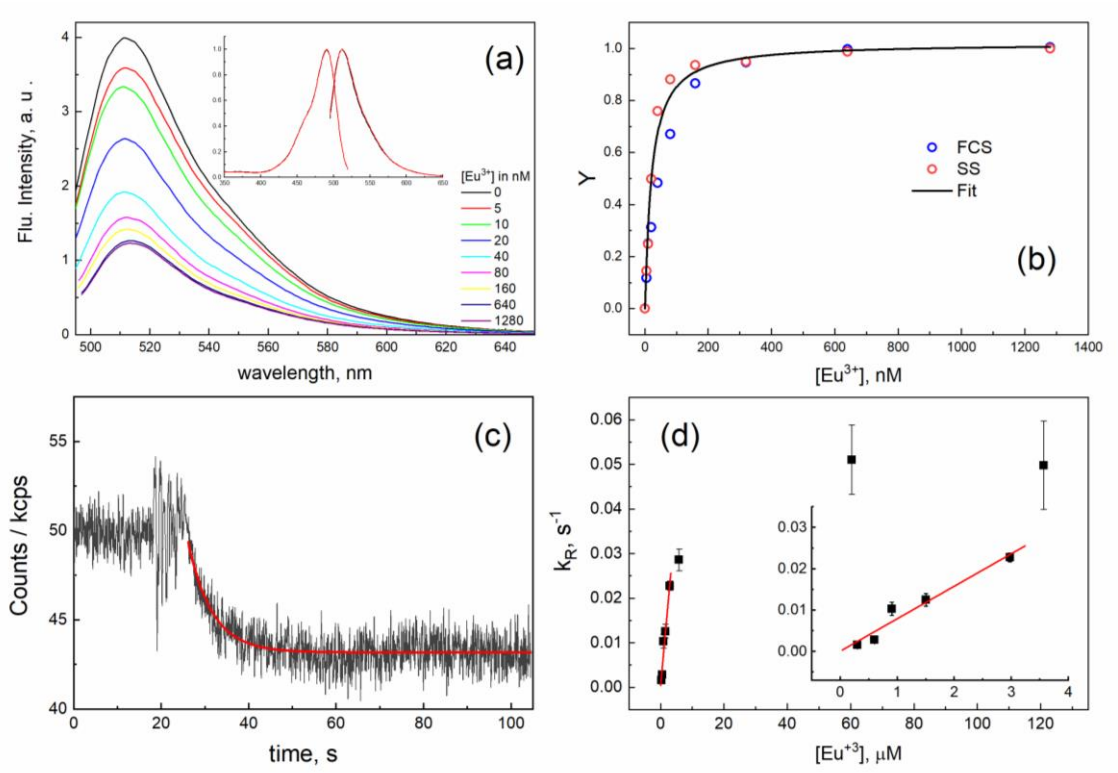

Figure 5.10: **(a)** Fluorescence intensity of calcien (with excitation at 485 nm) gradually decreases with the addition of Eu^{3+}. Inset shows normalized excitation and emission spectra of calcein in absence and presence of 1.2 μM europium. **(b)** Normalized binding curves for calcein-Eu^{3+} system estimated from ensemble and FCS measurements. The solid line is the fit of the binding curves for 1:1 complexation. **(c)** Fluorescence intensity trace of calcein. Large fluctuations around 20s is due to addition and mixing of Eu^{3+} stock solution in calcein solution for a final metal ion concentration of 60 μM. Solid line is the exponential fit curve. The fitted rate constants are then plotted as a function of added metal ion concentration **(d)**. The rate constants for < 4 nM metal ion concentrations were fitted with a linear function (inset) to obtain forward and backward rate constants as slope and intercept, respectively.

Ensemble and FCS results for the interaction of calcein with europium are similar to those obtained for the other metals (see Figure 5.10). The relaxation rate k_R ($= \tau_R^{-1}$) increases linearly with increasing metal concentration with slope (i.e. k_f) 7.9 (±0.8) x 10^3 $M^{-1}s^{-1}$ and intercept (i.e. k_b) 8.5 (±0.9) x 10^{-5} s^{-1} for ion concentrations below 4 μM. The relaxation rate saturates at a value of 0.05 s^{-1} for larger Eu^{3+} concentrations.

5.3.4 Interaction kinetics of Calcein with Americium (III)

Next we demonstrate the capability of FCS for determining association/dissociation rates and binding constants with a minimum sample quantity (~ 1 μl solution of ~ 1 nM), thus reducing the required sample amount (and thus radioactivity) by nearly six orders of magnitude as compared to conventional ensemble measurements. We performed FCS measurements with 1 μl calcein solution placed between two glass cover slips with a spacer of ~ 0.15 mm. Recorded FCS curves were found to look almost identical to curves regularly recorded with ~ 50 μl solution on top of a glass coverslip (see Figure 5.1). After this, we recorded FCS curves on 1 μl ~0.7 nM calcein solutions containing varying concentration of Am^{3+}, prepared by dilution of Am^{3+} stock solution in a safe environment. Measurements were always performed one day after sample preparation (see Figure 5.11a). Normalized FCS curves (see Figure 5.11a inset) indicate unchanged triplet state dynamics of calcein in the presence of few nM Am^{3+}, and without any appreciable change in diffusion coefficient. As expected, fluorescence quenching due to ground state complexation gradually decreased the average number of molecules N (reflected by an FCS amplitude increase) and saturated at large concentrations of Am^{3+}. Fitting of the binding curve (assuming 1:1 complexation) yields an association constant K_a value of 3.2 (± 0.7) x 10^8 M^{-1}, indicating strong binding between Am^{3+} and calcein in imidazole buffer of pH 6.5.

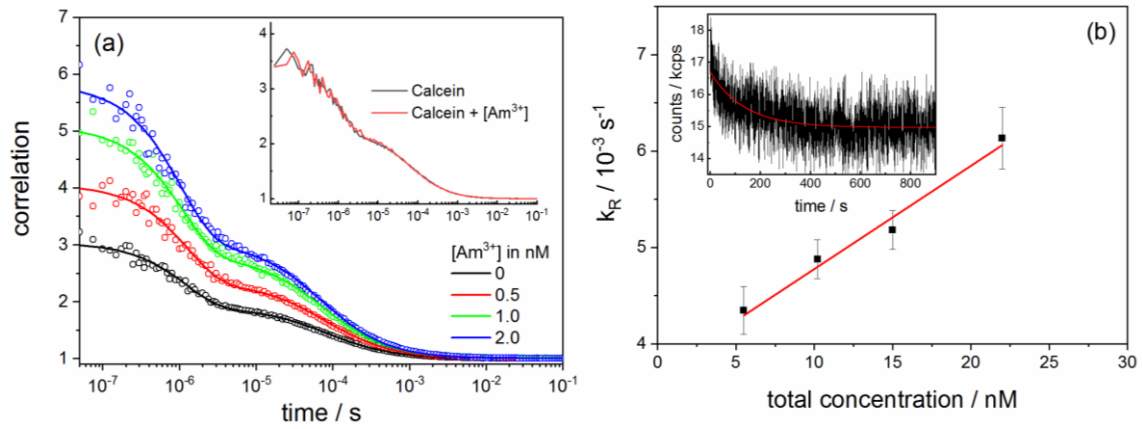

Figure 5.11: (a) FCS data for ~ 0.7 nM calcein for varying concentration of metal ions. Solid lines are the fit curves. (Inset) Normalized FCS curves for calcein in the presence and absence of 2 nM Am^{3+}. (b) The fitted rate constants from the fluorescence intensity traces (inset) just after addition of Am^{3+} into calcein solution are plotted as a function of total calcein & metal ion concentrations. Forward and backward rate constants were obtained from linear fits of the rate constants

This larger value, as compared to that for europium, is due to a higher stability and selectivity of calcein towards, which is also observed for other ligands such as 2,6-bis(1,2,4-triazin-3-yl)pyridine.[8] Measurements with other available processed Am^{3+} stock solutions show even a larger binding constant (> 10^9 M^{-1}). We assume that this is due to presence of other trace metal impurities in Am^{3+} stock solutions, but also to the difficulty to precisely adjust the final extremely low Am^{3+} concentrations in the measurement volume.

At very low metal ion concentrations, the binding time scales between Am^{3+} and calcein become very long. To avoid sample drying, long time excitation intensity fluctuations, and photo-bleaching, we thus used slightly higher Am^{3+} concentrations for the kinetic measurements so that one measurement lasted not longer than 10 minutes. We used 1 µl solutions with a maximum of 16 nM Am^{3+} (activity ~0.48 Bq) in ~5 nM calcein (see Figure 5.11b). Because of the limited concentration range of metal ions with respect to calcein (< 5 times), we correlate the relaxation rate against the total concentration of metal and ligand instead of only the ligand concentration,

as is usually under pseudo uni-molecular conditions. Thus, the total reaction rate is calculated as $k_R = k_f([M]+[L])+k_b$.[37,96] The inset in Figure 5.11b shows a linear increase in relaxation rate k_R with increasing metal concentration, yielding k_f = 1.08 (±0.1) x 10^5 $M^{-1}s^{-1}$ and k_b = 3.7 (±0.1) x 10^{-3} s^{-1}. For precise estimation of rate constants, we also fitted the intensity time traces with a general solution for a reversible bimolecular reaction (see appendix A2 for derivation), which independently returned a K_a value of 6.8 (±0.3) x 10^8 M^{-1}, for a nearly similar values of k_f and k_b (i.e. 4.8 (±0.1) x 10^5 $M^{-1}s^{-1}$ and 0.7 (±0.1) x $10^{-3}s^{-1}$ respectively).

In comparison to americium, europium shows complex formation rate constant that is one order of magnitude smaller. This can be expected when taking into account that the charge-to-radius ratios of americium (z^2/r = 7.9 with r = 1.14 Å for $[Am(H_2O)_9]^{3+}$) and europium (z^2/r = 8.5 with r = 1.062 Å for $[Eu(H_2O)_9]^{3+}$).[97] As a result, europium shows higher hydration energy than americium, and as a result the displacement of coordinated water molecules by the ligand is expected to be slower for europium. Moreover, when compared to americium, europium is also known to form relatively labile complexes with oxygen-donating ligands, which is further substantiated by the obtained dissociation rates. In the case of uranyl, although the lower charge density (z^2/r = 3.703 with r = 1.08 Å for $UO_2(H_2O)_5^{2+}$) leading to a reduced hydration energy should favor faster complexation, the obtained experimental results show a slower formation rate than for americium. This is probably caused by steric hindrance aka reduced accessibility of the calcein binding pocket by uranyl ions, due to the latter's two axial oxygen atoms which requires re-structuring of the calcein's ligating arms for effective chelation.[98]

5.3.5 Sequestration Reactions

Finally, we also assessed FCS for measuring sequestration reactions. We demonstrate this by adding a strong chelator (L_s) to the solution of ML complexes, keeping the total

concentration of L constant. For the calcein-iron system, we used deferoxamine[90,99] (DFO; a known chelator in the treatment of acute iron poisoning, logK_a = 30. Addition of 800 nM iron to the calcein solution leads to an increase of the correlation amplitude due to quenching by ground-state ML complexation (see Figure 5.12a).

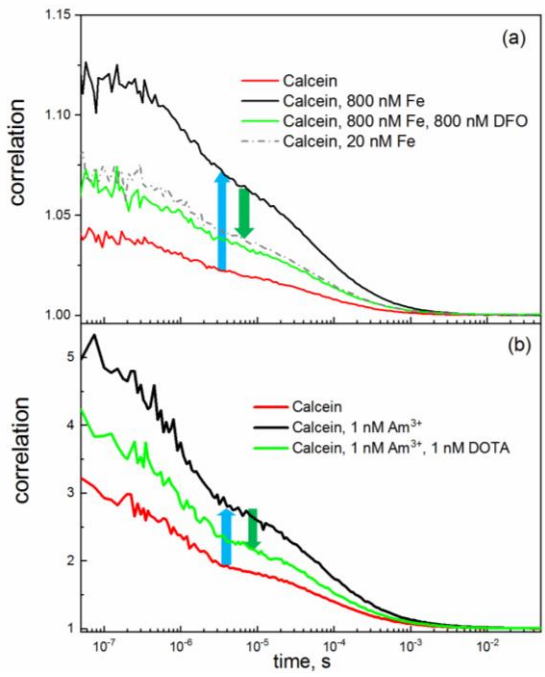

Figure 5.12: Fluorescence recovery (or decrease in correlation amplitude) in presence of L_s is due to increase in free calcein population owing to dissociation of calcein-iron **(a)** and calcein-americium **(b)** complexes. Blue and green arrow indicates fluorescence turn-off and turn-on events, respectively.

Subsequent addition of 800 nM DFO leads to a decrease of the correlation amplitude (i.e. increase in the number of free fluorescent calcein molecules). This is due to extraction of iron (M) from the ML complexes by L_s, leaving calcein as free ligand (L) and resulting in the formation of DFO-iron complexes (i.e. ML + L_s ↔ ML_s + L, without any change in calcein photophysics, see Figure 5.13).

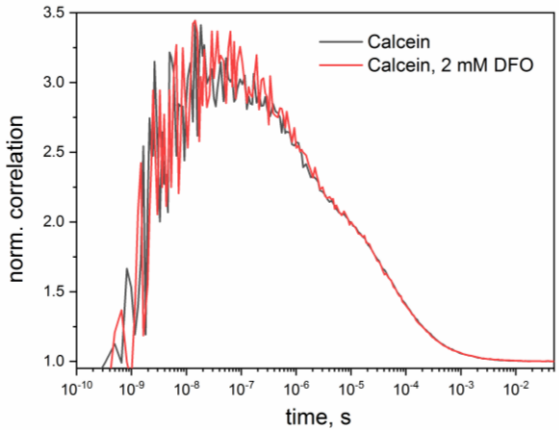

Figure 5.13:. Presence of DFO does not alter the photophysics of calcein. However, to be noted that the correlation amplitude shows marginal decrease, probably due to change in calcein population depending on the presence of trace metals in buffer solution prior the addition of DFO.

Analysis of these amplitude changes shows a nearly 41% recovery of L within 1 hour of DFO addition. The correlation amplitude for the last system is similar to that obtained with 20 nM iron in calcein, suggesting a recovery of ~ 98% iron by DFO for the studied calcein-iron system. We observed similar trends for the calcein-americium system using DOTA[100] (1,4,7,10-tetraazacyclododecane-1,4,7,10-tetraacetic acid, logK_a = 24) as L_s, see Figure 5.12b.

5.4 Conclusion

In the present chapter, we have shown how to use FCS for measuring slow binding kinetics of metal ions to chelators, at nanomolar concentrations and with only microliters of sample. For doing that, we have performed concentration dependent FCS measurements and determined the average number of fluorescent molecules within the detection volume as a proxy for the concentration change upon metal ion addition. Although similar information can be obtained from bulk intensity measurements, the ultimate sensitivity of FCS makes it an ideal tool for measuring reaction kinetics of hazardous materials. Moreover, FCS measurements yield additional information that is not easily accessible by ensemble measurements. For example, the

observed unchanged photophysics and fluorescence lifetime upon metal ion addition indicates the negligible impact of metal ions on intersystem crossing (due to heavy atom effect) or additional collisional quenching.

FCS is a general and very versatile technique and only needs a fluorophore (i.e. fluorescent ligand or fluorophore tagged ligand) which interacts with metal ions. Designing suitably tagged chelators for studying metal ion complexation of rare and difficult sample is rather straightforward, taking into account the vast existing inventory of fluorophores and the wide variety of available conjugation strategies. More effort has to be invested when aiming at fluorescent chelators with high metal ion selectivity within a background of several competing ions. However, one could apply a suitable sample pre-treatment that removes interfering metal ions, which lowers the requirement of high selectivity for the fluorescent reporter.

It is worth mentioning that commonly used time-resolved laser-induced fluorescence spectroscopy (TRLIFS)[2,10] is another very sensitive technique that is able to directly detect the photoluminescence of actinides (even at sub-nanomolar concentrations) and to characterize their oxidation states from the analysis of spectral features. However, FCS has significant advantage when it comes to bio-molecules or in-vivo experiments under ambient conditions (as discussed in Chapter1).[76,77] Apart from complexation & sequestration involved in bio-speciation & bio-sequestration research, FCS methods can be also be useful for research concerned with the separation of highly active actinides from lanthanides (an important topic for long term & safe disposal of nuclear waste materials), with sorption/inclusion of active metal ions into minerals, or with their leaching from rocks/vitrified matrix. The primary process involved in all these scenarios is complexation kinetics, and as we have shown here, FCS can be an extremely useful tool for studying such reactions.

CHAPTER 6

Photophysics of Carbon Nanodots

6.1 Introduction

Fluorescent carbon nanodots (CNDs) have attracted immense attention in past one decade due to their simple and inexpensive synthesis, high fluorescence quantum yield, high photostability, easy functionalization, non-toxicity and so the bio-compatibility. All these novel properties of CNDs make them a serious contender for various single molecule sensitive applications like bioimaging, protein tracking and metal ion sensing, etc.[53,54,56,101] Therefore, numerous efforts have been undertaken to unravel the photophysics and origin of photoluminescence of carbon dots (CNDs) to gain fundamental insights and for better utilization of CNDs in various applications.[101-106] Here our particular interest is to exploit the abundance of functional groups present on these novel materials as a marker for investigation of metal ions and their interaction dynamics.

The most fascinating aspect of their photophysics is their excitation dependent fluorescence behavior which has led to several hypotheses, starting from particle size distribution[58,107] to the presence of different emissive states.[56,59-61] In addition, single particle

measurements confirm single step photo bleaching similar to regular fluorophores[103,108] but with one or several discrete intensity levels for a fraction of particles.[60] On the contrary complete absence of blinking is also reported.[61] Furthermore, contrary to excitation dependence, single particle results also highlight excitation independent emission spectra for CNDs.[108] Possible contributions from polarity, pH, surface passivation, etc. towards the excitation dependence or independence have also been established.[62,109,110] Recently, non-equilibrium solvent configuration due to slower solvent relaxation in polar media during its excited state lifetime has also been proposed for the excitation dependent emission of CNDs,[62] similar to the red edge excitation effect reported for graphene oxide (GO).[111] The non-equilibrium solvent configuration due to slower dielectric relaxation during the excited state lifetime is possible but the strong Stokes shift (of about 2000-6000 cm^{-1})[62] observed for all resolved components of fluorescence emission remain unexplained, as slow relaxation results in small Stokes shifts of around 1000-2000 cm^{-1}.[112]

Therefore, in present chapter we will address this intense debate on the origin of large excitation dependent fluorescence spectral shift. We will highlight significant fundamental insight into the photoluminescence of CND from different SS and time resolved ensemble spectroscopic investigations and substantiate various discrete proposals suggested for the exotic observation of huge excitation dependent spectral shift, without violating the classical Kasha−Vavilov rule.[11,16] We will provide definitive evidence for the involvement of discrete multiple electronic states for the excitation dependent emission in carbon nanodots. We will also explore origin of these multiple electronic states as due to molecular fluorophore, carbon nanoparticle and different types of aggregates. Lastly, we will discuss the capability of CNDs as

a fluorescent chelators for sensing metal ions i.e. Uranyl ion to study their interactions with both single molecule and ensemble spectroscopy.

6.2 Experimental details

6.2.1 Materials

All reactions were performed in oven-dried (120 °C) or flame-dried glass apparatus under dry N_2 atmosphere. Citric acid and urea were purchased from Aldrich. Column chromatography was performed on Florisil (60–100 mesh). Water was obtained from Milli-Q System (Millipore) and used in all synthetic and spectroscopic investigations. Commercially available citrazinic acid (Sigma-Aldrich) was used without further purification. Spectroscopy grade solvents (ethanol, methanol, dimethyl formamide and dimethyl sulfoxide) were procured from M/s. S. D. Fine Chemicals and used without further purification. All synthesis and purification of carbon nanodots were done in collaboration with Bio-Organic Division, BARC.

6.2.2 Synthesis

Citric acid and urea mixture (in 1:3 ratio) was heated to around 210^0 C on a heating mantle for 10 min under N_2 conditions to synthesize carbon nanodots. The obtained yellow-brown reaction mixture was dissolved in minimum 9:1 ethanol-water solvent. The solution was centrifuged and the supernatant was purified by florisil based column chromatography. The highest polar pure fraction of synthesized CND was used for the investigation of excitation dependent fluorescence behaviour of CNDs.

6.2.3 Methods

Ground-state absorption, steady state (SS) fluorescence, time resolve fluorescence and FCS spectrum were recorded using similar setups mentioned in previous chapters.

FTIR spectra were recorded on Bruker Tensor III. High resolution transmission electron microscopy (HR-TEM) images were recorded with Carl Zeiss Libra 200 kV on carbon coated cupper grids. For atomic force microscopy (AFM) measurements sample were loaded on mica plates. Regular TEM images were recorded with Carl Zeiss Libra 120 kV. AFM images were recorded with AFM-A100 from APE Research. Raman spectra were recorded with 785 nm solid state laser using LabRAM HR800 from Horiba Yobin Yvon, France. ^{1}H-NMR spectra were recorded on 500 MHz (Varian), using DMSO-d6 as solvent.

6.3 Results and Discussion

6.3.1 Origin of excitation dependent fluorescence in CNDs

SS absorption spectra show major bands at 220 and 350 nm and were accompanied by two other very weak absorption bands at around 450 and 520 nm (see Figure 6.1a). The 220 and 350 nm band shows properties of π-π^* and n-π^* transitions respectively. SS emission spectrum is recorded at different excitation wavelengths and is shown in Figure 6.1b. As expected, the emission spectra show excitation dependence and shift toward longer wavelengths.

A closer inspection of the emission spectrum shows multiple emission bands at around 450, 540 and 600 nm region (Figure 6.1b). Additionally, the fluorescence excitation spectra (Figure 6.1c) at different emission wavelengths also corroborate the involvement of at least three electronic transitions around 350, 450 and 520 nm. Thus it is expected that, the redistribution of fluorescence intensity among different emission bands results in the excitation dependent multicolored fluorescence spectra of CNDs. So, in order to certify the involvement of multiple electronic states in CNDs, we recorded SS excitation anisotropy (r_{ss}) of CND in glycerol, which

is a highly viscous media where reorientation of the molecules is negligible during their excited state lifetime.[11,16]

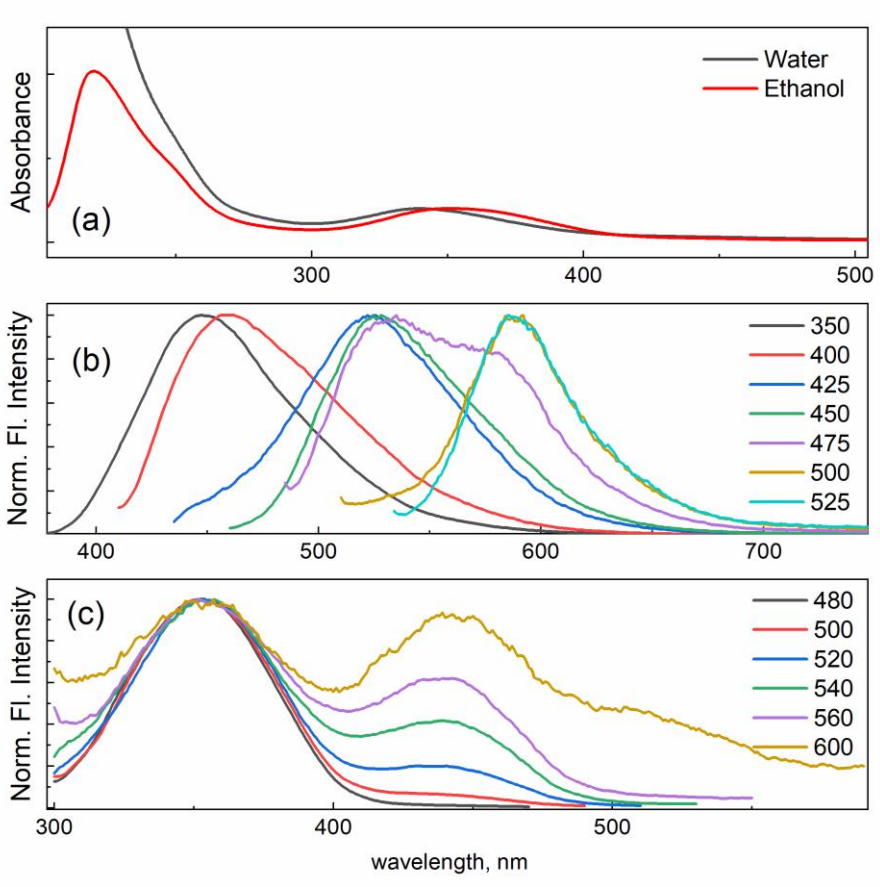

Figure 6.1: Normalized steady-state absorption (a), emission (b) and excitation (c) spectra of CND. Absorption spectrum is recorded in ethanol and water whereas emission and excitation spectrum is recorded in water only. The mentioned excitation and emission wavelengths are in nm scale.

It is clearly evident from Figure 6.2a that the fundamental anisotropy (r_0) values are relatively constant across the three long wavelength excitation/absorption bands and are individually different. It means, the orientations of transition diploes are different for different absorption or excitation band. This distinct anisotropy values and hence the different angles (β) between the absorption and emission dipoles for the 350, 450 and 520 nm excitation bands

certainly prove the existence of multiple electronic transitions. However, the lack of anisotropy dependence on emission wavelength at a particular excitation wavelength (Figure 6.2b) is expected for the emission from the lowest electronic state.[11,16]

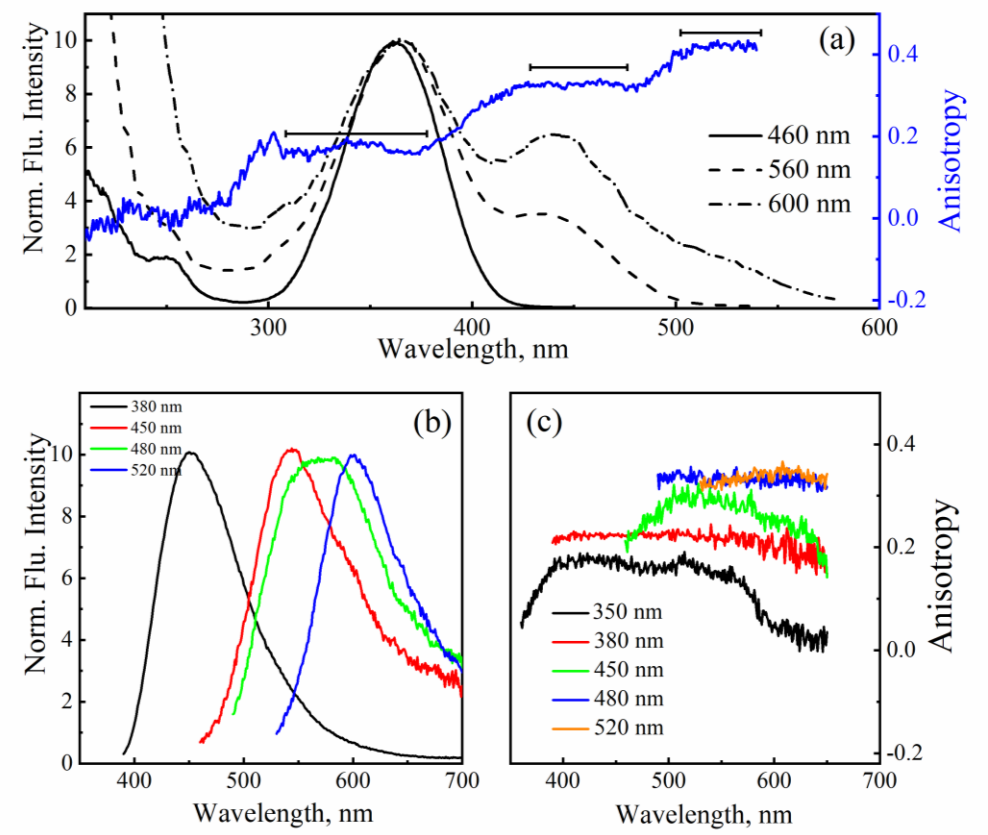

Figure 6.2: Fluorescence excitation spectra and excitation anisotropy spectra of CND in glycerol (a) indicates multiple electronic transitions. Steady-state emission anisotropy (c) and emission spectra (b) of CND in glycerol as a function of excitation wavelength further supports the involvement of multiple electronic states.

This is clearly evident for excitations at the main absorption band over the majority of emission wavelengths, except at far red region. However excitation at 450nm displays non-monotonous dependence of anisotropy on emission wavelength; r_{ss} value initially increases and then decreases.

This apparent behavior is only possible when emission occurs from more than one electronic state and when these states show different emission spectra.[11,16] At even higher excitations wavelengths (480 nm and above), anisotropy values remain nearly independent of emission wavelength. All these results consolidate the involvement of multiple electronic states for CND emission, possibly due to the presence of ground state heterogeneity as it does not violate the classical Kasha-Vavilov rule.[11,16]

It is worth mentioning here that the observation of discrete multiple electronic states from one particle seem unlikely due to the small energy band gap and also in the absence of energy migration as in that case fluorescence lifetime must show gradual increase with increasing emission wavelength. Additionally, time resolved fluorescence measurement for all three major excitations at 374nm, 445nm and 490nm show gradual decrease in lifetime with increasing emission wavelength (see Figure 6.3).

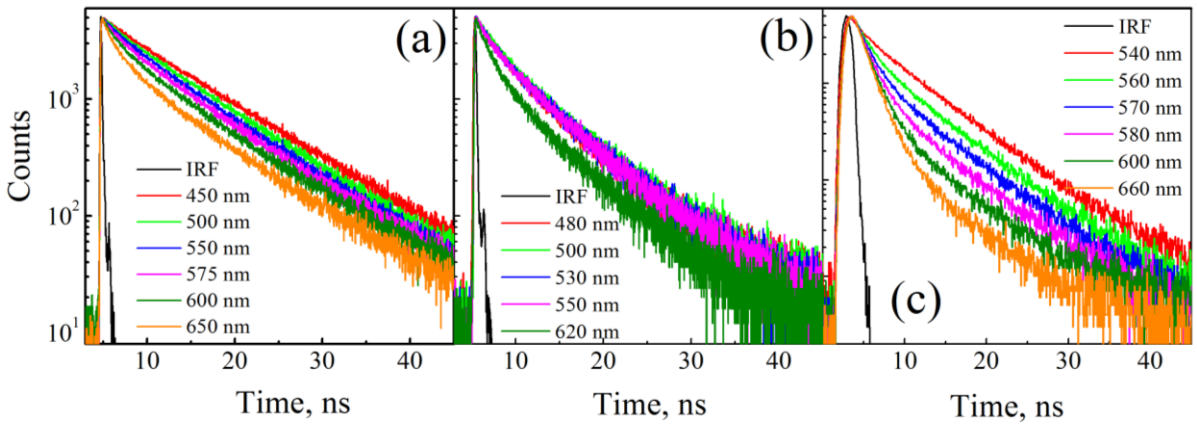

Figure 6.3: Time resolved fluorescence decay traces of CND1 in water at different emission wavelengths with excitations 374 nm (a), 445 nm (b) and 490 nm (c).

This measurement contradicts the involvement of sluggish solvent relaxation or energy migration theory[62] behind excitation dependent emission behaviour of carbon nanodots. Further,

there are several reports of CND fluorescence where single and nearly structure less emission bands is observed and these bands demonstrate shifts.[55,60,61,110,113] The possibility of in-band heterogeneity, other than the distinct ground-state heterogeneity which is clearly seen from multiple bands in absorption and emission, is also likely for CND.

In general, ground-state heterogeneity can be clearly distinguished from red edge effect (due to inhomogeneous broadening) by studying the site-selective effects in excitation and in emission.[114,115]

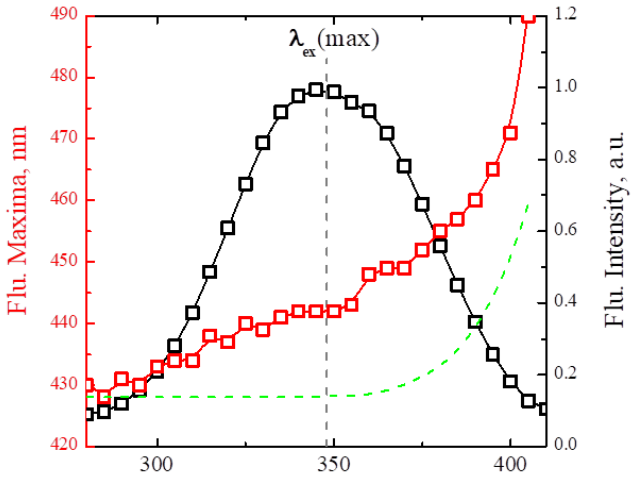

Figure 6.4: Emission maxima and peak intensity as a function of excitation wavelength for CNDs. Spectroscopic effect expected from slow solvent relaxation leading to red edge effect is schematically shown by green line (not to scale).

Red edge effect is generally expected to show characteristic shift of fluorescence spectra very distinctly above excitation wavelength maxima, λ_{ex}(max), while in-band ground state heterogeneity is expected to show shift even in the blue edge of the excitation spectra.[115] In the present case, correlations of emission intensity and emission maxima with excitation wavelength (Figure 6.4) clearly indicate the presence of in-band ground state heterogeneity.

6.3.2 Origin of fluorescence in CNDs

Over past one decade, many efforts have been undertaken to understand the origin of fluorescence in carbon nanodots. A general consensus from various reports highlights four broad possibilities. Photoluminescence (PL) in CNDs as summarized by Zhu et al.,[116] originate from (i) the conjugated π-domains of carbon core or the quantum confinement effect;[107,117,118] (ii) the functional groups connected with the carbon backbone, known as surface states;[60,119-123] (iii) the fluorescent molecules connected on the surface or interior of the CNDs, known as molecular state;[109,124-129] and (iv) the crosslink-enhanced emission (CEE) effect.[130,131] But a uniform explanation, which can address most of the PL behaviour of CNDs, is yet to emerge. Quite a few seminal reports[109,126-129,132,133] have already argued for the molecular origin of fluorescence in CNDs. Demchenko and Dekaliuk[134] have proposed based on advanced single particle measurements of Ghosh et al.,[108] that spontaneous layered stacking of chromophore during the synthesis of CND allow exciton delocalization over the whole particle leading to its characteristic polarized emission[58] by electron-hole recombination. Therefore, consideration of molecular fluorescence and their aggregation in the context of reported PL behavior of CND across the literature deserve special attention. This has further relevance in the development of tunable color materials,[58,101,106,135,136] analyte sensing,[137] etc., where CNDs are used at higher concentrations.

In this contribution, we attempt to address origin of PL and properties of multiple electronic states in CNDs, which is critically compared and verified with the experimental results reported by various other groups. For this, a new set of CNDs were synthesized by same method. Three major fractions named as CD-f1, CD-f2 and CD-f3, were separated through column chromatography based on their polarities and characterized for the present investigation.

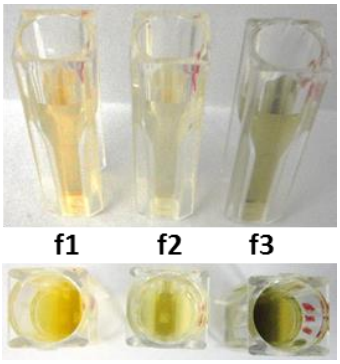

Figure 6.5: Images of CD-f1, CD-f2 and CD-f3

6.3.2.1 Characterization of all three CNDs with IR, TEM and AFM

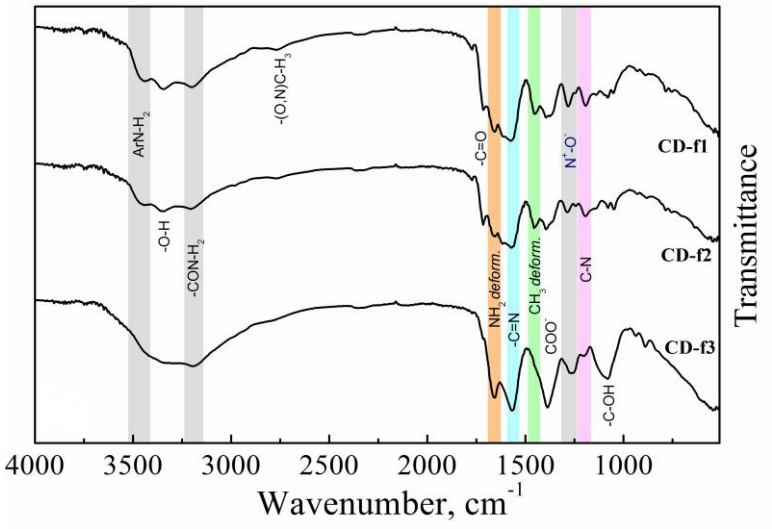

Figure 6.6: FT-IR spectrum of CNDs displaying the presence of various functional groups.

All the three CND fractions displayed characteristic IR peaks (Figure 6.6) at 1387 cm^{-1} (COO^- stretching), 1567 cm^{-1} (C=N stretching), 1192 cm^{-1} (C-N stretching), and 1717 cm^{-1} (C=O stretching) along with a broad peak at approximately around 2900-3700 cm^{-1} (with peaks at 3200, 3347 and 3452 cm^{-1} for N-H stretching of amide, O-H stretching and N-H of aromatic amines, respectively). Therefore presence of nitrogen containing pyridine, amide, amino groups

and carbonyl containing functional groups like ketone/aldehyde/carboxyl is clearly established from the FTIR spectra along with hydroxyl groups.

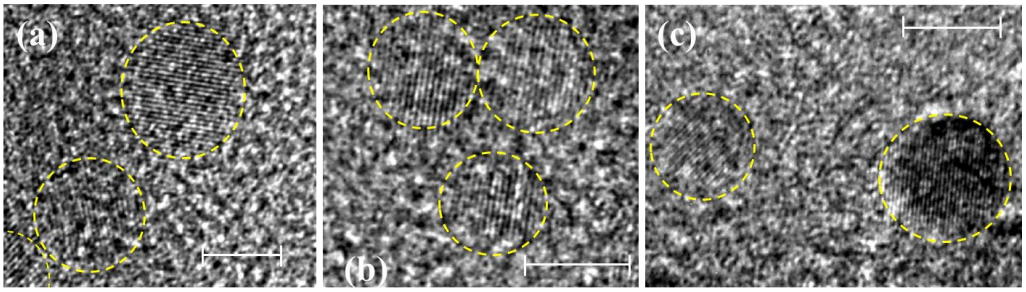

Figure 6.7: High resolution TEM images of CD-f1 (a), CD-f2 (b) and CD-f3 (c) show crystal lattice structure. Scale bar is 10 nm.

The size of the CNDs, as revealed from transmission electron microscopy (TEM) images were around 6-10 nm (Figure 6.7a-c) with a uniform height distribution as recorded with atomic force microscopy (Figure 6.8). The observed lattice spacing was around 0.26, 0.24 and 0.21 nm for the three factions.

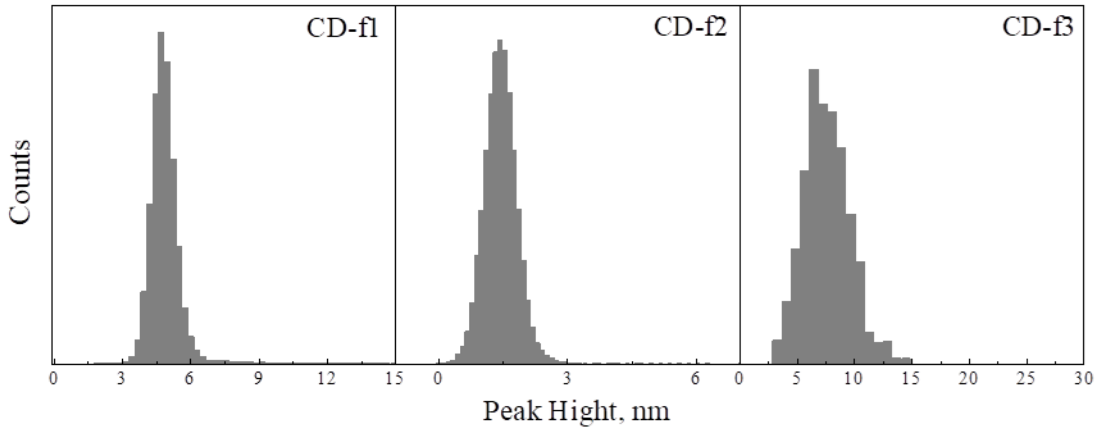

Figure 6.8: Particle height distribution of CNDs obtained from AFM measurements.

6.3.2.2 SS absorption and excitation spectra

All the three main fractions show distinct absorption band(s) in the visible wavelength range with a prominent peak around 330 to 345 nm for the n-π^* transition. As expected, this

absorption band shows gradual hypsochromic (blue) shift of ~10 nm with increase in proticity of polar protic solvents like ethanol (EtOH), methanol (MeOH) and water (Figure 6.9c).

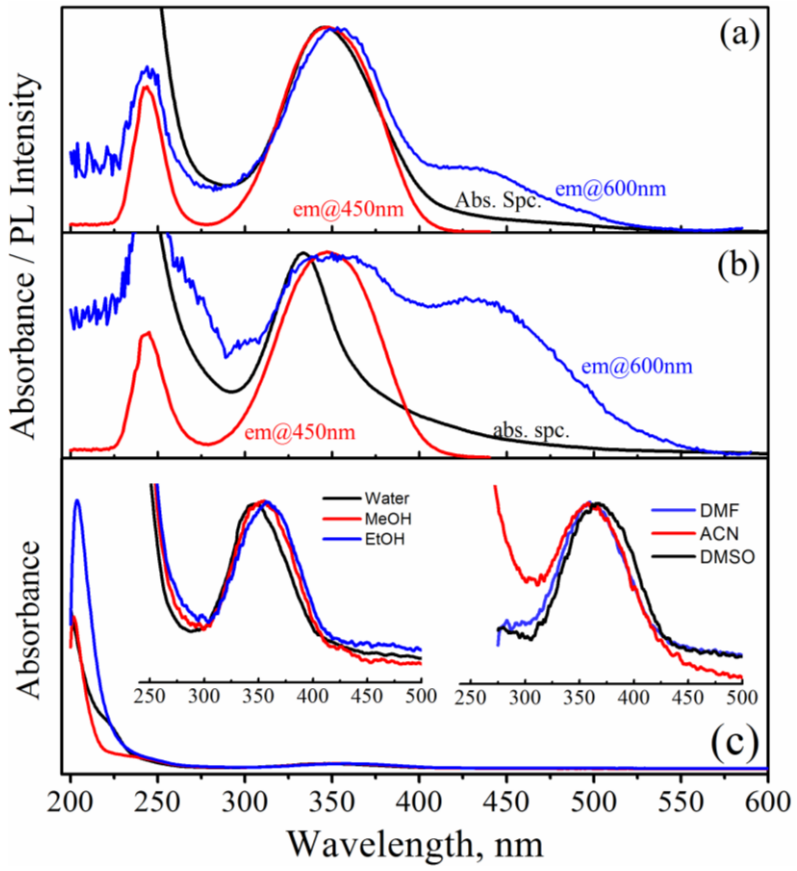

Figure 6.9: SS absorption and excitation spectra of CD-f1 (a) and CD-f3 (b) indicate multiple excitation bands. Absorption spectra of CD-f1 (c) in different polar solvents show hypsochromic and bathochromic shifts in polar protic and aprotic solvents, respectively. The concentration of CND is around 0.05 mg/ml.

On the contrary, in polar aprotic solvents, like acetonitrile (ACN), dimethylformamide (DMF) and dimethylsulphoxide (DMSO) a bathochromic (red) shift of ~ 9 nm has been observed. This observation is found similar with the other two CND fractions. The former blue-shift indicate n-π* transition (as H-bonding with solvent stabilizes the non-bonding electron pair in the ground state relative to that with the excited anti-bonding π state), while the later red-shift highlights the π-π* character for this excitation band (as the delocalized excited state is expected

to have greater energy stabilization with increased polarity). Therefore, we observe contribution from both type of transitions, π-π* and n-π*, leading to the broad absorption band at ~340 nm. Theoretical investigation of absorption spectra of oxygen-functionalised graphitic CNDs by Sudolská et al.[138] also suggested that the experimentally observed broad absorption band originate from both, n-π* and π-π* charge transfer transitions. The interlayer charge transfer transitions between different molecules or fragments with the same molecule of π-π* nature dominates over the commonly weak symmetry restricted n–π* transition.

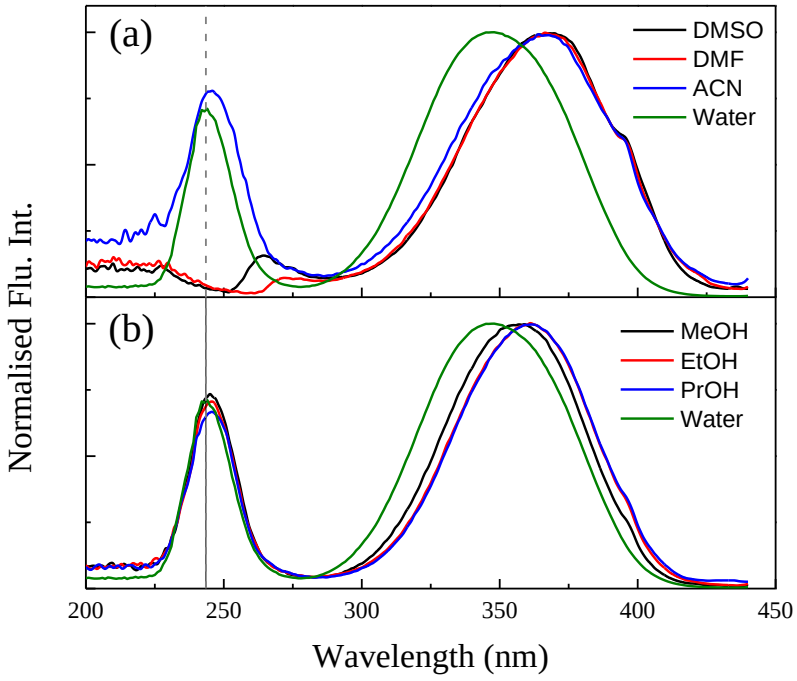

Figure 6.10: PL excitation spectra of CD-f1 in polar aprotic (a) and protic (b) solvents. The excitation spectra were not considered below 275 nm in DMSO and DMF due to solvent interference. The concentration of CND is ~0.05 mg/ml.

The recorded excitation spectra in polar protic and aprotic solvents, shown in Figure 6.10, further substantiate the above unique and distinct observation of spectral blue- and red-shift for CNDs. These results therefore contradict the general perception of exclusive n-π* transition for this band. The chromophoric groups are possibly located on the surface of CNDs – expected

from the observed solvatochromic shifts and also from the observed fluorescence quenching and concentration dependent spectral splitting, as discussed ahead.

6.3.2.3 Validity of high energy excitation band as core state of CNDs

The intense absorption band(s) in the UV region (< 300 nm) for CNDs does not lead to any significant PL emission and therefore to characterize the emissive excited states we primarily rely on the PL excitation bands. The PL excitation spectra indicate comparatively weaker excitation at ~240 nm compared to that at ~350 nm for all the fractions (Figure 6.9). It has been suggested that high energy excitation/absorption band (~240 nm) is that of core states with sp^2-hybridised carbon nanodomains of graphene like flakes embedded in a matrix comprising of sp^3-hybridised carbon with oxygen/nitrogen containing functional groups on the surface. The general accord is that the core state resulting the π-π^* transition is buried inside CND structure and is not exposed to solvent. This implies that the spectral position is independent of solvent polarity. It is to be highlighted that the UV excitation band around 240 nm demonstrate small but blue shift of ~3 nm from ethanol to water (Figure 6.10).

Therefore, spectral shift with solvent polarity confronts the shielded "core state" proposition. Similar spectral shift for this band is also reported by other groups.[139] Such observation implies that this shielded core state, if true, must be electronically well connected with the surface/edge functional groups to sample the changes in external environment. Otherwise the illustration of sp^2 hybridized carbogenic core state model for the UV excitation band in CND needs reconsideration, in absence of any inherent heterogeneity in sample.

Thus, to gain more insight in the underlying PL mechanism in CNDs, Stern-Volmer (SV) fluorescence quenching experiments were performed with iodide ions, i.e. external heavy atom effect. Fluorescence decay traces of CND in presence of KI are shown in Figure 6.11a.

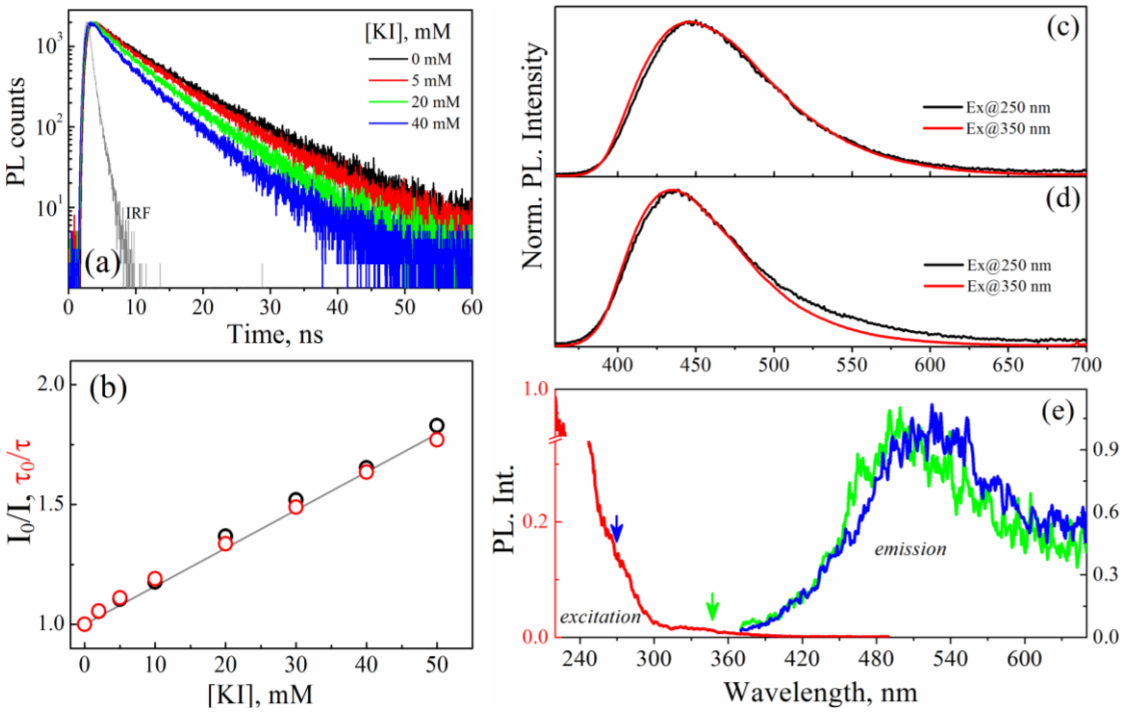

Figure 6.11: Fluorescence decay traces of CD-f1 with 267 nm excitation at different concentrations of iodide (a) indicate the accessibility of 250 nm band by external solutes. The SV plot (b) obtained from the average lifetime values show linear correlation with quencher concentration. Emission spectra of CD-f1 (c) and CD-f3 (d) with 250 and 350 nm excitations. Phosphorescence excitation and emission spectra of CD-f1 (e) recorded at 77 K. The concentration of CND is ~ 0.1 mg/ml.

Significant fluorescence quenching with 267 nm excitation (similar to 350 nm excitation) highlights the accessibility of these so called core states to external quenchers, an issue never ventured into. The estimated quenching constant from the SV plot (Figure 6.11b) is 1.8 x 10^9 $M^{-1}s^{-1}$. Spectral shift with solvent polarity and quenching of fluorescence for this high energy absorption/excitation band unambiguously highlight the inadequacy of general depiction of carbon dot "core state" transition.

Though, both 250 nm and 350 nm excitation produces similar emission spectra with a maxima around 450 nm (while the latter is strongly emissive), the involved energy levels need not necessarily be the same. A closer look at the emission spectra with 250 nm excitation reveals a distinct behavior compared to that with 350 nm excitation. The former emission spectra is slightly red shifted and relatively narrower (see Figure 6.11c,d), conceivably, a reflection of greater heterogeneity of available emissive transitions at higher wavelength excitations. The later conclusion is also supported by the above unique spectral shift with solvent polarity and reported in-band heterogeneity for the 350 nm absorption/excitation band.[129] The shorter average fluorescence lifetime of 8.4 ns for CD-f1 with 267 nm excitation than that of 9.8 ns with 374 nm excitation also highlights the presence of two distinct emissive states resulting similar emission spectra. Though we did not observe any room temperature phosphorescence, but at 77K phosphorescence spectra showed red shifted emission for lower wavelength excitation (see Figure 6.11e) similar to fluorescence emission. Additionally the measured phosphorescence decay time of 715ms at 350 nm excitation is also considerably slower (by ~ 40%) than that with the lower excitation wavelength. Based on these spectral studies we envision that the involved emissive states are not exactly the same for the 250 and 350 nm excitation. The possible involvement of higher excited state (e.g. S_2) of the same chromophoric group with 250 nm excitation or Förster resonance energy transfer from other emitters leading to near similar emission spectra is less likely in the present case.

6.3.2.4 Concentration dependent fluorescence properties

With gradual increase in concentration the main PL excitation band (for emission measurements at 450 nm) initially marginally broadened keeping the maxima unaltered. At

moderate concentrations (up to ~ 0.5 mg/ml), small spectral shift is evident along with the beginning of splitting of the main excitation band (Figure 6.12a-c).

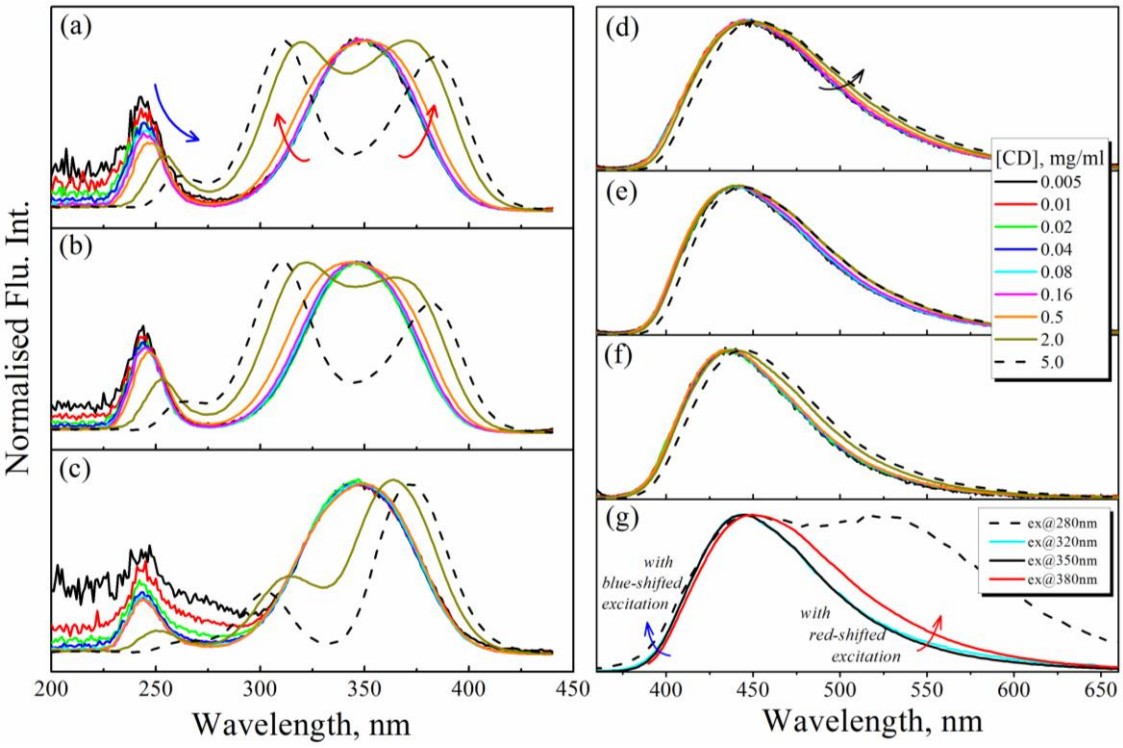

Figure 6.12: Excitation (left) and emission spectra (right) of CD-f1 (a,d), CD-f2 (b,e) and CD-f3 (c,f) at different CND concentrations. Excitation and emission spectra were recorded keeping emission and excitation wavelengths fixed at 450 nm and 350 nm, respectively. Emission spectra of CD-f3 at high concentration (g) show increased contribution from high energy emission with blue-shifted excitation, while increased low energy emission displayed with red-shifted excitation.

At comparatively high CND concentrations (>1 mg/ml), main excitation band at ~350 nm diminishes with concomitant occurrence of a high energy blue-shifted and low energy red-shifted excitation bands, albeit with altered intensity of the bands for different CND fractions. The distinct changes in spectral shape indicate the gradual formation of higher order aggregates. Surprising absence of isobestic points in the excitation spectra indicates non-equilibrium situation. Concentration dependent excitation spectra for emissions at even higher wavelengths

(i.e. at 550nm, shown in Figure 6.13) is qualitatively no different than the above except different propensity of bands across all the fractions.

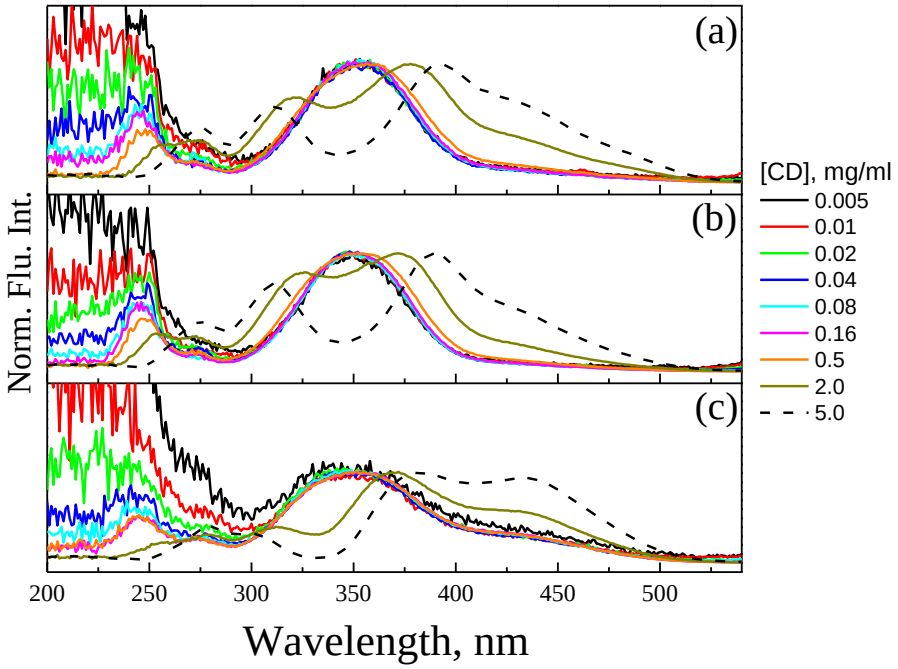

Figure 6.13: Excitation spectra of CD-f1 (a), CD-f2 (b) and CD-f3 (b) at different CD concentrations indicate aggregation induced splitting of the main excitation band. The excitation spectra were recorded keeping emission wavelengths fixed at 550 nm.

Contrary to this, the changes in emission spectra with concentration is not that dramatic, but certainly shows gradual evolution of red emissive states (leading to spectral broadening) without altering the shape on the high energy emissive side (see Figure 6.12d-f). However, at very high concentrations (≥ 5mg/ml) the whole spectra move to lower energies. Additionally the PL spectra with blue-shifted excitation reveal additional contribution from high energy emissive states compared to that at 350 nm excitation, while with the red-shifted excitation the PL spectra is noticeably red-shifted (see Figure 6.12g).

6.3.2.5 Characterization of aggregate bands

According to exciton theory of Kasha et al.,[140,141] weakly emissive H-aggregates are characterized by blue-shifted excitation/absorption band whereas for highly emissive J-aggregates, red-shifted excitation/absorption band is observed. Based on these models we may assume that the blue-shifted excitation/absorption band arises due to H-aggregates while the red-shifted band is for J-aggregates. It is quite possible that J- and H-aggregates coexists. [142-144] Observation of rod or needle shaped structure in TEM images for CNDs possibly indicate J-aggregates, although the red-shifted excitation band is not surprisingly narrowed unlike observed with other fluorophore aggregates.[136,137] Further to note, mesoscopic ribbon-like or tubular H-aggregates structure of fluorophores is also reported.[143,145] For more complex aggregate structures, simple description of pure H- and J-aggregates is inadequate to differentiate the aggregates as excitation/absorption and emission spectra displays vibronic structures. Based on the excitonic coupling strength, Spano has provided invaluable insights to distinguish between the two types of aggregates.

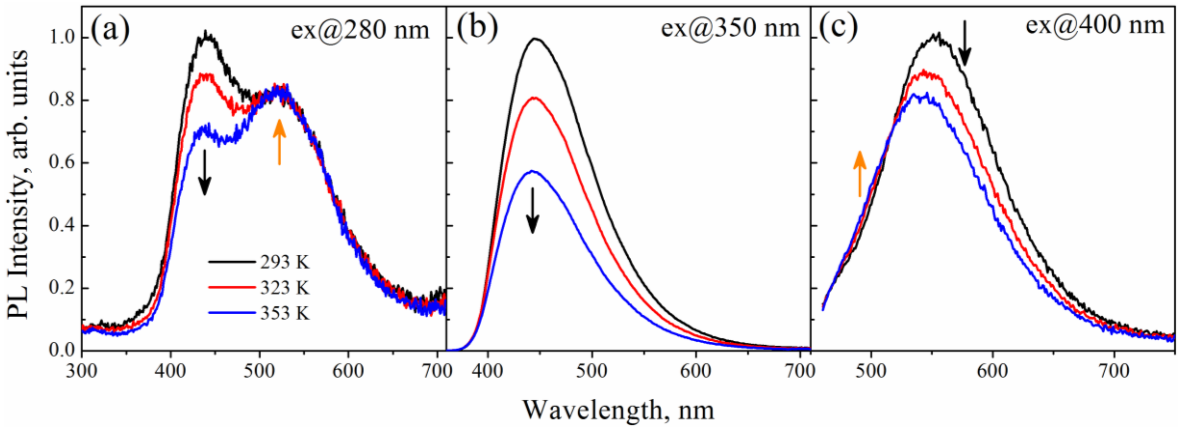

Figure 6.14: Effect of increasing temperature on the emission spectra of CD-f1 measured with different excitation wavelengths. The concentration of CND is 0.5 mg/ml.

In the present case, extending the argument of Spano[146,147] to distinguish H- and J-aggregates we recorded temperature dependent PL with excitation at blue- and red-shifted excitation maxima, shown in Figure 6.14. Either the excitations show almost unaltered or small decrease in emission intensity with temperature at the lower energy emissions, around 530 nm (Figure 6.14a,c) compared to drastic decrease at 450 nm (Figure 6.14b).

Differential temperature dependent for the low and high energy emission spectra of CND has also been reported by Gan et al.[148] In case of weakly emissive H-aggregate increase in intensity with increase in temperature is predictable, but this has to be exceedingly sufficient to overcome the strong decrease in isolated chromophore intensity due to its increase in non-radiative deactivation, even though the isolated chromophores have a small population in the blue- or red-shifted excitation wavelength. However, with red-shifted excitation, assuming it to be J-aggregate, one would expect drastic decrease in intensity with rise in temperature compared to that with isolated chromophore or monomer emission. Figure 6.14c also displays gradual increase in relative higher energy emissions with temperature, expected from H-aggregates. Thus the red-shifted excitation band does not seem to be of J-aggregates; rather we call it weakly H-aggregates. The unusual observation of low energy H-aggregate excitation is perhaps a culmination of both, weak coupling and structural distortions due to larger separation among CND particles and their non-ideal mutual spatial configuration, which relaxes selection rule for lower energy excitonic transitions, i.e. red-shifted excitation band. Radiant red-shifted excitation for weakly coupled H-aggregates has been reported for carbocyanin dyes by Berlepsch et al.[149] They have also showed that weakly coupled H-aggregates are organized in well-ordered, extended monolayer sheets, whereas the strongly coupled H-aggregates appear to consist of particles of only a few nanometers in size. Though detail structural investigation is required to

determine CND aggregates but preliminary TEM images of concentrated and matured CND samples also display sheet like structures layered one above the other, sheets with curved layers, etc. (see Figure 6.15).

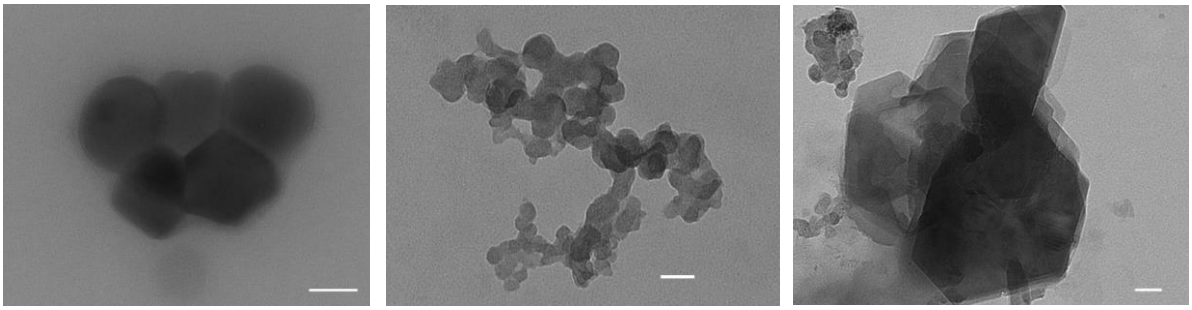

Figure 6.15: TEM images of concentrated CD-f1, CD-f2 and CD-f3 samples. Scale bar is 50 nm.

Hence, concentration and temperature dependent PL results are indicative but undeniable evidence towards aggregation, a behavior well known to many molecular fluorophores. The molecular origin of PL in CNDs is therefore further strengthened from the above solvent polarity and concentration dependent spectral changes. So, next we will discuss the presence of molecular fluorophore (if any) in CND samples.

6.3.2.6 Molecular origin of fluorescence in carbon nanodots

Formation of organic fluorophore from the reaction of citric acid with α,β-diamines and similar molecules has been reported by many groups.[126,129,132-134] Spectral similarity of citrazinic acid with CNDs has also been recently demonstrated by Schneider et al.[129] Demchenko and Dekaliuk[134] have further proposed that spontaneous layered stacking of chromophore during the synthesis of CND allow exciton delocalization over the whole particle leading to its characteristic polarized emission[58] by electron-hole recombination. Such proposed H-aggregate structure of CND also prompts explanation for the observed large stokes shift. Concentration

dependent excitation spectra experimentally proves the presence of CND aggregates even in moderate to low concentration regimes (<0.5 mg/ml), resulting in the excitation dependent PL in CND samples (discussed above).

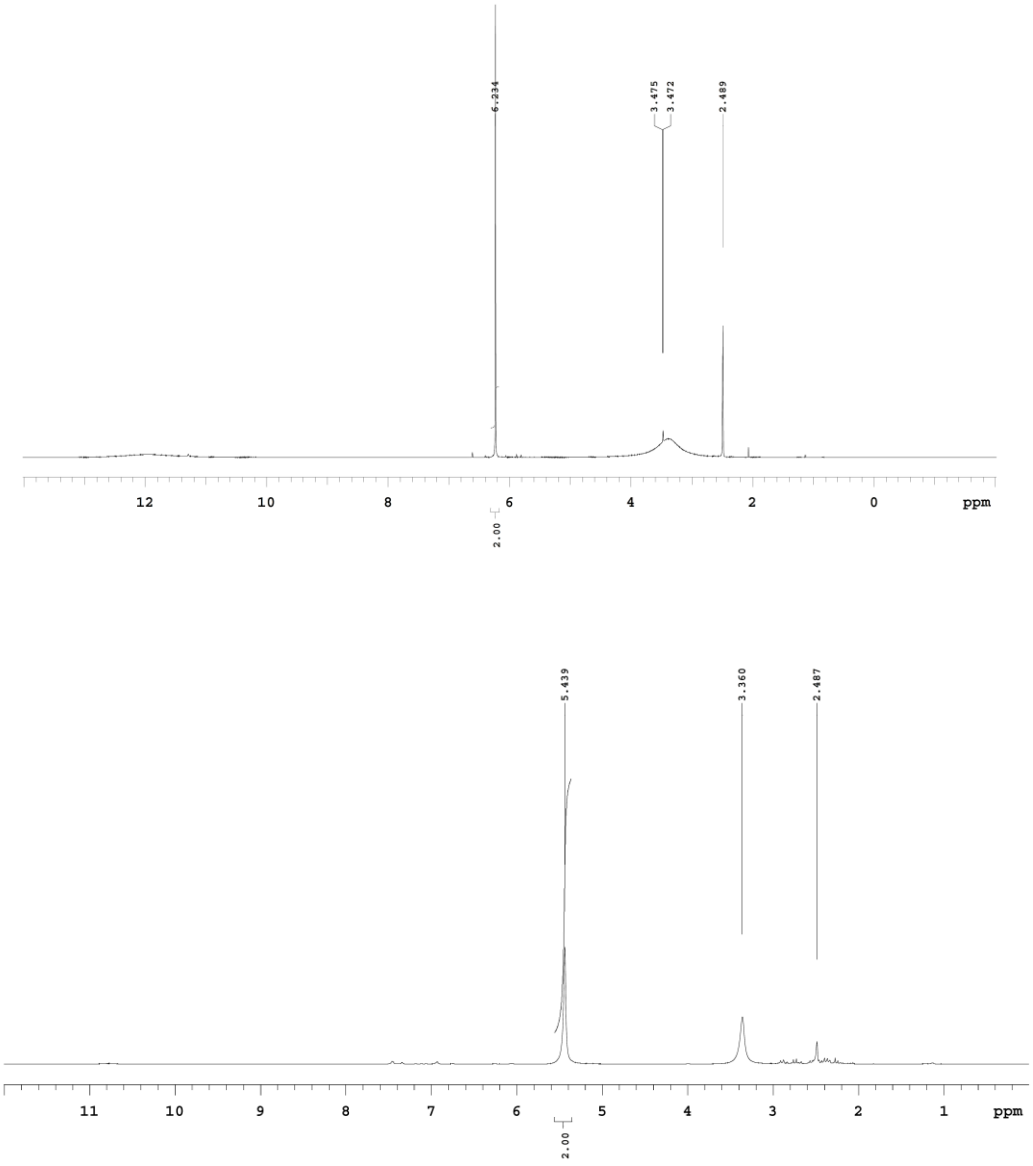

Figure 6.16: NMR spectra of CzA (top) and CD-f1 in DMSO-d6.

Molecular emissive state in citric acid derived CNDs in addition to emissions from the carbon core and multiple surface states has also been reported by Dhenadhayalan et al.[127] and Krysmann et al.[109] So, we further extended spectroscopic investigations with citrazinic acid (CzA) to substantiate the signature of molecular chromophores in CNDs. Close resemblance of NMR spectra of CND with that of CzA (Figure 6.16) also supports their argument.

It is very interesting to note that within the linear concentration vs. absorbance regime there is blue shift for the 350 nm band along with decrease in the visible tail band (Figure 6.17). The latter observation is similar with CNDs although the main absorption band does not show shift. But surprisingly the CzA excitation spectra display the beginning of spectral splitting (*cf.* Figure 6.17 inset), an observation similar to CNDs.

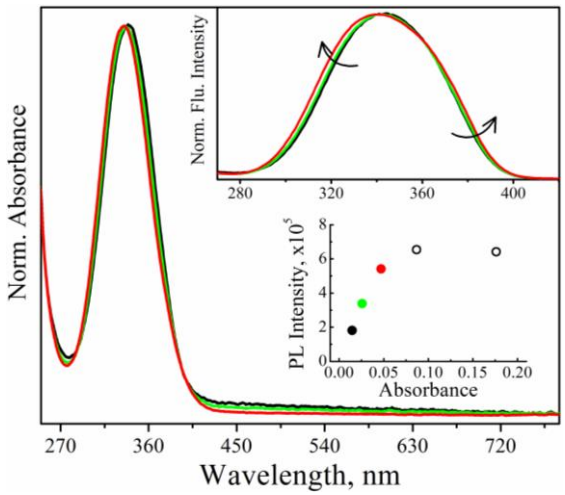

Figure 6.17: Absorption spectra of CzA at different concentrations indicated by the colors in the absorbance vs. PL intensity plot in the inset. Corresponding excitation spectra shows broadening with increase in CzA concentration.

A closer inspection of the absorption spectra also indicates the presence of additional band in the 370-410 nm regions at high CzA concentration, similar to its excitation spectra. Further, the recorded absorption spectra in different polar solvents (see Figure 6.18) illustrate

bathochromic shift for polar aprotic solvent while hypsochromic shift is witnessed in polar protic solvents.

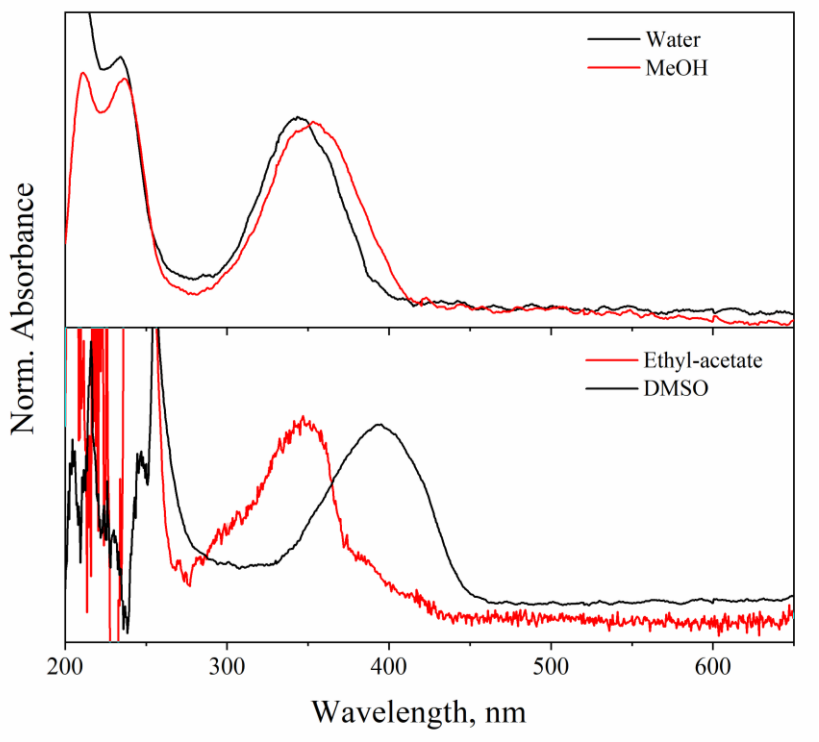

Figure 6.18: Absorption spectra of CzA in polar protic and aprotic solvents.

Therefore, though CNDs are much complex and larger system, their spectral features bear a close resemblance to CzA. On the other hand, comparison of lifetime decays (see Figure 6.19c) discerns complex and altered photophysics in CNDs than basic CzA unit. It is important to mention here that this molecular state, as described by Choi et al,[150] is different from the edge state, which is related to the boundary between sp^2- and sp^3-hybridized carbon and the surface exposed functional groups, although they undergo similar n-π^* transition with a similar energy gap. Further, reaction temperature in hydrothermal synthesis imparts influence on the extent of carbonization and the formation of fluorophore units in CND samples.[109,129,151-153] Zhang et al.[153] has shown that formation of carbon dots starts at or above 180^0 C from the carbonization of

fluorescent polymer chains generated by the condensation of initially produced small fluorescent molecules.

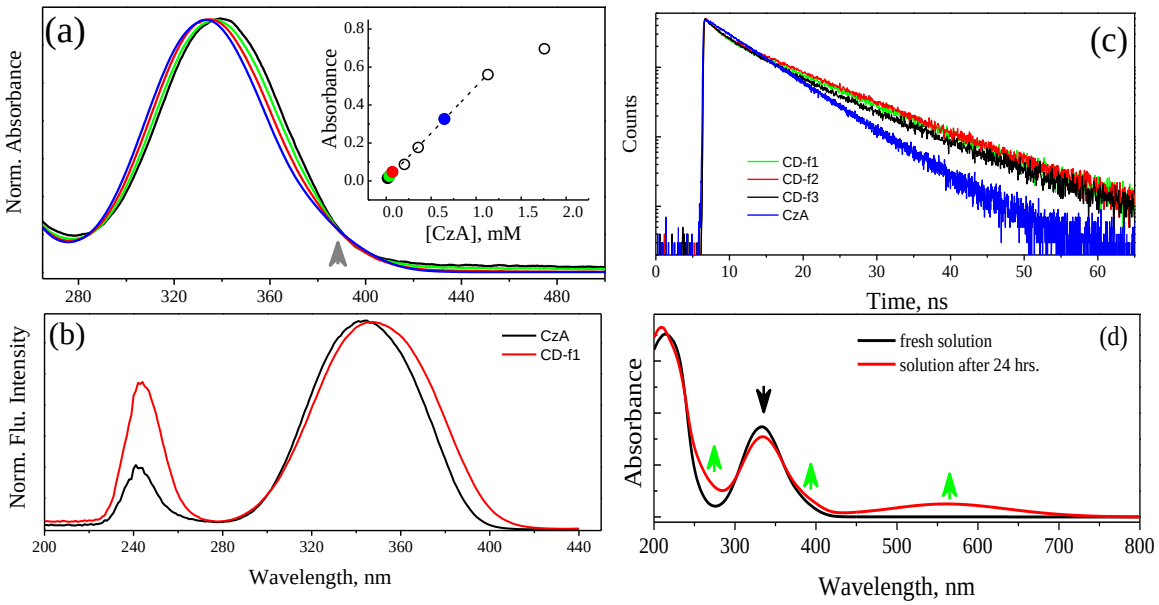

Figure 6.19: Absorption spectra with increase in concentration of CzA (a) indicate the presence of a small band in the 370-410 nm region. Inset shows the linear range of concentration vs. absorbance plot. Similarity between CD-f1 and CzA excitation spectra (b) corroborates the molecular origin for the 240 nm excitation band. However, lifetime measurements with 374 nm excitation (c) discern the complex PL behaviour in CNDs than CzA. Changes in absorbance spectra of concentrated CzA solution (d) indicates evolution of high and low energy bands with time.

Though quantum yield exhibits significant change, the general spectral features of CNDs prepared at different reaction temperature are quite similar, especially excitation dependent emission behavior.[109,151-153] Spectroscopic investigations of our CND samples prepared at different temperatures also substantiate the above observations.

However, In spite of emphasizing on the molecular origin for PL in CND sample, in absence of direct measurements like fluorescence correlation spectroscopy (FCS), it is very challenging to identify the luminescence moiety as free molecular fluorophore or chromophore embedded CND particles. Though it is debatable whether molecular fluorophores are embedded

into carbonized nanoparticles (CNDs) or otherwise,[154] recent fluorescence correlation spectroscopy (FCS) results by Righetto et al.[155] clearly prove that the main excitation-emission band is exclusively due to small molecule like species, as was earlier pointed out by Krysmann et al.[109] and later isolated by Song et al.[126,156] So we have also recorded FCS curves for our CND sample (CD-f2) samples in water with 405 nm excitation wavelength (see Figure 6.20), which reiterates diffusion of sub-nanometer molecular species similar to coumarin 503 (C503). Hence, in view of the exclusive FCS results by Righetto et al.[155] and the present one, earlier mentioned concentration dependent broadening of excitation spectra and splitting at very high concentrations along with other molecular aspects of PL is also certainly attributed to aggregation of these free molecular species similar to other fluorophores, without emphasizing on the self-assembly of CND particles. In fact, the observed very fast rotational depolarization than expected from particles of over nanometer dimension[58] can also be realized from these FCS results – an acknowledgement to the presence of small and free fluorophore moieties.

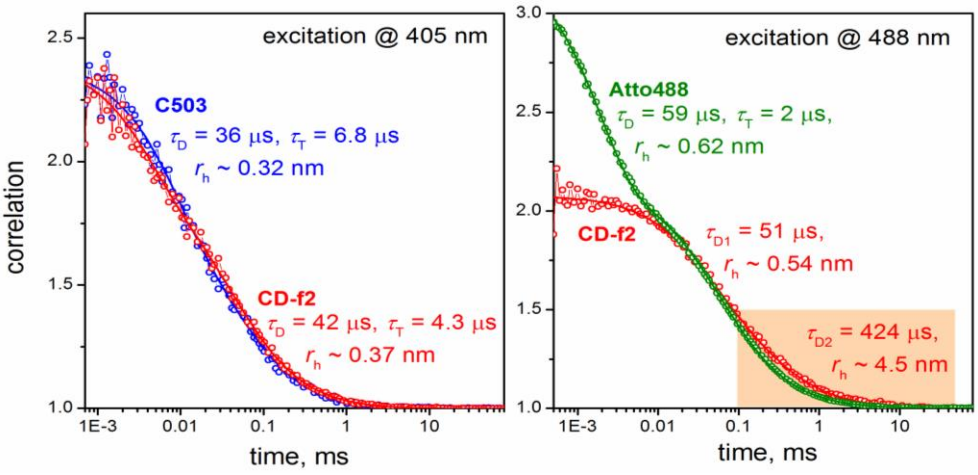

Figure 6.20: FCS curves with three dimensional diffusion fits (smooth lines) for C503 (blue), Atto488 (green) and CD-f2 (red) in water. FCS curve for CD-f2 with 488 nm excitation was best fitted with two diffusion times (τ_d). Diffusion coefficients for standard dyes C503 and Atto488 are 6.72 x10^{-10} m^2s^{-1} and 4.0 x10^{-10} m^2s^{-1}. Overall results are also similar for other CND fractions.

Additionally, excitation wavelength resolved FCS measurements also hints at the presence of larger hydrodynamic radii particles at excitation wavelengths over 440 nm, which is consistent with the dimensions of CNDs found from transmission electron microscopy (TEM) measurements. Following their results we also recorded FCS curves with 488 nm excitation, as shown in Figure 6.20. Presence of slow diffusing species with hydrodynamic radius (r_h) of 4.5 nm (~23%), similar to earlier TEM results, further reaffirms presence of emissive CND particles. However, even with 488 nm excitation, PL contribution from sub-nanometer species is quite significant in our CND sample. Righetto et al.[155] further argued from time-resolved electron paramagnetic resonance (TREPR) measurements that carbon sp^2 domains are embedded within carbon sp^3 scaffolds of carbon cores. Single particle imaging and nano-cavity based quantum yield measurements with similar excitation wavelengths by Ghosh et al.[108] have conclusively demonstrated bright emission from single CND particles and their estimated hydrodynamic dimensions match high-resolution TEM and atomic force microscopy (AFM) results, besides unique structural insight of CNDs and its correlation with observed PL. Further stability against photobleaching for this longer wavelength emission has been attributed to the protection offered by carbon matrix to the incorporated chromophore by Xiong et al.[154] These reports suggest that the higher wavelength excitation/emission is predominantly due to CND particles and PL results nicely corroborate with TEM measurements.

Internal structure of carbogenic CND particles received minute attention except regular lattice spacing of around 0.22 nm analogous to graphite. However, such regular crystal lattice structure under electron microscopy is also probable due to molecular aggregates. So whether the observed nanometer sized particles with regular lattice structure in electron micrographs are due to aggregates of molecular species (induced by drying on TEM grids)[157] or is due to true CND

particles? Here we further explored the structure of CND particles for insight of their formation from these molecular precursors and its resemblance with other reported naturally occurring or man-made carbon particles. Insight of CND particles and its comparative assessment with spherical carbon soots and carbonaceous particles is highly imperative; especially in the context of designing CND particles with improved PL and other characteristics as luminescent probe or marker for use with visible excitation wavelengths.

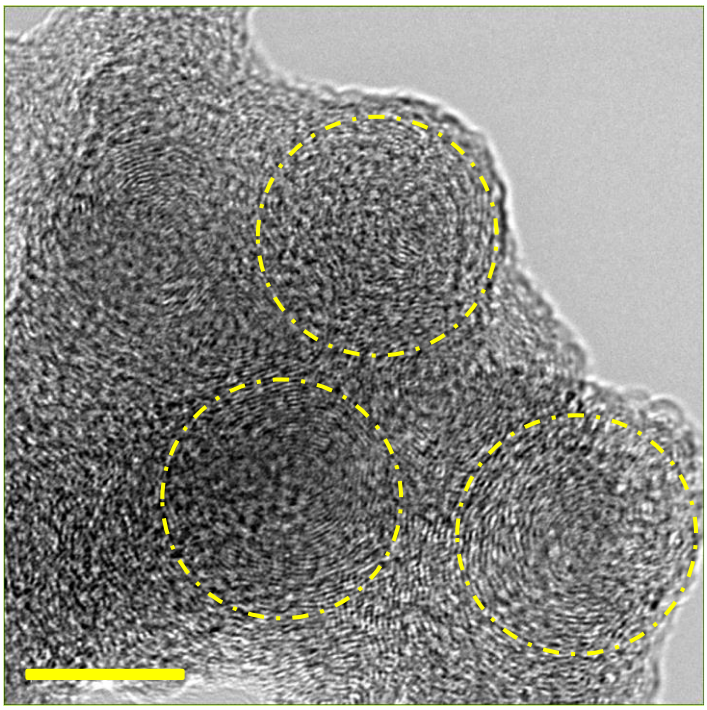

Figure 6.21: TEM images of CND agglomerates of spherical particles. Yellow circles represents the approximate size of spherical CND. Scale bar is 10 nm.

So we recorded high resolution TEM images for the CD-f2 sample (Figure 6.21). We observed that other than regular crystal lattices spherical particles are also present in the CND sample. It also reveal an array of agglomerate structures with hundreds of spherical primary particles, which we generally avoid considering in our analysis (see Figure 6.15). A closer

inspection of these spherical primary structures reveal striking morphology of curved lattice arrangement with occasional not so defined boundaries, shown in Figure 6.21.

Concentric nanostructures confirm that these particles were formed during high temperature synthesis from organic materials. To be noted, similar CND structures were earlier reported by Ghosh et al.[108] and were also identified in fluorescence confocal images. Recently, similar structure was also reported by Li et al.[158] for graphene quantum dots under highly acidic conditions. Additionally, these structures are very commonly encountered with carbon soot aggregates – irrespective of their origin from combustion of wood, diesel engine emission or dark pigments layers covering speleothems.[159-162] So, following the depiction of carbon soot particles by Heidenreich et al.,[163] we schematically represent the internal structure of CND in Figure 6.22.

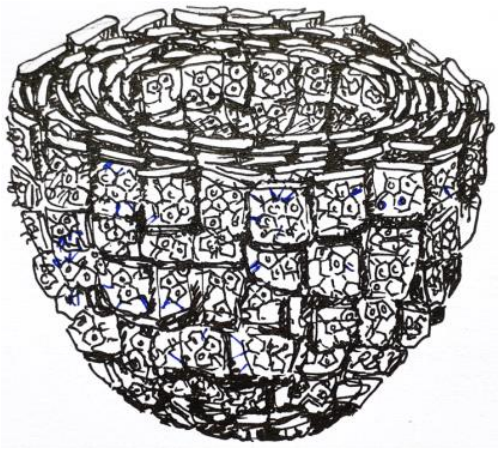

Figure 6.22: Internal structure of spherical primary particles in CND agglomerates

So, we conclude that primary heterogeneity in CND sample, responsible for its fascinating PL behavior, is due to the presence of both molecular fluorophores and CND particles, compounded with the abundance of functional groups, size and structural

distribution.[108,109,155,164,165] Observed composite spectral behavior for CNDs is additionally complex due to the possibility of self-assembly of these emissive units and alteration of involved electronic states. The huge excitation dependent emission spectral shift in CND samples, which apparently challenges the classical Kasha-Vavilov rule, is primarily due to the involvement of multiple electronic states arising from heterogeneity in samples.

6.3.3 Interaction of CNDs with Uranyl ion (UO_2^{2+})

In order to explore the tendency of fluorescent carbon nanodots to sense heavy metal ions with single molecule sensitivity, we studied interaction of CNDs with Uranyl ion. The CNDs here used were synthesized under highly oxidative environment via same procedure. Obtained CNDs were then purified using column chromatography and the red emissive portion of CNDs were collected as it is evident from earlier studies that blue emissive CNDs contains mostly molecular entities. But the fluorescence quantum yield of this CND sample is found very low (<5 %). This lower quantum yield along with huge ground state heterogeneity in the sample, highly affected the quality of FCS data.

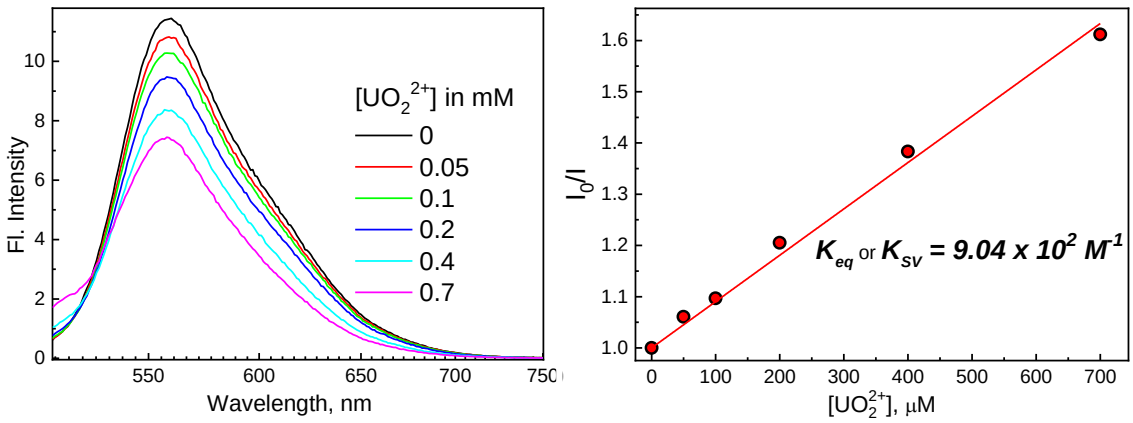

Figure 6.23: SS emission spectra of CND for excitation at 550nm at different concentration of uranyl ion (left). SS Stern Volmer plot for quenching (right).

So we recorded SS emission spectra to study their interactions with uranyl ion. The obtained SV plot shows linear variation with quencher concentration indicating 1:1 ground state interaction of CND with uranyl ion. However, the observed SV constant or ground state equilibrium constant was found to be very low (= 904 M^{-1}). It implies that our newly synthesized CNDs are not very sensitive towards metal ion complexation like Calcein. Thus performing experiments with highly radioactive metals like americium ions near its disposable limit is not possible even with single molecule sensitive measurements. Thus, a lot or synthetic research is still required to practically use these materials for various analytical measurements with both single molecule and ensemble spectroscopy methods.

6.4 Conclusion

In summary, the origin of excitation and emission bands is considerably complex and heterogeneous than the simple interpretations prevalent in literature. We have shown simple but definite evidence that directly contradicts the general core state proposition. Apart from the demonstration of heterogeneity for the edge band, our experiments also recognize presence of molecular fluorophore by FCS measurements and aggregation induced spectral splitting like molecular fluorophore for CNDs. Though additional evidences are required to exactly explain the titillating PL behavior of CNDs at high concentrations, but based on the temperature dependent PL studies we tentatively argue for the simultaneous presence of weak and strong H-aggregates. Our investigation also reveals the possibility of different origin of near similar emission spectra for the 250 and 350 nm band excitation. Further, we have also potentially verified the presence of CND particles with HR-TEM and FCS measurements. In addition to that, we have also studied the potential of CNDs towards sensing metal ions. However, lots of

development in their synthesis, purification and passivation processes with improved quantum yield is required to make them efficient for this particular application.

We believe that, these highly significant and new results will certainly instigate researchers to reassess the PL behavior of carbon dots, an essential not only for fundamental understanding but also for various applications from bio-imaging to white light materials. Though CNDs has been used in various super-resolution imaging techniques like, stimulated emission depletion (STED),[166] super-resolution optical fluctuation imaging (SOFI)[103] and localization-based super-resolution microscopy,[167] the dearth of clarity in several issues starting from synthesis of vast CND samples to systematic investigation for the origin of complex fluorescence behavior actually limits its wide applicability. Moreover, CNDs can also be potentially employed in sub-diffraction resolution imaging with super resolution by polarization demodulation (SPoD),[168] as it displays anisotropic PL from the electric diploe of CNDs established by scanning of azimuthally polarized laser beam (APLB) at focal region.[108] Although different imaging techniques exploit various parameters of CND as fluorescent marker (i.e. photo-stability, blinking, polarization, etc.), the trickiest of them is to have excitation independent emission (detrimental in selecting/designing donor-acceptor pairs for energy transfer experiments). Although a general consensus for the control of PL mechanism is yet to emerge but primarily linked to surface passivation and homogeneous surface/molecular states structure. Recently, several studies have come up with excitation independent (or very weakly dependent) CND samples either by engineering reaction schemes[110,128,169-174] or by suitable functionalization[175] or doping of CNDs,[176] signifying a brighter prospect of CND as a non-expensive, stable and bio-compatible marker.

APPENDIX

A1. Global fitting of SS SV and antibunching data using 1:1 ground state complexation model for A655-Trp interactions

Considering only a 1:1 ground state complex formation, without any additional excited state quenching other than dynamic interaction, the reaction model can be shown as

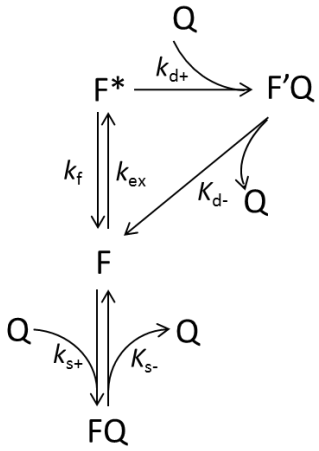

Figure A1.1: Schematic diagram of A655-Trp quenching

Solving this model for I_0/I with steady state approximation, we get a second order polynomial of q, given by

$$\frac{I_0}{I(q)} = 1 + aq + bq^2 \tag{A1.1}$$

Here a and b are the constant coefficients of the polynomial, given by

$$a = \frac{k_{d-}k_{d+}k_{s-} + k_{d+}k_{ex}k_{s-} + k_{d-}k_f k_{s+}}{k_{d-}k_{ex}k_{s-} + k_{d-}k_f k_{s-}} \tag{A1.2}$$

$$b = \frac{k_{s+}}{k_{s-}} \frac{k_{d+}}{k_{ex} + k_f} \tag{A1.3}$$

Rearrangement of these equations gives solutions for k_{d-} and k_{s-} as follow

$$k_{d-} = -\frac{{k_{d+}}^2 k_{ex}}{{k_{d+}}^2 - a k_{d+}(k_{ex} + k_f) + b k_f (k_{ex} + k_f)} \tag{A1.4}$$

$$k_{s-} = \frac{k_{d+} k_{s+}}{b(k_{ex} + k_f)} \tag{A1.5}$$

The values for 'a' and 'b' were calculated from the second order polynomial fit of SS SV plot (Figure A1.2) which comes out to be a = 20.5 M^{-1} and b = 7780 M^{-2} (though third order polynomial in q give better fit). The values of k_f and k_{d+} can be calculated from TCSPC data, and k_{ex} can be calculated from antibunching analysis of A655 at zero quencher concentration. When substituting all of these known parameters into eq. (A1.4), one obtains a negative value for k_{d-} (i.e. -3.39 x 10^5), which is unphysical. This clearly indicates the necessity of using even a more complex kinetic scheme than displayed in Figure A1.1.

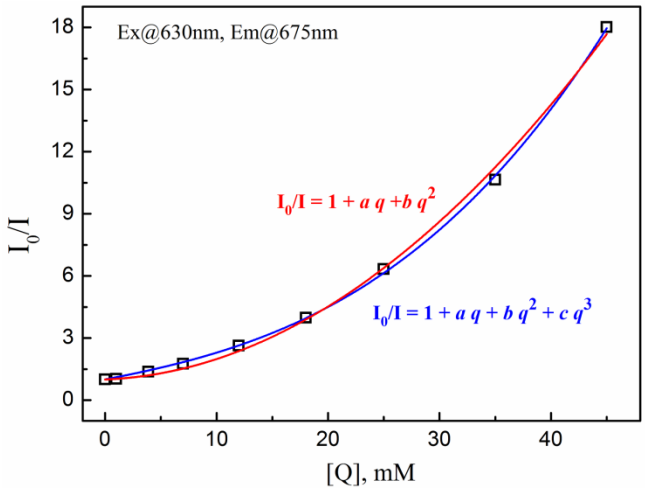

FigureA1.2: SS SV plot fitted with second and third order polynomial function in q.

A2. Kinetics of bimolecular interactions

Let us consider a bimolecular reaction between A and B

$$A + B \underset{k_b}{\overset{k_f}{\rightleftharpoons}} AB$$

The rate of reaction is given by

$$\frac{dA}{dt} = -k_f[A][B] + k_b[AB] \tag{A2.1}$$

Now for any instantaneous time t, [*AB*] is given by

$$[AB] = [A_0] - [A] \tag{A2.2}$$

and

$$[B] = [B_0] - [AB] = [B_0] - [A_0] + [A] \tag{A2.3}$$

Substituting these values of [*AB*] and [*B*] in eq. (A2.1) we get

$$\frac{dA}{dt} = -k_f[A]^2 - (k_f[B_0] - k_f[A_0] + k_b)[A] + k_b[A_0] \tag{A2.4}$$

This equation can be written in a simplified form as

$$\frac{dA}{dt} = a[A]^2 + b[A] + c \tag{A2.5}$$

where

$$a = -k_f \tag{A2.6}$$

$$b = -(k_f[B_0] - k_f[A_0] + k_b) \tag{A2.7}$$

$$c = k_b[A_0] \tag{A2.8}$$

Now, rearranging the eq. (A2.5) we get

$$\frac{dA}{a[A]^2 + b[A] + c} = dt \tag{A2.9}$$

or
$$\frac{dA}{[A]^2+\frac{b}{a}[A]+\frac{c}{a}} = a.dt \qquad \text{(A2.10)}$$

Denominator of eq. (A2.10) can be factorized as

$$\frac{dA}{(A-x_1)(A-x_2)} = a.dt \qquad \text{(A2.11)}$$

where
$$x_1 = \frac{-b+\sqrt{b^2-4ac}}{2a}; \quad x_2 = \frac{-b-\sqrt{b^2-4ac}}{2a} \qquad \text{(A2.12)}$$

Rearranging eq. (A2.11), we get

$$\frac{1}{(x_1-x_2)}\left(\frac{1}{(A-x_1)}-\frac{1}{(A-x_2)}\right)dA = a.dt \qquad \text{(A2.13)}$$

Now, in order to get an expression for A as a function of t, we can integrate eq. (A2.13) under specified limits i.e.

$$\frac{1}{(x_1-x_2)}\int_{A_0}^{A}\left(\frac{1}{(A-x_1)}-\frac{1}{(A-x_2)}\right)dA = a\int_0^t dt \qquad \text{(A2.14)}$$

Which given us

$$\ln\left[\frac{(A-x_1)}{(A-x_2)}\frac{(A_0-x_2)}{(A_0-x_1)}\right] = a.t(x_1-x_2) \qquad \text{(A2.15)}$$

or
$$\frac{(A-x_1)}{(A-x_2)} = \frac{(A_0-x_1)}{(A_0-x_2)}e^{at(x_1-x_2)} \qquad \text{(A2.16)}$$

Now, let us consider

$$\frac{(A_0-x_1)}{(A_0-x_2)}e^{at(x_1-x_2)} = c \qquad \text{(A2.17)}$$

$\therefore$ eq. (A2.17) now

becomes

$$(A - x_1) = c(A - x_2) \tag{A2.18}$$

$\therefore$

$$A = \frac{x_1 - x_2 c}{1 - c} \tag{A2.19}$$

Substituting value of c from eq. (17) into eq. (19), we get

$$A = \frac{x_1 - x_2 \dfrac{(A_0 - x_1)}{(A_0 - x_2)} e^{at(x_1 - x_2)}}{1 - \dfrac{(A_0 - x_1)}{(A_0 - x_2)} e^{at(x_1 - x_2)}} \tag{A2.20}$$

This gives us the required expression for A as a function of t.

REFERENCES

(1) Kumar, A.; Alia, M.; Ningthoujam, R. S.; Gaikwad, P.; Kumar, M.; Nath, B. B.; Pandey, B. N. *J. Hazardous Mat.* **2016**, *307*, 281.

(2) Bauer, N.; Fröhlich, D. R.; Panak, P. J. *Dalton Trans.* **2014**, *43*, 6689.

(3) Sturzbecher-Hoehne, M.; Goujon, C.; Deblonde, G. J.-P.; Mason, A. B.; Abergel, R. J. *J. Am. Chem. Soc.* **2013**, *135*, 2676.

(4) Deblonde, G. J.-P.; Sturzbecher-Hoehne, M.; Mason, A. B.; Abergel, R. J. *Metallomics* **2013**, *5*, 619.

(5) Jensen, M. P.; Rickert, P. G.; Gorman-Lewis, D.; Seifert, S.; Aryal, B.; Lai, B.; Woloschak, G. E.; Paunesku, T.; Soderholm, L. *Nat. Chem. Biol.* **2011**, *7*, 560.

(6) Maloubier, M.; Michel, H.; Solari, P. L.; Moisy, P.; Tribalat, M.-A.; Oberhaensli, F. R.; Bottein, M. Y. D.; Thomas, O. P.; Monfort, M.; Moulin, C.; al., e. *Dalton Trans.* **2015**, *44*, 20584.

(7) Mohapatra, P. K.; Sengupta, A.; Iqbal, M.; Huskens, J.; Verboom, W. *Chem. Eur. J.* **2013**, *19*, 3230.

(8) Bhattacharyya, A.; Kim, E.; Weck, P. F.; Forster, P. M.; Czerwinski, K. R. *Inorg. Chem.* **2013**, *52*, 761.

(9) Miguirditchian, M.; Guillaneux, D.; François, N.; Airvault, S.; Ducros, S.; Thauvin, D.; Madic, C.; Illemassène, M.; Lagarde, G.; Krupa, J.-C. *Nuclear Sci. & Eng.* **2006**, *153*, 223.

(10) Geipel, G.; Acker, M.; Vulpius, D.; Bernhard, G.; Nitsche, H.; Fanghänel, T. *Spectrochimia Acta A* **2004**, *60*, 417.

(11) Lakowicz, J. R. *Principles of Fluorescence Spectroscopy*; 3rd ed.; Spinger: New York, USA, 2006.

(12) Grossmann, K.; Arnold, T.; Ikeda-Ohno, A.; Steudtner, R.; Geipel, G.; Bernhard, G. *Spectrochimica Acta Part A* **2009**, *72*, 449.

(13) Valenzuela, R. W.; Brundage, R. T. *J. Chem. Phys.* **1990**, *93*, 8469.

(14) Conway, J. G.; Wallmann, J. C.; Cunningham, B. B.; Shalimoff, G. V. *J. Chem. Phys.* **1957**, *27*, 1461.

(15) Gmar, M.; Capdevila, J. M. *Nuclear Instruments and Methods in Physics Research Section A: Accelerators, Spectrometers, Detectors and Associated Equipment* **1999**, *422*, 841.

(16) Valeur, B. *Molecular Fluorescence: Principles and Applications*; Wiley-VCH Verlag GmbH: Weinheim, Germany, 2001.

(17) Marmé, N.; Knemeyer, J.-P.; Sauer, M.; Wolfrum, J. *Bioconjugate Chem.* **2003**, *14*.

(18) Vaiana, A. C.; Neuweiler, H.; Schulz, A.; Wolfrum, J. r.; Sauer, M.; Smith, J. C. *J. Am. Chem. Soc.* **2003**, *125*, 14564.

(19) Doose, S.; Neuweiler, H.; Sauer, M. *ChemPhysChem* **2005**, *6*, 2277.

(20) Brox, D.; Kiel, A.; Wörner, S. J.; Pernpointner, M.; Comba, P.; Martin, B.; Herten, D.-P. *PLOS One* **2013**, *8*, e58049 (7).

(21) Zhang, Y.; Yuan, S.; Lu, R.; Yu, A. *J. Phys. Chem. B* **2013**, *117*, 7308.

(22) Bhattacharjee, U.; Beck, C.; Winter, A.; Wells, C.; Petrich, J. W. *J. Phys. Chem. B* **2014**, *118*, 8471.

(23) Sayed, M.; Pal, H. *Phys. Chem. Chem. Phys.* **2015**, *17*, 9519.

(24) Carter, K. P.; Young, A. M.; Palmer, A. E. *Chemical Reviews* **2014**, *114*, 4564.

(25) Pollnau, M.; Hardman, P. J.; Clarkson, W. A.; Hanna, D. C. *Optics Communications* **1998**, *147*, 203.

(26) Marme´, N.; Habl, G.; Knemeyer, J.-P. *Chem. Phys. Lett.* **2005**, *408* 221.

(27) Magde, D.; Elson, E. L.; Webb, W. W. *Phys. Rev. Lett.* **1972**, *29*, 705.

(28) Elson, E. L. *Biophys. J.* **2011**, *101*, 2855.

(29) Haustein, E.; Schwille, P. *Annu. Rev. Biophys. Biomol. Struct.* **2007**, *36*, 151.

(30) Kumbhakar, M.; Nath, S.; Mukherjee, T.; Mittal, J. P.; Pal, H. *J. Photochem. Photobiol. C* **2004**, *5*, 113.

(31) Ehrenberg, M.; Rigler, R. *Chem. Phys.* **1974**, *4*, 390.

(32) Kask, P.; Piksarv, P.; Mets, Ü. *Eur. Biophys. J.* **1985**, *12*, 163.

(33) Doose, S.; Neuweiler, H.; Sauer, M. *ChemPhysChem* **2009**, *10*, 1389.

(34) Yin, Y.; Zhao, X. S. *Acc. Chem. Res.* **2011** *44*, 1172.

(35) Kumbhakar, M.; Singh, P. K.; Satpati, A. K.; Nath, S.; Pal, H. *J. Phys. Chem. B* **2010**, *114*, 10057.

(36) Schwille, P.; Kummer, S.; Heikal, A. A.; Moerner, W. E.; Webb, W. W. *Proc. Natl. Am. Soc.* **2000**, *97*, 151.

(37) Al-Soufi, W.; Reija, B.; Novo, M.; Felekyan, S.; Kühnemuth, R.; Seidel, C. A. M. *J. Am. Chem. Soc.* **2005**, *127*, 8775.

(38) Kim, J.; Doose, S.; Neuweiler, H.; Sauer, M. *Nucleic Acids Res.* **2006**, *34*, 2516.

(39) Al-Soufi, W.; Reija, B.; Felekyan, S.; Seidel, C. A. M.; Novo, M. *ChemPhysChem* **2008**, *9*, 1819.

(40) Novo, M.; Granadero, D.; Bordello, J.; Al-Soufi, W. *J. Incl. Phenom. Macrocycl. Chem.* **2011**, *70*, 259.

(41) Doose, S.; Neuweiler, H.; Sauer, M. *ChemPhysChem* **2005**, *6*, 2277.

(42) Neuweiler, H.; Sauer, M. *Curr. Pharma. Biotech.* **2004**, *5*, 285.

(43) Sauer, M.; Neuweiler, H. *Methods Mol. Biol.* **2014**, *1076*, 597.

(44) Kumbhakar, M.; Kiel, A.; Pal, H.; Herten, D.-P. *ChemPhysChem* **2009**, *10*, 629

(45) Schuler, B.; Soranno, A.; Hofmann, H.; Nettels, D. *Annu. Rev. Biophys.* **2016**, *45*, 207.

(46) Tinnefeld, P.; Weston, K. D.; Vosch, T.; Cotlet, M.; Weil, T.; Hofkens, J.; Müllen, K.; Schryver, F. C. D.; Sauer, M. *J. Am. Chem. Soc.* **2002**, *124*, 14310.

(47) Sýkora, J.; Kaiser, K.; Gregor, I.; Bönigk, W.; Schmalzing, G.; Enderlein, J. *Anal. Chem.* **2007**, *79*, 4040.

(48) Ta, H.; Kiel, A.; Wahl, M.; Herten, D.-P. *Phys. Chem. Chem. Phys.* **2010**, *12*, 10295.

(49) Mets, Ü.; Widengren, J.; Rigler, R. *Chem. Phys.* **1997**, *218*, 191.

(50) Vester, M.; Staut, T.; Enderlein, J.; Jung, G. *J. Phys. Chem. Lett.* **2015**, *6*, 1149.

(51) Vester, M.; Grueter, A.; Finkler, B.; Becker, R.; Gregor, I. *Phys. Chem. Chem. Phys.* **2016**, *18*, 10281.

(52) Schwartz, O.; Levitt, J. M.; Tenne, R.; Itzhakov, S.; Deutsch, Z.; Oron, D. *Nano Lett.* **2013**, *13* 5832.

(53) Lim, S. Y.; Shen, W.; Gao, Z. *Chem. Soc. Rev.* **2015**, *44* 362.

(54) Hong, G.; Diao, S.; Antaris, A. L.; Dai, H. *Chem. Rev.* **2015**, *115*, 10816.

(55) Wang, Y.; Hu, A. *J. Mater. Chem. C* **2014**, *2*, 6921.

(56) Baker, S. N.; Baker, G. A. *Angew. Chem. Int. Ed.* **2010**, *49*, 6726

(57) Fu, M.; Ehrat, F.; Wang, Y.; Milowska, K. Z.; Reckmeier, C.; Rogach, A. L.; Stolarczyk, J. K.; Urban, A. S.; Feldmann, J. *Nano Lett.* **2015**, *15*, 6030.

(58) Dekaliuk, M. O.; Viagin, O.; Malyukin, Y. V.; Demchenko, A. P. *Phys. Chem. Chem. Phys.* **2014**, *16*, 16075.

(59) Nie, H.; Li, M.; Li, Q.; Liang, S.; Tan, Y.; Sheng, L.; Shi, W.; Zhang, S. X.-A. *Chem. Mater.* **2014**, *26*, 3104.

(60) Das, S. K.; Liu, Y.; Yeom, S.; Kim, D. Y.; Richards, C. I. *Nano Lett.* **2014**, *14*, 620−625.

(61) Sun, Y.-P.; Zhou, B.; Lin, Y.; Wang, W.; Fernando, K. A. S.; Pathak, P.; Meziani, M. J.; Harruff, B. A.; Wang, X.; Wang, H.; Luo, P. G.; Yang, H.; Kose, M. E.; Chen, B.; Veca, L. M.; Xie, S.-Y. *J. Am. Chem. Soc.* **2006**, *128*, 7756.

(62) Khan, S.; Gupta, A.; Verma, N. C.; Nandi, C. K. *Nano Lett.* **2015**, *15*, 8300.

(63) Ringemann, C.; Schçnle, A.; Giske, A.; Middendorff, C. v.; Hell, S. W.; Eggeling, C. *ChemPhysChem* **2008**, *9*, 612

(64) Neuweiler, H.; Schulz, A.; Böhmer, M.; Enderlein, J.; Sauer, M. *J. Am. Chem. Soc.* **2003**, *125*, 5324.

(65) Qu, P.; Yang, X.; Li, X.; Zhou, X.; Zhao, X. S. *J. Phys. Chem. B* **2010**, *114*, 8235.

(66) Sun, Q.; Lu, R.; Yu, A. *J. Phys. Chem. B* **2012**, *116*, 660.

(67) Zhu, R.; Li, X.; Zhao, X. S.; Yu, A. *J. Phys. Chem. B* **2011**, *115*, 5001.

(68) Stefan, M. I.; Novère, N. L. *PLOS Computational Biology* **2013**, *9*, e1003106.

(69) Huang, C. Y. *Methods in Enzymology* **1982**, *87*, 509.

(70) Nigam, S.; Durocher, G. *J. Phys. Chem.* **1996**, *100*, 7135.

(71) Bollmann, S.; Lollmann, M.; Sauer, M.; Doose, S. *Phys. Chem. Chem. Phys.* **2011**, *13*, 12874.

(72) Boaz, H.; Rollefson, G. K. *J. Am. Chem. Soc.* **1950**, *72*, 3435.

(73) Rath, M. C.; Pal, H.; Mukherjee, T. *J. Phys. Chem. A* **2001**, *105*, 7945.

(74) Keizer, J. *J. Am. Chem. Soc.* **1983**, *105*, 1494.

(75) Buschmann, V.; Weston, K. D.; Sauer, M. *Bioconjugate Chem.* **2003**, *14*, 195.

(76) Haustein, E.; Schwille, P. *Annu. Rev. Biophys. Biomol. Struct.* **2007**, *36*, 151.

(77) Sauer, M.; Hofkens, J.; Enderlein, J. *Handbook of Fluorescence Spectroscopy and Imaging: From Ensemble to Single Molecules*; Wiley-VCH Verlag GmbH & Co. KGaA, 2011.

(78) Bordello, J.; Snchez, M. I.; Vázquez, M. E.; MascareÇas, J. L.; Al-Soufi, W.; Novo, M. *Angew. Chem. Int. Ed.* **2012**, *51*, 7541.

(79) Verma, S. D.; Pal, N.; Singh, M. K.; Shweta, H.; Khan, M. F.; Sen, S. *Anal. Chem.* **2012**, *84*, 7218.

(80) Das, N. K.; Ghosh, S.; Jaiswal, S.; Tewary, A.; Mukherjee, S. *Chem. Phys. Lett.* **2017**, *682*, 147.

(81) Dong, C.; Qian, H.; Fang, N.; Ren, J. *J. Phys. Chem. B* **2006**, *110*, 11069.

(82) Brox, D.; Kiel, A.; Wörner, S. J.; Pernpointner, M.; Comba, P.; Martin, B.; Herten, D.-P. *PLOS One* **2013**, *8*, e58049(7).

(83) Bera, K.; Das, A. K.; Nag, M.; Basak, S. *Anal. Chem.* **2014**, *86*, 2740.

(84) Magzoub, M.; Padmawar, P.; Dix, J. A.; Verkman, A. S. *J. Phys. Chem. B* **2006**, *110*, 21216.

(85) Tóth, É.; Brücher, E.; Lázár, I.; Tóth, I. *Inorg. Chem.* **1994**, *33*, 4070.

(86) Tircso´, G.; Kovacs, Z. n.; Sherry, A. D. *Inorg. Chem.* **2006**, *45*, 9269.

(87) Pham, T. A.; Xu, J.; Raymond, K. N. *J. Am. Chem. Soc.* **2014**, *136*, 9106.

(88) Göhler, A.; Andre´, S.; Kaltner, H.; Sauer, M.; Gabius, H.-J.; Doose, S. *Biophys. J.* **2010**, *98*, 3044.

(89) Göhler, A.; Büchner, C.; André, S.; Doose, S.; Kaltner, H.; Gabius, H.-J. *Biochimie* **2012**, *94* 2649e2655.

(90) Ma, Y.; Abbateb, V.; Hider, R. C. *Metallomics* **2015**, *7*, 212.

(91) Schwille, P.; Kummer, S.; Heikal, A. A.; Moerner, W. E.; Webb, W. W. *Proc. Natl. Am. Soc.* **2000**, *97*, 151.

(92) Escarrilla, A. M. *Talanta* **1966**, *13*, 363.

(93) Thomas, F.; Serratrice, G.; Be´guin, C.; Aman, E. S.; Pierre, J. L.; Fontecave, M.; Laulhe`re, J. P. *J. Biol. Chem.* **1999**, *274*, 13375.

(94) Nivens, D. A.; Zhang, Y.; Angel, S. M. *J. Photochem. Photobiol. A: Chem.* **2002**, *152*, 167.

(95) Wunderlich, B.; Nettels, D.; Benke, S.; Clark, J.; Weidner, S.; Hofmann, H.; Pfeil, S. H.; Schuler, B. *Nat. Protocols* **2013**, *8*, 1459.

(96) Zhang, X.; Sisamakis, E.; Sozanski, K.; Holyst, R. *J. Phys. Chem. Lett. , 8, 5785−5791* **2017**, *8*, 5785.

(97) Persson, I. *Pure Appl. Chem.* **2010**, *82*, 1901.

(98) Choppin, G. R. *J. Alloys & Comp.* **1995**, *225* 242.

(99) Ihnat, P. M.; Vennerstrom, J. L.; Robinson, D. H. *J. Pharmacol. Sci.* **2002**, *91*, 1733.

(100) Audras, M.; Berthon, L.; Martin, N.; Zorz, N.; Moisy, P. *J. Radioanal. Nucl. Chem.* **2015**, *303*, 1897.

(101) Wang, Y.; Kalytchuk, S.; Zhang, Y.; Shi, H.; Kershaw, S. V.; Rogach, A. L. *J. Phys. Chem. Lett.* **2014**, *5*, 1412.

(102) Shen, P.; Xia, Y. *Anal. Chem.* **2014**, *86*, 5323.

(103) Chizhik, A. M.; Stein, S.; Dekaliuk, M. O.; Battle, C.; Li, W.; Huss, A.; Platen, M.; Schaap, I. A. T.; Gregor, I.; Demchenko, A. P.; Schmidt, C. F.; Enderlein, J. r.; Chizhik, A. I. *Nano Lett.* **2016**, *16*, 237−242.

(104) Ding, H.; Yu, S.-B.; Wei, J.-S.; Xiong, H.-M. *ACS Nano* **2016**, *10*, 484.

(105) Jiang, K.; Zhang, L.; Lu, J.; Xu, C.; Cai, C.; Lin, H. *Angew. Chem. Int. Ed.* **2016**, *55*, 7231.

(106) Lu, S.; Cong, R.; Zhu, S.; Zhao, X.; Liu, J.; S.Tse, J.; Meng, S.; Yang, B. *ACS Appl. Mater. Interfaces* **2016**, *8*, 4062.

(107) Bhattacharya, A.; Chatterjee, S.; Prajapati, R.; Mukherjee, T. K. *Phys. Chem. Chem. Phys.* **2015**, *17*, 12833.

(108) Ghosh, S.; Chizhik, A. M.; Karedla, N.; Dekaliuk, M. O.; Gregor, I.; Schuhmann, H.; Seibt, M.; Bodensiek, K.; Schaap, I. A. T.; Schulz, O.; Demchenko, A. P.; Enderlein, J.; Chizhik, A. I. *Nano Lett.* **2014**, *14*, 5656.

(109) Krysmann, M. J.; Kelarakis, A.; Dallas, P.; Giannelis, E. P. *J. Am. Chem. Soc.* **2012**, *134*, 747.

(110) Li, X.; Zhang, S.; Kulinich, S. A.; Liu, Y.; Zeng, H. *Sci. Rep.* **2014**, *4*, 4976.

(111) Cushing, S. K.; Li, M.; Huang, F.; Wu, N. *ACS Nano* **2014**, *8*, 1002.

(112) Kumbhakar, M.; Goel, T.; Nath, S.; Mukherjee, T.; Pal, H. *J. Phys. Chem. B* **2006**, *110*.

(113) Ruan, S.; Qian, J.; Shen, S.; Zhu, J.; Jiang, X.; Hea, Q.; Gao, H. *Nanoscale* **2014**, *6*, 10040.

(114) Demchenko, A. P. *Methods Enzymol.* **2008**, *450*, 59.

(115) Demchenko, A. P. *Weber's Red-Edge Effect that Changed the Paradigm in Photophysics and Photochemistry*; Springer International Publishing, Switzerland, 2016.

(116) Zhu, S.; Song, Y.; Zhao, X.; Shao, J.; Zhang, J.; Yang, B. *Nano Res.* **2015**, *8*, 355.

(117) Li, H.; He, X.; Kang, Z.; Huang, H.; Liu, Y.; Liu, J.; Lian, S.; Tsang, C. H. A.; Yang, X.; Lee, S.-T. *Angew. Chem. Int. Ed.* **2010**, *49*, 4430.

(118) Thiyagarajan, S. K.; Raghupathy, S.; Palanivel, D.; Raji, K.; Ramamurthy, P. *Phys. Chem. Chem. Phys.* **2016**, *18*, 12065.

(119) Liu, H.; Ye, T.; Mao, C. *Angew. Chem. Int. Ed.* **2007**, *46*, 6473.

(120) Zheng, H.; Wang, Q.; Long, Y.; Zhang, H.; Huang, X.; Zhu, R. *Chem. Commun.* **2011**, *47*, 10650.

(121) Yu, P.; Wen, X.; Toh, Y.-R.; Tang, J. *J. Phys. Chem. C* **2012**, *116*, 25552.

(122) Wen, X.; Yu, P.; Toh, Y.-R.; Hao, X.; Tang, J. *Adv. Opt. Mater.* **2013**, *1*, 173.

(123) Wang, L.; Zhu, S.-J.; Hai-YuWang; Qu, S.-N.; Zhang, Y.-L.; Zhang, J.-H.; Chen, Q.-D.; Xu, H.-L.; Han, W.; Yang, B.; Sun, H.-B. *ACS Nano* **2014**, *8*, 2541.

(124) Zhu, S.; Meng, Q.; Wang, L.; Zhang, J.; Song, Y.; Jin, H.; Zhang, K.; Sun, H.; Wang, H.; Yang, B. *Angew. Chem. Int. Ed.* **2013**, *59*, 3953.

(125) Song, Y.; Zhu, S.; Xiang, S.; Zhao, X.; Zhang, J.; Zhang, H.; Fu, Y.; Yang, B. *Nanoscale* **2014**, *6*, 4676.

(126) Song, Y.; Zhu, S.; Zhang, S.; Fu, Y.; Wang, L.; Zhao, X.; Yang, B. *J. Mater. Chem. C* **2015**, *3*, 5976.

(127) Dhenadhayalan, N.; Lin, K.-C.; Suresh, R.; Ramamurthy, P. *J. Phys. Chem. C* **2016**, *120*, 1252.

(128) Gude, V.; Das, A.; Chatterjee, T.; Mandal, P. K. *Phys. Chem. Chem. Phys.* **2016**, *18*, 28274.

(129) Schneider, J.; Reckmeier, C. J.; Xiong, Y.; Seckendorff, M. v.; Susha, A. S.; Kasak, P.; Rogach, A. L. *J. Phys. Chem. C* **2017**, *121*, 2014.

(130) Sun, Y.; Cao, W.; Li, S.; Jin, S.; Hu, K.; Hu, L.; Huang, Y.; Gao, X.; Wu, Y.; Liang, X.-J. *Sci. Rep.* **2013**, *3*, 3036.

(131) Zhu, S.; Wang, L.; Zhou, N.; Zhao, X.; Song, Y.; Maharjan, S.; Zhang, J.; Lu, L.; Wang, H.; Yang, B. *Chem. Commun.* **2014**, *50*, 13845.

(132) Kasprzyk, W.; Bednarz, S.; Bogdal, D. *Chem. Commun.* **2013**, *49*, 6445.

(133) Kasprzyk, W.; Bednarz, S.; Żmudzki, P.; Galica, M.; Bogdał, D. *RSC Adv.* **2015**, *5*, 34795.

(134) Demchenko, A. P.; Dekaliuk, M. O. *Nanoscale* **2016**, *8*, 14057.

(135) Chen, Y.; Zheng, M.; Xiao, Y.; Dong, H.; Zhang, H.; Zhuang, J.; Hu, H.; Lei, B.; Liu, Y. *Adv. Mater.* **2016**, *28*, 312.

(136) Jeong, C. J.; Lee, G.; Ina, I.; Park, S. Y. *Luminescence* **2015**, *31*, 897.

(137) Liu, Z. X.; Wu, Z. L.; Gao, M. X.; Huang, H. L. C. Z. *Chem. Commun.* **2016**, *52*, 2063.

(138) Sudolská, M. r.; Dubecký, M. s.; Sarkar, S.; Reckmeier, C. J.; Zbořil, R.; Rogach, A. L.; Otyepka, M. *J. Phys. Chem. C* **2015**, *119*, 13369.

(139) Reckmeier, C. J.; Wang, Y.; Zboril, R.; Rogach, A. L. *J. Phys. Chem. C* **2016**, *120*, 10591.

(140) Kasha, M. *Rad. Res.* **1963**, *20*, 55.

(141) Kasha, M.; Rawls, H. R.; El-Bayoumi, M. A. *Pure Appl. Chem.* **1965**, *11*, 371.

(142) Eisfeld, A.; Briggs, J. S. *Chem. Phys.* **2006**, *324*, 376.

(143) Berlepsch, H. v.; Ludwig, K.; Böttcher, C. *Phys. Chem. Chem. Phys.* **2014**, *16*, 10659.

(144) Deng, Y.; Yuan, W.; Jia, Z.; Liu, G. *J. Phys. Chem. B* **2014**, *118*, 14536.

(145) Berlepsch, H. v.; Brandenburg, E.; Koksch, B.; Bottcher, C. *Langmuir* **2010**, *26*, 11452.

(146) Spano, F. C. *Acc. Chem. Res.* **2010**, *43*, 429.

(147) Spano, F. C.; Silva, C. *Annu. Rev. Phys. Chem.* **2014**, *65*, 477.

(148) Gan, Z.; Hao, Y.; Shan, Y. *Chem. Nano. Mat.* **2016**, *2*, 171.

(149) Berlepsch, H. v.; Böttcher, C. *J. Phys. Chem. B* **2015**, *119*, 11900.

(150) Cho, Y.; Kang, B.; Lee, J.; Kim, S.; Kim, G. T.; Kang, H.; Lee, B. R.; Kim, H.; Shim, S.-H.; Lee, G.; Kwon, O.-H.; Kim, B.-S. *Chem. Mater.* **2016**, *28*, 6840.

(151) Wu, Q.; Li, W.; Wu, P.; Li, J.; Liu, S.; Jin, C.; Zhanc, X. *RSC Adv.* **2015**, *5*, 75711.

(152) Zhang, J.; Yang, L.; Yuan, Y.; Jiang, J.; Yu, S.-H. *Chem. Mater.* **2016**, *28*, 4367.

(153) Zhang, Y.; Wang, Y.; Feng, X.; Zhang, F.; Yang, Y.; Liu, X. *Appl. Surf. Sci.* **2016**, *387* 1236.

(154) Xiong, Y.; Schneider, J.; Reckmeier, C. J.; Huang, H.; Kasák, P.; Rogach, A. L. *Nanoscale* **2017**, *9*, 11730.

(155) Righetto, M.; Privitera, A.; Fortunati, I.; Mosconi, D.; Zerbetto, M.; Curri, M. L.; Corricelli, M.; Moretto, A.; Agnoli, S.; Franco, L.; Bozio, R.; Ferrante, C. *J. Phys. Chem. Lett.* **2017**, *8*, 2236.

(156) Shi, L.; Yang, J. H.; Zeng, H. B.; Chen, Y. M.; Yang, S. C.; Wu, C.; Zeng, H.; Yoshihito, O.; Zhang, Q. *Nanoscale* **2016**, *8*, 14374.

(157) Khan, S.; Sharma, A.; Ghoshal, S.; Jain, S.; Hazra, M. K.; Nandi, C. K. *Chem. Sci.* **2017**, *doi:10.1039/c7sc02528a*.

(158) Li, Q.; Chen, B.; Xing, B. *Environ. Sci. Technol.* **2017**, *51*, 1364.

(159) Liati, A.; Brem, B. T.; Durdina, L.; Vögtli, M.; Dasilva, Y. A. R.; Eggenschwiler, P. D.; Wang, J. *Environ. Sci. Technol.* **2014**, *48*, 10975.

(160) Pawlyta, M.; Rouzaud, J.-N. l.; Duber, S. *Carbon* **2015**, *84*, 479.

(161) Rouzaud, J.-N.; Deldicque, D.; Charon, E.; Pageot, J. *C. R. Geoscience* **2015**, *347* 124.

(162) Pawlyta, M.; Hercman, H. *Annales Societatis Geologorum Poloniae* **2016**, *86*, 237.

(163) Heidenreich, R. D.; Hess, W. M.; Ban, L. L. *J. Appl. Crystallogr.* **1968**, *1*, 1.

(164) Sciortino, A.; Marino, E.; Dam, B. v.; Schall, P.; Cannas, M.; Messina, F. *J. Phys. Chem. Lett.* **2016**, *7*, 3419.

(165) Sciortino, A.; Cayuela, A.; Soriano, M. L.; Gelardi, F. M.; Cannas, M.; Valca´rcelc, M.; Messina, F. *Phys. Chem. Chem. Phys.* **2017**, *19*, 22670.

(166) Leménager, G.; Luca, E. D.; Sun, Y.-P.; Pompa, P. P. *Nanoscale* **2014**, *6*, 8617.

(167) Verma, N. C.; Khan, S.; Nandi, C. K. *Methods Appl. Fluoresc.* **2016**, *4*, 044006.

(168) Hafi, N.; Grunwald, M.; Heuvel, L. S. v. d.; Aspelmeier, T.; Chen, J.-H.; Zagrebelsky, M.; Schütte, O. M.; Steinem, C.; Korte, M.; Munk, A.; Walla, P. J. *Nat. Method* **2014**, *5*, 579.

(169) Dong, Y.; Pang, H.; Yang, H. B.; Guo, C.; Shao, J.; Chi, Y.; Li, C. M.; Yu, T. *Angew. Chem. Int. Ed.* **2013**, *52*, 7800.

(170) Hou, J.; Wang, L.; Zhang, P.; Xu, Y.; Ding, L. *Chem. Commun.* **2015**, *51*, 17768.

(171) Zhang, Y.; He, J. *Phys.Chem.Chem.Phys.* **2015**, *17*, 20154.

(172) Liu, Y.; Zhou, L.; Li, Y.; Deng, R.; Zhang, H. *RSC Adv.* **2016**, *6*, 108203.

(173) Wen, Z.-H.; Yin, X.-B. *RSC Adv.* **2016**, *6*, 27829.

(174) Yuan, Y. H.; Liu, Z. X.; Li, R. S.; Zou, H. Y.; Lin, M.; Liu, H.; Huang, C. Z. *Nanoscale* **2016**, *8*, 6770.

(175) Chen, H.; Wang, L.; Fu, H.; Wang, Z.; Xie, Y.; Zhang, Z.; Tang, Y. *J. Mater. Chem. B* **2016**, *4*, 7472.

(176) Cheng, J.; Wang, C.-F.; Zhang, Y.; Yang, S.; Chen, S. *RSC Adv.* **2016**, *6*, 37189.